UNIVERSITÉ DE MONTRÉAL

MEASUREMENT OF PULMONARY FUNCTION WITH

ELECTRICAL IMPEDANCE TOMOGRAPHY

ANDREW ADLER

INSTITUT DE GÉNIE BIOMÉDICAL

ÉCOLE POLYTECHNIQUE DE MONTRÉAL

THÈSE PRÉSENTÉE EN VUE DE L'OBTENTION

DU DIPLÔME DE PHILOSOPHIAE DOCTOR (Ph.D.)

(GÉNIE BIOMÉDICAL)

OCTOBRE 1995

UNIVERSITÉ DE MONTRÉAL

ÉCOLE POLYTECHNIQUE DE MONTRÉAL

Cette thèse intitulée

MEASUREMENT OF PULMONARY FUNCTION WITH

ELECTRICAL IMPEDANCE TOMOGRAPHY

présentée par: ADLER Andrew

en vue de l'obtention du diplôme de: Philosophiae Doctor

a été dûment acceptée par le jury d'examen constitué de:

M. GOUSSARD Yves, Ph.D., président

M. GUARDO Robert, Ph.D., membre et directeur de recherche

M. BERTHIAUME Yves, M.D., M.Sc., membre et codirecteur de recherche

M. SAVARD Pierre, Ph.D., membre

M. NEWELL Jonathan., Ph.D., membre

To Alison

Of making many books there is no end,

and much study wearies the body.

˜ *Ecclesiastes*

REMERCIEMENTS

Premièrement, j'aimerais remercier mon directeur de recherche, le Dr Robert Guardo, pour son encouragement continu et précieux, ses avis judicieux et pertinents, ses critiques constructives, son encadrement, sa disponibilité, et son généreux appui financier.

J'aimerais également remercier mon codirecteur, le Dr Yves Berthiaume, pour sa patience à m'expliquer des notions de physiologie respiratoire, ses conseils judicieux, son encouragement − surtout quand les expériences ne se déroulaient pas comme prévu − et pour son aide généreuse.

Je remercie le Dr Yves Goussard pour son enseignement et pour la clarté de ses explications sur les techniques de régularisation. J'aimerais souligner la contribution de M. Christian Boulay à la réussite de la partie expérimentale de ce projet, rendue possible en partie par le système d'acquisition de données HEMOS III qu'il avait développé. Je tiens aussi à remercier M. Claude Turcotte qui nous a assuré le bon fonctionnement du réseau informatique du laboratoire.

Un grand merci à tout mes confrères de l'Institut de génie biomédical, qui ont su rendre agréable cette période de ma vie. Merci à M. Ghislain Savoie pour son aide technique, à M. Faouzi Kallel pour ces opinions judicieuses sur mes idées, à M. Stéphane Trudelle pour l'enthousiasme avec lequel il a mis à l'épreuve par des essais *in vitro* les résultats de mes simulations. Merci à MM. Lahbib Soualmi, Roch Maurice et Martin Cyr aussi qu'à tous mes autres amis du laboratoire pour leur amitié et soutien.

Je salue également l'équipe avec laquelle j'ai réalisé les expériences cliniques à l'Hôtel-Dieu de Montréal, qui était composée du Dr Robert Amyot et Mme Chantale Massé. Ils m'ont offert une grande amitié et un bon encouragement.

And finally, I would like to thank Dr. Jason Bates and Mr. Thomas Schuessler of the Meakins-Christie Laboratories whose advice and support were greatly appreciated.

RÉSUMÉ

La tomographie d'impédance électrique (TIE) se sert des mesures d'impédance électrique, effectuées à l'aide d'électrodes placées sur la surface du corps, pour construire une image du changement de conductivité dans une section du corps. Un courant de basse fréquence est appliqué entre des paires d'électrodes pendant que le potentiel produit par ce courant est mesuré par d'autres paires d'électrodes. La technique habituelle consiste à acquérir une séquence d'ensembles de mesures et à reconstruire des images qui représentent le changement de la distribution survenus entre l'instant où un ensemble de référence est acquis et chacun des autres ensembles. Cette technique présente un intérêt pour l'étude de la fonction pulmonaire, parce que les phénomènes physiologiques sous-jacents, soit le mouvement de l'air, la perfusion sanguine et la présence pathologique d'air ou de fluide, produisent des changements importants dans la distribution de conductivité du thorax.

La reconstruction d'images en TIE nécessite la solution d'un problème inverse non linéaire et mal posé, à partir de données bruitées. La solution de ce type de problème exige des hypothèses simplificatrices ou une régularisation. Deux algorithmes sont proposés dans cette thèse qui tiennent compte de la géométrie du milieu conducteur et du niveau du bruit des données, et permettent la reconstruction rapide d'images. Le premier algorithme, basé sur des réseaux de neurones artificiels, calcule une approximation linéaire du problème inverse directement à partir de simulations du problème direct par la méthode d'éléments finis. Cet algorithme donne des résultats acceptables quand le niveau de bruit dans les mesures est semblable à celui utilisé pour l'entraînement du réseau. Le deuxième algorithme utilise une approche de *maximum a posteriori* basée sur des estimations du bruit de mesure et de la résolution maximale disponible. Cette technique permet une interprétation intuitive des paramètres de l'algorithme et repose sur une base théorique. Pour comparer ces algorithmes aux autres techniques proposées dans la littérature, certains indices de performance sont développés pour mesurer la résolution de l'image, l'amplification du bruit et la fidélité de positionnement d'une cible dans l'image.

L'interprétation des images de TIE est compliquée, car elle se heurte à plusieurs difficultés expérimentales. Par exemple, dans le cas de l'étude de la fonction pulmonaire, le mouvement des électrodes placées sur la surface du thorax produit une erreur de

mesure. Un modèle par éléments finis des propriétés mécaniques et électriques du thorax a été utilisé pour déterminer l'effet de l'expansion de la cage thoracique sur la distribution de conductivité reconstruite. Les résultats de ces simulations montrent que l'expansion du thorax contribue jusqu'à 20 pour cent de l'amplitude de l'image. Toutefois, pour des applications qui visent uniquement à évaluer un changement dans le niveau d'activité physiologique, l'effet de cette expansion peut être négligé parce qu'il varie linéairement avec le volume courant pulmonaire.

Une série d'expériences sur le chien ont été effectuées pour déterminer la précision avec laquelle la TIE permet de mesurer la ventilation pulmonaire et la quantité de fluide présent dans un poumon. Les résultats de ces expériences démontrent une bonne corrélation linéaire (r > .95) entre l'amplitude de l'image et le volume courant ou la quantité du fluide. L'erreur moyenne de mesure était de 90 ml pour la ventilation et de 10 ml pour l'instillation du fluide. De plus, les images montrent clairement la région des poumons de l'animal et le poumon ayant subi l'instillation du fluide. Les résultats rapportés dans cette thèse démontrent le potentiel de la TIE comme outil d'investigation de la fonction pulmonaire.

ABSTRACT

Electrical Impedance Tomography (EIT) uses electrical measurements at electrodes placed on the body surface to produce a cross-sectional image of conductivity changes within the body. A low frequency current is injected between pairs of electrodes while voltage measurements are made at all other electrode pairs. Images are reconstructed of the change in conductivity distribution between the acquisition of the two sets of measurements. This technique can potentially provide useful information for the investigation of pulmonary function as the clinical phenomena of interest (air movement, blood perfusion, and pathological air or fluid presence, for example) induce large conductivity changes.

Reconstruction of images in EIT requires the solution of an ill-conditioned non-linear inverse problem on noisy data, typically requiring simplifying assumptions or regularization. Two reconstruction algorithms are proposed which take into account the geometry of the conductive medium and the noise level in the measured data, and allow fast (near real-time) image reconstruction. An algorithm based on artificial neural networks is used to calculate a linear approximation of the inverse problem directly from finite element simulations of the forward problem. Results show good reconstruction when the signal to noise ratio (SNR) in the measurements is similar to the SNR used during network calculation. Additionally, a *maximum a posteriori* (MAP) approach to image reconstruction is developed, based on a priori estimates of the measurement noise and the maximum image resolution available. This approach has the advantage of an intuitive interpretation of algorithm parameters as well as theoretical support. In order to compare these approaches to existing algorithms, figures of merit are developed to measure the reconstructed image resolution, the noise amplification of the image reconstruction, and the fidelity of positioning of a target in the image.

Certain physiological realities complicate the interpretation of EIT images. In the case of imaging of pulmonary function, the movement of electrodes placed on the thorax due to rib cage expansion introduces artefacts into the images. A finite element model of the mechanical and electrical properties of the thorax is used to determine the effect of chest expansion on the reconstructed conductivity change images. Results indicate that thorax expansion accounts for up to 20 percent of the reconstructed image amplitude,

although for applications which are only concerned with changes in the level of physiological activity, the effect of the expansion can be neglected as it varies linearly with the lung tidal volume.

Finally, in order to experimentally validate EIT as a tool for the measurement of pulmonary function, a series of experiments on dogs were conducted to quantify the accuracy of measurement of lung ventilation and lung fluid instillation. Results indicate good linear correlation (r > .95) between image amplitude and the tidal volume or fluid quantity. The average EIT measurement error was 90 ml for ventilation and 10 ml for instillation. Additionally, images clearly show the lung region of the animal and indicate which lung underwent fluid instillation. These results demonstrate the potential of EIT as a tool for the investigation of pulmonary function.

CONDENSÉ EN FRANÇAIS

0.1 Introduction

Selon les lois de la physique, on peut déterminer la structure d'un corps en injectant de l'énergie dans un corps et en étudiant comment il interagit avec cette énergie. La tomographie d'impédance électrique (TIE) suit cette approche analytique en injectant de l'énergie sous la forme d'un courant électrique et en mesurant comment la distribution de conductivité et la géométrie du corps modifient le champ de potentiel produit par ce courant. En pratique, l'injection de courant et la mesure de potentiel s'effectuent uniquement par des électrodes placées à la surface du corps. Toutefois, il est possible d'utiliser des connaissances mathématiques des règles d'interaction pour estimer la distribution de conductivité à l'intérieur du corps à partir d'un ensemble limité de mesures.

D'un point de vue clinique, la distribution de conductivité électrique dans le corps humain présente peu d'intérêt, même si cette propriété intrinsèque des tissus et des fluides du corps pourrait servir à les distinguer. Par contre, certains phénomènes physiologiques, comme la respiration, l'activité cardiaque et la digestion, impliquent le mouvement de fluides qui modifie la distribution de conductivité du corps. En mesurant l'effet de ces mouvements sur la distribution de conductivité il devient possible d'étudier ces phénomènes.

Bien que la TIE n'offre pas une résolution spatiale comparable à celle de la radiographie ou de la résonance magnétique nucléaire, elle présente certains avantages pour les études cliniques. Elle est non invasive, relativement compacte en termes d'équipement et peu encombrante pour le patient. En raison de sa faible résolution spatiale, la TIE ne convient pas à l'imagerie *anatomique*, mais elle peut être fort utile pour certaines études *fonctionnelles*.

Une application très prometteuse de la TIE est la surveillance de la fonction pulmonaire. Les phénomènes physiologiques d'intérêt, tels que la ventilation et la perfusion pulmonaire ainsi que la présence pathologique de fluides, provoquent des changements relativement importants de la distribution de conductivité du thorax.

Contrairement aux mesures mécaniques du débit et de la pression d'air au niveau de la bouche, qui ne donnent qu'un indice global de la fonction pulmonaire, la TIE produit une image du thorax qui permet de détecter et de localiser des anomalies. La TIE a également comme avantage par rapport à d'autres modalités d'imagerie de permettre une surveillance continue du patient au cours de la thérapie.

Le principal objectif de cette thèse était de vérifier la faisabilité de mesurer certains paramètres de la fonction pulmonaire à partir de la TIE. La thèse effectue cette vérification en se basant sur trois volets: le développement de méthodes de reconstruction d'images, la modélisation sur ordinateur de l'extraction de paramètres physiologiques à partir de la TIE et l'évaluation expérimentale de ces techniques.

0.2   Reconstruction d'images

Bien que plusieurs groupes aient étudié le problème de la reconstruction d'images en TIE, certaines difficultés expérimentales n'ont pas encore été traitées de façon rigoureuse. La géométrie non circulaire du thorax, la variabilité de l'espacement entre les électrodes, le bruit inhérent aux instruments de mesure et la présence possible de canaux de mesure défectueux posent de sérieux problèmes. Les techniques décrites dans cette thèse essayent de tenir compte de ces difficultés tout en visant une reconstruction d'images rapide.

Deux protocoles d'imagerie ont été proposés pour la TIE. L'imagerie *statique* reconstruit la distribution de conductivité absolue à partir d'un seul ensemble de mesures, tandis que l'imagerie *dynamique* calcule le changement de cette distribution à partir des changements présents dans deux ensembles de mesures acquis en des instants différents. En général, les algorithmes pour la reconstruction d'images statiques sont très sensibles aux erreurs de mesure et à la variabilité dans la géométrie du milieu (Barber, 1988). Cette thèse se concentre sur l'imagerie dynamique, qui, tout en étant moins générale que l'imagerie statique, est considérablement plus robuste. Ainsi, les images qui seront reconstruites et traitées dans ce projet représentent le changement de la distribution de conductivité, $\mathbf{x}$, correspondant à deux ensembles de mesure, $\mathbf{v}^1$ et $\mathbf{v}^2$, acquis aux instants t^1 et t^2, respectivement. Avec la méthode des éléments finis, le milieu est divisé en N éléments triangulaires et le changement du logarithme de la conductivité est représenté

par l'élément correspondant du vecteur **x**. Le vecteur du signal dynamique, **z**, est défini par:

$$\mathbf{z}_i = \frac{\mathbf{v}_i^1 - \mathbf{v}_i^2}{\frac{1}{2}\left(\mathbf{v}_i^1 + \mathbf{v}_i^2\right)}$$

(0.1)

où chaque composant *i* est obtenu par une combinaison de quatre électrodes: deux pour l'injection de courant et deux pour la mesure d'une différence de potentiel. Pour une reconstruction d'images rapide, une approximation linéaire est développée. Une estimation $\hat{\mathbf{x}}$ des changements de conductivité est calculée à partir du signal, **z**, et d'une matrice de reconstruction, **B**, avec l'équation linéaire:

$$\hat{\mathbf{x}} = \mathbf{Bz}$$

(0.2)

Deux techniques sont proposées pour calculer cette matrice de reconstruction: une basée sur les réseaux de neurones artificiels et l'autre sur l'estimation maximum a posteriori.

0.2.1 Reconstruction d'images par réseaux de neurones artificiels

La méthode des réseaux de neurones artificiels (RNA) permet de développer un modèle d'un problème sans exiger une relation mathématique explicite. Dans son application à la reconstruction d'images de TIE le principal attrait de cette technique est que le RNA peut être adapté par un processus d'«entraînement» à donner sa meilleure performance pour la géométrie et le niveau de bruit rencontrés dans la phase de l'entraînement. Chaque élément du réseau calcule le changement de conductivité d'un élément de volume du corps, en calculant la somme de chaque élément du signal **z** pondéré par la valeur de la matrice **N** correspondante (la matrice **N** est équivalente à **B** dans l'approche RNA).

Le calcul des éléments de la matrice **N** est appelé l'«entraînement» du réseau. Cette phase exige un ensemble de patrons d'entraînement et la réponse désirée correspondante. Cet ensemble de patrons et de réponses peut être mesuré *in vitro* (Guardo, 1991) ou, pour des raisons d'efficacité et de simplicité, être calculés avec un modèle par éléments finis du corps. L'algorithme d'entraînement du RNA est le suivant:
- Tous les poids, **N**, sont initialisés à des petites valeurs aléatoires.
- Un ordre aléatoire de présentation de vecteurs d'entraînement au RNA est choisi.
- Début des itérations d'entraînement.

- Un vecteur d'entraînement, plus du bruit, est présenté au réseau pour calculer une estimation de l'image, **o**:

$$\mathbf{o} = \mathbf{N}_i(\mathbf{z} + \mathbf{n})$$

(0.3)

- L'erreur, **e = o − d**, est calculée, où **d** est la réponse désirée du RNA.
- Le réseau est actualisé par la règle (**N**$_i$ représente les poids à l'itération i):

$$\mathbf{N}_{i+1} = \mathbf{N}_i - \alpha \mathbf{e} \mathbf{o}^t$$

(0.4)

où le paramètre α contrôle le taux d'entraînement.

- Les itérations sont poursuivies jusqu'à ce que l'erreur moyenne, $\sqrt{\mathbf{e}^t \mathbf{e}}$, atteigne un seuil acceptable.

Les principaux avantages de la technique RNA sont sa simplicité numérique et sa capacité de résoudre des problèmes complexes en tenant compte des conditions présentes dans la phase d'entraînement. Dans ce modèle, la matrice de reconstruction d'images est déterminée uniquement à partir d'un modèle du problème direct par éléments finis et d'une estimation du niveau de bruit du système de mesure. Quand le RNA est entraîné sans bruit, la reconstruction d'images a une bonne résolution mais une faible capacité de rejeter le bruit de mesure. Par contre, le RNA entraîné avec un niveau de bruit plus élevé a une meilleure performance dans des conditions de bruit de mesure similaires à celles de l'entraînement.

Même si les RNA sont capables de produire de bonnes images, il reste deux désavantages importants. D'un part, le fait que la solution n'exige pas de formulation théorique impose certaines limites sur l'interprétation des images. D'autre part, étant donné que le réseau est spécifique aux conditions d'entraînement, tout changement des conditions expérimentales nécessite l'entraînement d'un nouveau réseau, ce qui est très coûteux en temps de calcul.

0.2.2   Reconstruction d'images par estimation *maximum a posteriori*

Le deuxième technique est basée sur une approche bayésienne, qui permet d'introduire des informations sur le système et sur l'image en termes probabilistes. Ceci donne lieu à une interprétation plus naturelle des connaissances *a priori* en termes de paramètres du modèle. Par exemple, un canal de mesure défectueux indique une haute probabilité d'erreur dans les données acquises par ce canal. En utilisant une telle approche et un estimateur *maximum a posteriori* (MAP), et sous les hypothèses que le problème direct est linéaire et que les densités de probabilité de l'objet de du bruit ont une forme gaussienne. On aboutit naturellement à un estimateur de la forme d'équation 0.2, dans lequel la matrice **B** a pour expression:

$$\mathbf{B} = \left(\mathbf{H}^t \mathbf{W} \mathbf{H} + \mu \mathbf{Q} \right)^{-1} \mathbf{H}^t \mathbf{W}$$

(0.5)

où **B** dépend des paramètres **H**, **W**, **Q**, et μ, qui tiennent compte des propriétés du milieu et du système de mesure. Le problème direct est linéarisé en calculant une matrice de sensibilité **H** définie par:

$$\mathbf{H}_{ij} = \frac{\partial [\mathbf{Z}(\mathbf{x})]_i}{\partial \mathbf{x}_j} \bigg|_{\mathbf{x} = \mathbf{x}_o}$$

(0.6)

où **Z**(**x**) est un modèle par éléments finis du signal dynamique mesuré, **z**, produit par un changement de conductivité **x** autour d'une conductivité du milieu environnant **x**$_O$. Une colonne *j* de **H** représente le signal produit par un petit changement de conductivité dans l'élément *j*. Les dimensions de **H** sont le nombre de mesures par le nombre d'éléments de conductivité. Puisque, en général, on n'a pas d'information anatomique pour préciser **x**$_O$, **H** est calculé autour d'une distribution homogène. **W** est une matrice diagonale de la réciproque de la variance du bruit dans chaque élément du signal; les valeurs peuvent être calculées à partir de la définition du signal, ou mesurées à partir du système tomographique.

Pour éviter d'introduire des artefacts par une discrétisation trop grossière du milieu, le nombre d'éléments de conductivité indépendants doit être aussi élevé que possible. Par exemple, si on désire une résolution spatiale équivalant à 10 pour cent du diamètre du milieu, il faut une centaine d'éléments indépendants. Cependant, si on utilise 16 électrodes, on ne possède pas assez d'information pour estimer autant de paramètres indépendants. Ce problème est dit mal posé, et a besoin d'information *a priori* pour

produire une solution unique. **Q** est une matrice de régularisation qui pénalise toute composante de l'image avec une fréquence spatiale au-dessus d'un seuil. Les simulations ont démontré qu'un bon choix de seuil pour 16 électrodes correspond à 10 pour cent du diamètre du milieu. Le paramètre µ contrôle la quantité de régularisation utilisée. Une petite valeur de µ produit la meilleure résolution mais a tendance à amplifier le bruit de mesure; par ailleurs, une grande valeur de µ réduit la résolution pour améliorer la performance en termes de bruit. La valeur de µ doit donc être choisie pour obtenir le meilleur compromis entre l'amplification du bruit et la résolution spatiale pour chaque situation expérimentale.

Cette technique offre plusieurs avantages pour la reconstruction d'images. Le modèle par éléments finis permet d'utiliser cet algorithme avec un corps de forme arbitraire, et la formulation MAP caractérise le problème en termes de paramètres du milieu et du système de mesure. La possibilité de calculer une matrice de reconstruction signifie que la caractérisation du système peut être faite en temps différé et que, ensuite, la reconstruction d'images sera très rapide.

0.2.3   Évaluation d'algorithmes de reconstruction d'images

Pour évaluer le succès d'un approche de reconstruction d'images et pour comparer les algorithmes développés dans cette thèse avec ceux proposés dans la littérature, il est important d'avoir des critères de comparaison. Quatre indices de performance de reconstruction d'images ont été définis. Le *noise figure* (NF) est une mesure de l'amplification du bruit par le processus de reconstruction d'images. Par comparaison avec un système de communication, on considère la matrice de reconstruction comme un récepteur à l'entrée duquel il y a un signal **z** et un bruit **n**. Le signal de sortie du récepteur est l'image **Bz** avec un bruit **Bn**. Le NF est le ratio du rapport signal sur bruit (RSB) à l'entrée et à la sortie du récepteur. Cette valeur de NF dépend seulement de la matrice de reconstruction, qui est une fonction de µ.

$$\mathrm{NF} = \frac{\mathrm{RSB}_{\mathrm{entrée}}}{\mathrm{RSB}_{\mathrm{sortie}}} = \left(\frac{\mathrm{moy}[\mathbf{z}]}{\sqrt{\mathrm{var}[\mathbf{n}]}} \right) \Big/ \left(\frac{\mathrm{moy}[\mathbf{Bz}]}{\sqrt{\mathrm{var}[\mathbf{Bn}]}} \right)$$

(0.7)

Un second indice, le *blur radius* (BR), mesure la résolution de la reconstruction. Le signal produit par une cible ponctuelle est mesuré, l'image de ce changement de conductivité est reconstruite, et le rayon moyen de la zone qui contient la moitié de l'amplitude de l'image est calculé. Étant donné que la TIE est plus sensible aux changements de conductivité à proximité de la surface du corps, la résolution dépend du rayon et le BR doit être calculé en fonction de la position radiale de la cible.

Le *position error* (PE) est une mesure de la fiabilité de reconstruction de la position d'une cible. Certains algorithmes, dont le «backprojection» (Barber, 1987), ont tendance à «pousser» la position d'un objet plus au centre de l'image qu'il ne l'était en réalité. Le PE est défini comme la position radiale réelle de la cible ponctuelle moins la position radiale du centre de la zone du BR.

Le dernier indice est une mesure de la sensibilité de la TIE et décrit la probabilité de non-détection d'un contraste. Le calcul de cette probabilité tient compte de la matrice de reconstruction, du niveau du bruit de mesure et de la région d'intérêt autour du contraste. Un contraste est plus facilement visible si une région d'intérêt est choisie parce que le bruit à l'extérieur de cette région est ignoré.

0.3   Modélisation physiologique

L'interprétation d'images en TIE est compliquée, car elle doit tenir compte de certaines réalités physiologiques. Idéalement, l'algorithme de reconstruction d'images devrait tenir compte de tous les détails de l'anatomie et de la configuration du système de mesure. Or, ceci n'a pas été possible. Par exemple, il n'existe présentement aucun algorithme d'imagerie qui tienne compte de l'anisotropie du corps ou du mouvement des électrodes dû à la respiration et aux changements de posture. Ceci indique que les images de changements de conductivité *in vivo* sont soumises à plusieurs sources d'erreurs. Faute de techniques pour éliminer ces erreurs, il est important d'estimer leur importance et de comprendre leurs effets sur les images.

On a analysé dans cette thèse le problème du mouvement des électrodes produit par la respiration, parce qu'il est apparu qu'il pourrait avoir un effet important sur la mesure de la fonction pulmonaire. Les algorithmes de reconstruction d'images en TIE

font l'hypothèse que les changements observés dans les mesures d'impédance dépendent uniquement des changements de conductivité. Or, les mesures effectuées à la surface du thorax dépendent aussi du mouvement de la cage thoracique. Un modèle par éléments finis bidimensionnel des propriétés mécaniques et électriques du thorax a été utilisé pour simuler le mouvement des électrodes et des structures anatomiques produit par l'expansion du thorax. Ensuite, les données mécaniques ont été utilisées avec une connaissance des propriétés électriques des tissus pour simuler l'ensemble de mesures d'impédance à la fin de l'inspiration et à la fin de l'expiration, en présence et en absence de mouvement des électrodes. Finalement, des images ont été reconstruites à partir de ces données et comparées. Les résultats indiquent que l'expansion du thorax introduit un artefact au centre de l'image, qui peut contribuer jusqu'à 20 pour cent de l'amplitude de l'image. Bien que cette contribution varie selon l'anatomie, elle est relativement indépendante du volume courant. Pour certaines applications où on s'intéresse uniquement au changement du niveau de l'activité physiologique, l'effet de cette expansion peut être négligé parce qu'il varie linéairement avec le changement de conductivité.

0.4   Évaluation expérimentale

Il est important dans un projet comme celui-ci, qui vise à déterminer l'utilité d'une nouvelle technique pour des études cliniques, qu'une évaluation expérimentale soit effectuée. Une série de dix expériences a été effectuée sur le chien pour quantifier la précision des mesures de ventilation pulmonaire, d'instillation de fluide dans un poumon et de la détermination du poumon ayant subi l'instillation. La ventilation a été mesurée sur l'image du changement de conductivité entre la fin de l'expiration et la fin de l'inspiration. Des mesures ont été prises aux volumes courants de 200 ml, 500 ml, 700 ml, et 1000 ml. Les résultats indiquent une bonne corrélation entre l'amplitude de l'image et le volume courant du ventilateur, l'erreur moyenne de mesure par TIE étant de 90 ml.

Ensuite, un cathéter a été placé dans un lobe du poumon droit avec un bronchoscope, et des acquisitions ont été faites à la fin de l'expiration après instillation successive de 10 ml, 25 ml, 50 ml, 75 ml et 100 ml de solution saline. Les images ont été reconstruites entre l'acquisition suivant l'instillation et une référence prise à la fin de l'expiration avant le début de l'instillation. L'amplitude de l'image présentait une bonne

corrélation avec le volume du fluide instillé, et l'erreur moyenne de mesure par TIE était de 10 m*l*. De plus, les images montraient clairement la région des poumons de l'animal ainsi que le poumon où le fluide avait été instillé.

La phase de réabsorption de l'oedème pulmonaire a été mesurée par la TIE au cours des quatre heures qui ont suivi l'instillation du fluide dans un poumon, pour ensuite être comparée aux résultats obtenus par l'analyse de l'eau résiduelle dans les poumons extraits de l'animal. Les résultats indiquent qu'il y a une dérive importante dans les données de TIE au cours de cette période, ce qui rend la comparaison imprécise. Il est possible que cette dérive soit due au design électronique du système d'acquisition de données; elle pourrait être corrigée dans une nouvelle version de ce système qui est en cours de développement.

0.5 Conclusions

Bien que plusieurs questions soient encore sans réponses relativement à l'interprétation des images de TIE et à la précision de cette technique dans des conditions expérimentales et cliniques, cette thèse permet de tirer certaines conclusions.

• **Reconstruction d'images.** Les algorithmes de reconstruction d'images qui ont été développés permettent à la fois un calcul rapide de l'image et la prise en compte de la configuration et du niveau de bruit du système de mesure. De plus, ces algorithmes sont relativement insensibles aux variations de la position des électrodes et de la forme du thorax.

• **Validation expérimentale.** Il est possible de mesurer par TIE certains paramètres de la fonction respiratoire pendant des périodes relativement courtes (moins d'une heure) avec une précision suffisante pour les besoins cliniques. Le développement de systèmes d'acquisition de données plus stables devrait permettre d'accroître sensiblement la période utile de surveillance.

TABLE OF CONTENTS

LIST OF TABLES

LIST OF FIGURES

LIST OF SYMBOLS AND ABBREVIATIONS

ε	Relative permittivity
ε_O	Permittivity of free space = 8.85×10^{-12}
Γ	Boundary of conducting medium
μ	Regularization parameter
σ	Conductivity
σ	Standard deviation
$\boldsymbol{\sigma}$	Vector describing the conductivity distribution in each finite element of a medium
σ_h	Vector describing the conductivity distribution of a homogeneous medium
σ_x	Mechanical stress parameter
σ_y	Mechanical stress parameter
ρ	Electric charge density
ϕ	Error function
τ_{xy}	Mechanical stress parameter
ν	Poisson's ratio
Ω	Arbitrary conducting medium
ω_O	Maximum spatial frequency possible in the reconstructed image
$\mathbf{A}$	Diagonal matrix of FEM element areas
ANN	Artificial Neural Network
AP	Anterior-Posterior dimension
APD	Anterior-Posterior Displacement
$\boldsymbol{B}$	Vector magnetic field
$\mathbf{B}$	Image reconstruction matrix
$\mathbf{B}_{10}$	MAP reconstruction matrix with spatial filter of 10 percent diameter
$\mathbf{B}_{20}$	MAP reconstruction matrix with spatial filter of 20 percent diameter

$\mathbf{B}_5$ MAP reconstruction matrix with spatial filter of 5 percent diameter

$\mathbf{B}_{\text{ebp}}$ Image reconstruction matrix corresponding to the technique of Barber (1987)

$\mathbf{B}_{\text{I}}$ Image reconstruction matrix corresponding to the technique of Yorkey (1987)

$\mathbf{B}_{\text{Q}}$ Image reconstruction matrix corresponding to the technique of Woo (1993)

BR   Blur radius; a figure of merit for the reconstructed image resolution

$\mathbf{C}$ Current injection matrix for FEM

$\mathbf{d}_k$ EIT training image vector corresponding to $\mathbf{f}_k$

E Modulus of elasticity

E Electric field

EIT   Electrical Impedance Tomography

$\mathbf{F}$ Spatial filter matrix

$\mathbf{f}$ Dynamic measurement vector (used in chapter 3); equivalent to $\mathbf{z}$

f Parametrization of conductivity distribution

f Probability distribution function

$\mathbf{F}(\boldsymbol{\sigma})$ Vector of simulated EIT measurements for a conductivity distribution $\boldsymbol{\sigma}$

FEM   Finite Element Method

$\mathbf{f}_k$ Dynamic measurement vector for training the ANN

$\mathbf{H}$ Sensitivity matrix, a linearization of the forward conductivity problem

$\boldsymbol{J}$ Vector current density

$\boldsymbol{J}_c$ Conduction current density

$\boldsymbol{J}_d$ Displacement current density

$\boldsymbol{J}_{\mathbf{n}}$ Normal current density at a boundary

K   Gain factor in calculation of Probability of error

k Conversion factor from fluid volume to EIT image magnitude

L Ratio of lateral to AP displacement

LD   Lateral Displacement

M   Movement fraction

M   Number of image elements

MAP   Maximum A Posteriori

N   Number of independent EIT measurements

N   Neural network image reconstruction matrix; (used in chapter 2); equivalent to **B**

NF   Noise figure; a figure of merit for the reconstructed image noise performance

n   Normal vector to boundary

n   Vector of measurement noise in the signal, **x**

$P(\varepsilon)$ Probability of error; chance of non-detection of a target contrast

PE   Pulmonary edema

PE   Position error; a figure of merit for the reconstructed precision of target location

Q   Spatial filter estimate for the inverse of $\mathbf{R}_x$

QG   Quantative Gain; a figure of merit for the reconstructed image amplification

r   EIT image vector; (used in chapter 2); equivalent to **x**

$\mathbf{R}_n$ Prior model of the covariance of **n**

ROI   Region of Interest

$\mathbf{R}_x$ Prior model of the covariance of **x**

S   Sensitivity matrix; (used in chapter 2); equivalent to **H**

SNR   Signal to Noise Ratio

s_O output signal from communication channel

T[ ]   Transformation function from FEM voltage calculation to EIT measurements

u   Displacement in the *x* direction

u   Vector of EIT potential measurements without the effect of geometrical errors

V   Electric Potential (Voltage) distribution

V	Matrix of electric potential calculated by the FEM
v	Displacement in the *y* direction
v	Vector of EIT potential measurements
W	Noise variance cross-correlation matrix
x	EIT image vector; parametrization of the change in conductivity distribution
$\mathbf{x}_\infty$	Maximally smooth prior estimate for **x**
$\hat{\mathbf{x}}$	MAP Estimate of **x**
Y	Admittance matrix for FEM
Z	FEM model of EIT measurement signal
Z	Image reconstruction matrix; (used in chapter 3); equivalent to **B**
z	Measurement signal vector; describes a change in EIT measurements

CHAPTER 1:
INTRODUCTION

1.1   Introduction

The laws of physics state that in order to investigate the structure or function of a medium, it is necessary to inject energy into the medium, and then measure the interaction between the medium and the energy. Medical technology has well explored this physical law by finding many different ways to inject energy into a medium, including x-rays, ultrasound, radio-isotopes, and others.   Electrical impedance tomography (EIT) continues this "tradition" by injecting electrical current and measuring the voltage distribution produced.

EIT uses audio frequency electrical stimulation as an "energy beam" which interacts with a medium of interest producing a voltage distribution which is measured using electrodes on the medium surface. Because the voltage at the electrodes depends on the geometry of the medium and on the distribution of electrical impedance within the medium, one can work backwards from a knowledge of these voltage measurements and the medium geometry to an estimation of the impedance distribution.

Although, in itself, the electrical impedance distribution within a tissue is not of much clinical interest, the different tissues and fluids in the body have characteristic electrical impedances, and can potentially be distinguished on that basis. Various physiological activities can be imaged by the changes in impedance distribution associated with the activity.

Although, in its present state, EIT does not offer the resolution necessary to become a general tool as has become computed tomography (CT) and magnetic resonance imaging (MRI), EIT shows clinical promise in various areas. It has the advantage of requiring a relatively compact measurement system, a personal computer level of computing power, and a minimally cumbersome means of attaching to a patient.

Due to the limited spatial resolution currently available, EIT does not show much promise for *anatomical* imaging, but rather for *functional* imaging. An anatomical imaging process is one in which the aim is to identify the forms and locations of structures within the body; while presently available EIT systems can easily locate organs like the lungs and heart, they cannot clearly identify their shape nor any of the detailed structure within the organs. On the other hand, a functional imaging process aims to measure the comportment over time of physiological processes. The resolution requirements of a functional type of imaging are much reduced; the goal is typically to quantify the action, or to monitor changes in organ function over time and in response to other stimuli.

In order to use EIT for studying a particular physiological phenomenon, it is necessary that the phenomenon be associated with a change in impedance. Fortunately, this is true of many functions of clinical interest. Impedance changes are associated with fluid and gas movement in the body, thus respiration, circulation, and digestive system activity are visible to EIT.

Perhaps the most promising application for EIT is in the area of monitoring lung function. The phenomena of interest, lung ventilation, lung perfusion, and extravascular fluid presence, are associated with the movement of conductivity contrasting fluids, and induce large changes in the conductivity distribution of the thorax. One significant advantage of EIT over other imaging modalities in that, being non-invasive and minimally cumbersome, it could continuously monitor a patient over long periods.

1.2 Objectives

The feasibility of monitoring pulmonary function using EIT is investigated in this thesis. This investigation can be divided into three sections: reconstruction of EIT images while taking into account the experimental conditions, physiological modelling of data acquisition in order to interpret reconstructed conductivity changes, and experimental evaluation of the technique.

1.2.1   Image Reconstruction

Much work has been accomplished in image reconstruction for EIT; however, the many practical realities of data acquisition in a clinical environment are only beginning to be dealt with in the literature. These difficulties include the non-circular geometry of the thorax, variability in electrode spacing, varying levels of measurement noise, and the possibility of faulty measurement channels. The techniques developed in this thesis focus on taking into account these difficulties in experimental conditions while providing computationally inexpensive image reconstruction.

The first approach developed to deal with this problem used an artificial neural network (ANN) approach to reconstruct images. The advantage of the ANN is the ability to develop a "model" without requiring an explicit mathematical relationship. A simulated "training set" of inhomogeneities in a medium and the EIT measurements produced from this set was used to train an ANN to reconstruct the conductivity distribution from the measurements. By adjusting the noise level during the training process, it was possible to control the noise performance of the resulting ANN.

This work is described in the article "A Neural Network Image Reconstruction Algorithm for Electrical Impedance Tomography", by A. Adler and R. Guardo, published in the IEEE Transactions on Medical Imaging (December 1994, pp. 594-600). The text of this article comprises chapter 3.

Another image reconstruction approach was developed based on a finite element model (FEM) of the forward problem with a *maximum a posteriori* (MAP) formulation (also known as a Baysian formulation) of the image reconstruction. The FEM allows a modelling of an arbitrary geometry, and the MAP formulation states the problem in terms of probabilistic assertions about the original conductivity distribution, measurement system, and measurement noise. This allows a natural *interpretation* of known system information in terms of the model parameters. For instance, a defective measurement channel indicates a high probability of error on data acquired from that channel.

In order to evaluate the success of this image reconstruction model, certain figures of merit are developed. The quality of the image is measured by the *blur radius* (a measure of the resolution) and the *position error* (a measure of the fidelity of the position

of reconstructed targets). The algorithm performance with respect to measurement noise is measured by the *noise figure* (a measure of the amplification of noise by the image reconstruction process), and the probability of detection of a contrast.

This work is described in the article "Electrical Impedance Tomography: Regularized Imaging and Contrast Detection", by A. Adler and R. Guardo, which has been accepted for publication in the IEEE Transactions on Medical Imaging. The text of this article comprises chapter 4. Annex A compares the ANN and MAP reconstruction techniques.

1.2.2 Physiological Modelling

Use of EIT in a clinical environment implies the interpretation of images. Ideally, the image reconstruction algorithms would take into account all anatomical and measurement configuration details, but in practice this has not been possible. For example, there currently exist no imaging algorithms that take into account the presence of anisotropy, or the movement of electrodes due to posture changes and breathing. This indicates that the images of *in vivo* conductivity changes are subject to certain errors.

In the absence of ways to eliminate these error sources, it is important to understand their magnitude and effect in order to interpret images appropriately. Analysis of the problem of electrode movement due to breathing was undertaken because it seemed to be the most pressing problem for EIT measurement of pulmonary function.

A two dimensional anatomical finite element model of the mechanical properties of the thorax was used to simulate the movement of electrodes and anatomical structures due to breathing. This mechanical data was then used in conjunction with tissue electrical properties to simulate the EIT measurements at end-expiration and end-inspiration, from which images were reconstructed. Results indicate that electrode movement due to breathing contributes significantly to reconstructed images, and a normalized image interpretation scheme to reduce the effect was proposed.

This work is described in the article "Impedance Imaging of Lung Ventilation: Do we need to account for Chest Expansion?", by A. Adler, R. Guardo, and Y. Berthiaume,

which has been accepted for publication in the IEEE Transactions on Biomedical Engineering. The text of this article comprises chapter 5.

1.2.3   Experimental Evaluation

It is, of course, important in a feasibility study of pulmonary monitoring by EIT to experimentally evaluate the technique. A series of experiments on dogs was undertaken to determine the ability of EIT to measure certain lung processes. Lung tidal volume and the quantity of fluid instilled into a lung were measured, while the ability of EIT to image conductivity changes was verified by the identification of the lung subject to fluid instillation. Results indicate that EIT is capable of determining the instilled lung, and show a strong linear correlation between the quantities measured by EIT and the magnitude of lung ventilation and fluid instillation. The average error for EIT measurement of lung ventilation was determined to be 90 ml, while the error for instillation measurement was 10 ml. Additionally, the reabsorbtion phase of pulmonary edema (PE) was measured by EIT and compared to the results obtained from gravimetric analysis of the extracted lungs. Results indicated the presence of significant drift in the EIT data over time making the comparison inaccurate. These results are presented in chapter 6.

CHAPTER 2:
BACKGROUND

2.1   Electrical Impedance Tomography

Electrical Impedance Tomography (EIT) is an imaging technique which calculates the electrical conductivity distribution within a medium from electrical measurements made at a series of electrodes on the medium surface.   EIT data is acquired by successively applying a low amplitude audio frequency current across each pair of electrodes while measuring the voltage differences produced on all the other pairs of electrodes.   The measurement system used for these experiments has 16 electrodes; for each current pattern, there are 13 electrode pairs not used for current application at which the voltage is read.   At each pair of electrodes, a difference signal is calculated by subtracting one voltage from the other and then amplifying the result.   The data collected is then sent to the imaging system where it is processed.   Figure 2.1 summarises this process.
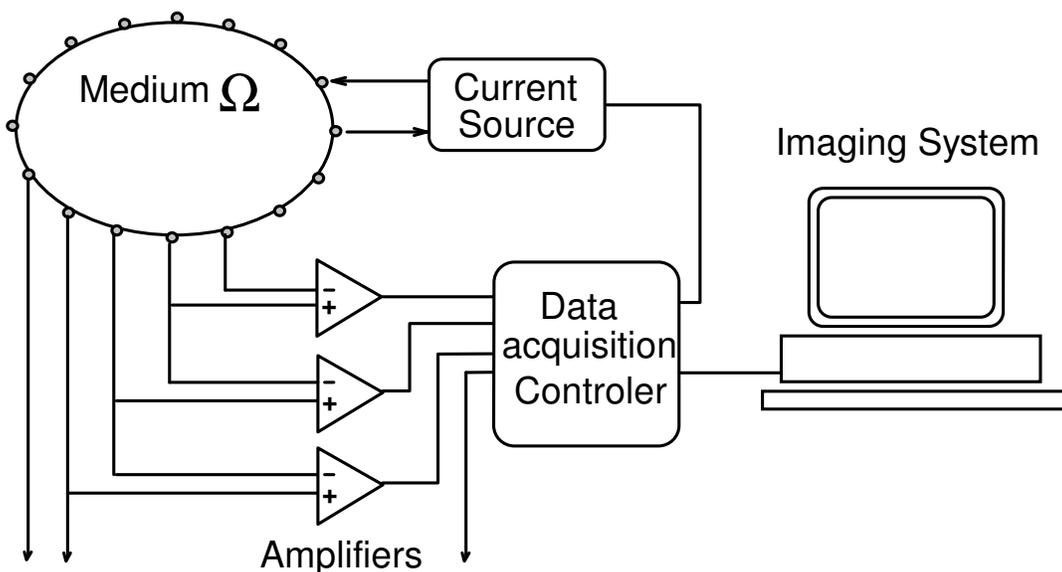
Figure 2.1: Block Diagram of a typical EIT system.

Inside the data acquisition controller these difference signals are demodulated and read by a digital to analog converter.   The demodulation reads the amplitude of the measured difference signal while removing electrical signals produced by physiological

processes (such as the ECG) by rejecting all contributions to the signal which are not at the frequency of current injection. After current injection and voltage reading are applied across all electrode pairs there are a total of 13×16 = 208 values read, which are sent to a computer which calculates the EIT image. This data set represents the conductivity distribution of the subject at the time of data acquisition.

EIT poses no known electrical risk to the patient. Studies of the cutaneous sensitivity of humans to electrical stimulation as a function of frequency (Dalziel, 1956; Geddes, 1971) indicate that, while the sensitivity is quite high to current at low frequencies, it decreases significantly with increasing frequency. In experimental work in this thesis the current used was approximately one tenth of the level required for cutaneous perception by the most sensitive percentile of the population. The current levels required to cause muscle contraction for cutaneous current injection are more than ten times higher than the perception values.

2.2   Physics of the problem

An arbitrary medium undergoing electrical stimulation, Ω, has electrical properties that vary as a function of position and time. We represent these properties by the electrical conductivity $\sigma(x,y,z,t)$ and relative permittivity $\varepsilon(x,y,z,t)$. Outside the medium there is no current flow because the conductivity is zero. Energy is applied to the medium in the form of current injection on the boundary, which sets up a distribution of voltage and a pattern of current flow in the medium.

Within the medium there is an electrical field $\boldsymbol{E}(x,y,z,t)$ which induces a current

$$\boldsymbol{J} = \boldsymbol{J}_c + \boldsymbol{J}_d$$

$$J_c = \sigma E$$

$$J_d = \varepsilon\varepsilon_o \frac{dE}{dt}$$

(2.1)

where $\boldsymbol{J}_c$ is the conduction current flow, $\boldsymbol{J}_d$ the displacement current, and ε_o is the physical constant 8.85×10^{-12} coul^2/N-m^2, the permittivity of free space.

Because the excitation of the medium is sinusoidal, we can represent the electrical field as the phasor $\boldsymbol{E}$, and the current phasor, $\boldsymbol{J}$, as a function of $\boldsymbol{E}$.

$$E(x, y, z, t) = \mathbf{E}(x, y, z)e^{-j\omega t} \tag{2.2}$$

$$\mathbf{J} = \mathbf{J}_c + \mathbf{J}_d = (\sigma - j\omega\varepsilon\varepsilon_o)\mathbf{E} \tag{2.3}$$

The expression $(\sigma - j\omega\varepsilon\varepsilon_o)$ represents the complex admittance (or the inverse of the impedance) distribution of the medium. Often, it is assumed that the reactive component is small with respect to the conductive ($\sigma \ll \omega\varepsilon\varepsilon_o$) in which case the medium can be modelled by real valued conductivity, σ.

In order to formulate this problem in terms of an electric potential, V, such that

$$E = -\nabla V \tag{2.4}$$

we need to be able to assume that $\nabla \times E = 0$. In general, Faraday's law states that

$$\nabla \times E = -\frac{\partial B}{\partial t} \tag{2.5}$$

where B is the magnetic field vector. According to the analysis of Davey (1991), the quasi-electrostatic assumption that the magnetic field is constant is valid for injection frequencies up to 1 MHz. Since EIT systems are within this limit, the potential formulation can be used.

Additionally, because the medium is conductive, there will be no local charge build up and the charge density, ρ, is zero. The continuity equation, therefore becomes

$$\nabla \bullet J = -\frac{\partial \rho}{\partial t} = 0 \tag{2.6}$$

Combining equations 2.3, 2.4, and 2.6, we obtain

$$\nabla \bullet (\sigma - j\omega\varepsilon\varepsilon_o)\nabla V = 0 \qquad \text{in } \Omega \tag{2.7}$$

The boundary conditions on Γ, the boundary of Ω, are formulated by fixing the normal current at every point of Γ. Representing the normal vector by $\mathbf{n}$, we have

$$J_{\mathbf{n}} = -(\sigma - j\omega\varepsilon\varepsilon_o)(\mathbf{n} \bullet \nabla V) = -(\sigma - j\omega\varepsilon\varepsilon_o)\frac{\partial V}{\partial \mathbf{n}} \qquad \text{on } \Gamma \tag{2.8}$$

Together, equations 2.7 and 2.8 may be used to find the voltage distribution within the medium, after fixing the voltage reference at some arbitrary point in the

medium. Two techniques have been used to solve these equations: analytic techniques, and numerical simulation. Analytical solutions to these equations typically use series approximations (Isaacson, 1986; Chen, 1992; Shaw, 1993) or conformal mapping (Barber, 1985). While important from a theoretical point of view, analytical techniques are only able to deal with single circular inhomogeneities in a circular medium. Numerical simulation using finite element or finite difference techniques is used by most groups investigating EIT (Yorkey, 1987; Cheney, 1990; Woo, 1993; Adler, 1993; Schuessler, 1994; Hua, 1988; Barber, 1992), because it allows the most general approach to the problem, including the simulation of a non circular medium with arbitrary inhomogeneities.

2.3   Image Reconstruction

There are two categories of reconstruction methods which have been proposed for EIT: *static* and *dynamic* reconstruction techniques. Static reconstruction produces an image of the conductivity distribution in a medium based on one set of data, while dynamic image reconstruction produces an image of the change in conductivity distribution between the acquisition times of two data sets.

2.3.1   Static Image Reconstruction

Static reconstruction in EIT has been proposed by various groups (Yorkey, 1987; Cheney, 1990; Woo, 1993). The basic technique used is the modified Newton-Raphson algorithm proposed by Yorkey (1987), a block diagram of which is shown in figure 2.2. This technique uses a finite element model of the medium to simulate the voltage measurements from the physical medium. Initially, the medium is assumed to be homogeneous, and subsequently, using an iterative procedure, the conductivity distribution is modified to better simulate the measured data. Iteration is stopped when the simulated data sufficiently well approximates the "real" data.
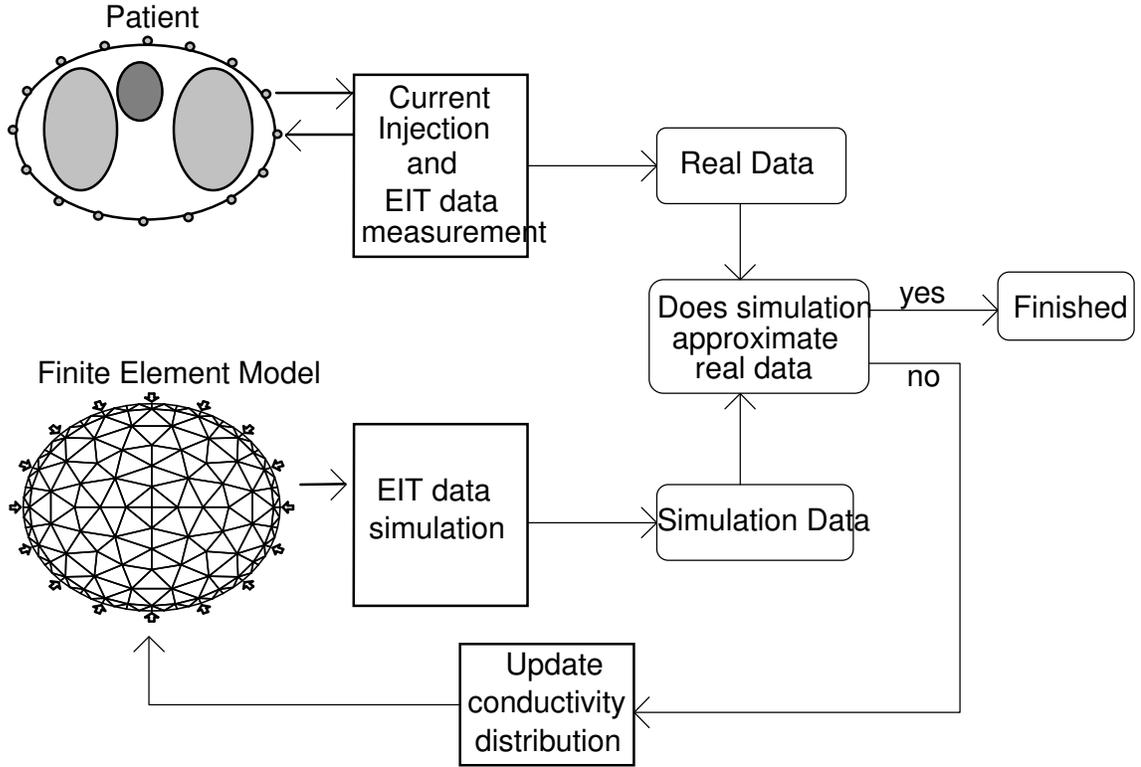
Figure 2.2: Modified Newton Raphson Algorithm

Yorkey's technique functions as follows: Given a vector of voltage measurements from the physical medium $\mathbf{v}$, and a finite element model $\mathbf{F}(\boldsymbol{\sigma})$ which simulates the voltage measurements from a medium with conductivity distribution $\boldsymbol{\sigma}$, we define an error function ϕ such that

$$\phi = \tfrac{1}{2}\sum_i \left(\mathbf{v}_i - \mathbf{F}_i(\sigma)\right)^2$$

(2.9)

The desired reconstructed conductivity distribution is the value of $\boldsymbol{\sigma}$ which minimises ϕ. At this point the derivative of ϕ with respect to $\boldsymbol{\sigma}$ will be zero.

$$\frac{\partial \phi}{\partial \sigma_j} = \sum_i \frac{\partial F_i(\sigma)}{\partial \sigma_j}\left(\mathbf{v}_i - F_i(\sigma)\right) = 0$$

(2.10)

Since   is a non-linear function, we use a Taylor expansion to find a linear approximation of ϕ' for a perturbation, $\Delta\boldsymbol{\sigma}^k$, about a conductivity distribution $\boldsymbol{\sigma}^k$

$$0 = \frac{\partial \phi}{\partial \sigma_j} = \frac{\partial \phi}{\partial \sigma_j}\left(\sigma^k\right) + \sum_i \left(\frac{\partial^2 \phi}{\partial \sigma_j \partial \sigma_i}\right) \Delta \sigma_i^{\ k}$$

(2.11)

The Hessian matrix ϕ'' can be approximated by

$$[\phi'']_{ij} = \frac{\partial^2 \phi}{\partial \sigma_j \partial \sigma_i} = \sum_l \left(\frac{\partial F_i(\sigma)}{\partial \sigma_l}\right)\left(\frac{\partial F_j(\sigma)}{\partial \sigma_l}\right)$$

(2.12)

where the summation is calculated for all conductivity elements, l. Using this expression, the value of $\Delta \sigma^k$ which minimises the approximation of ϕ may be calculated.

$$\Delta \sigma^k = -[\phi'']^{-1}[\phi']^t(\mathbf{F}(\sigma) - \mathbf{v})$$

(2.13)

Starting with an initial homogeneous conductivity estimate, σ^o = constant, $\Delta \sigma^k$ is used to update the conductivity distribution at each iteration.

$$\sigma^{k+1} = \sigma^k + \Delta \sigma^k$$

(2.14)

One of the problems associated with the iterative technique is its instability. It is not uncommon for an iterative procedure to produce physically unrealistic reconstructed images by either estimating negative conductivity values or by diverging toward infinite ones. This instability is caused either by measurement noise (Schuessler, 1994), or by geometrical errors, such as reconstructing data from an elliptical phantom on a cylindrical finite element model. Some improvement in this instability may be achieved by adding a regularizing term to the Newton-Raphson technique (Yorkey, 1987; Adler, 1993). Using the regularization formulation, the error function in equation 2.9 is replaced by:

$$\phi = \frac{1}{2}\left(\sum_i (v_i - F_i(\sigma))^2 + \mu \sum_j Q_{jj} \sigma_j^{\ 2}\right)$$

(2.15)

where the diagonal matrix $\mathbf{Q}$ and the parameter μ represent *a priori* information about the geometry of the medium and the noise in the measurements. These regularization parameters are typically assigned values by heuristic considerations. A variation on this approach is proposed by Cheney (1990) where only one iteration is used, allowing an increase in computational speed which compensates for the reduced accuracy.

Many reconstruction techniques do not attempt to calculate the conductivity distribution everywhere, but use a priori geometrical information to restrict the number of

unknowns (Newell, 1992; Woo, 1993). In these studies, a small number of unknown conductivities, such as for the heart, left and right lung, spine, and surrounding tissue will be assigned to the corresponding organs. Image reconstruction then takes the form of a constrained least squares minimisation to find these parameters. The advantage of this technique is the stability which is gained from reducing the number of parameters calculated. It is no longer necessary to use regularization techniques because the problem is no longer under-determined. Unfortunately, this technique is subject to the sensitivity of EIT to geometrical errors. Small errors in the geometrical information (the shapes of the organs or the position and size of electrodes) can have a large effect on the reconstructed conductivity values.

Besides the modified Newton-Raphson algorithm, the only other static reconstruction algorithm to be proposed is the layer stripping technique (Cheney, 1992). This technique reconstructs the conductivity distribution by first calculating the distribution in a "layer" of medium directly in contact with the surface, and subsequently using this distribution to calculate the conductivity of the next innermost layer, continuing until all "layers" in the medium have been calculated. The layer-stripping technique is not iterative like the Newton-Raphson, in that the conductivity of any area, once calculated, is not subsequently updated. At this time, the layer stripping technique does not seem to have been used with experimental data, and its potential is difficult to determine.

In general, static reconstruction algorithms suffer from a high sensitivity to measurement error, as pointed out by Barber (1988), due to EIT being more sensitive to changes near the medium surface than it is to changes within the medium. In order for static image reconstruction to be reliable, it is essential that the following error sources be carefully controlled:

• **Electrode positioning:** This presents the largest source of systematic error in the data, and unfortunately, tends not to be present in simulation studies which often use the same geometry for simulating the medium as for reconstructing the conductivity. The positioning of electrodes on the thorax of a patient can be especially problematic, as rhythmic movement due to breathing tends to cause the electrodes to move (Adler, 1994). This type of problem can be solved by using a rigid electrode frame, in which the electrode positions can be located with high precision, and held in contact with the patient

using a conductive foam or saline solution (Guardo, 1990). A rigid frame has the disadvantage, however, of being more cumbersome.

- **Variance between channels in the data acquisition hardware:** Due to component variability and ageing, it can be difficult to keep the characteristics of all data acquisition channels the same. It is possible to account for this error by systematically calibrating the hardware before every experiment.

- **Electrode contact area and contact resistance:** These problems are especially difficult when attaching electrodes to a patient, as movement and perspiration of the skin, and drying of the electrodes tend to change these properties.

2.3.2 Dynamic Image Reconstruction

The advantage of dynamic reconstruction is the ability to reduce the effect of many of these sources of error by looking at the effect of changes in conductivity on changes in measurements. Since even large changes in the medium produce changes in measurements that are relatively small compared to the measurements from the background conductivity distribution, the forward problem can be separated into a static and a dynamic component, where the dynamic component is assumed to be a linear function of the conductivity change.

$$\mathbf{v}_h + \Delta \mathbf{v} = \mathbf{F}(\sigma_h) + \mathbf{H} \Delta \sigma$$

(2.16)

where $\mathbf{v}_h$ is the voltage measurements from a homogeneous medium, $\mathbf{F}(\sigma_h)$ is a function of the homogeneous conductivity distribution, $\Delta \boldsymbol{\sigma}$ is the change in conductivity distribution, $\Delta \mathbf{v}$ is the change in measurements, and $\mathbf{H}$ is a "sensitivity matrix" describing this linear relation. Since the function $\mathbf{F}(\sigma_h)$ is difficult to calculate due to the sources of error discussed, its effect can be ignored by concentrating only on the changes ($\Delta \mathbf{v}$ and $\Delta \boldsymbol{\sigma}$). Of course, being a linear approximation, dynamic imaging is only valid in a limited range, but still represents a very good technique for many problems. Barber (1988) has shown that dynamic imaging is relatively insensitive to errors in electrode placements as long as these remain constant during the experiment.

Dynamic image reconstruction was used in the first EIT reconstruction technique proposed by Barber (1985), Equipotential Backprojection. This technique, by analogy

with CT backprojection reconstruction, calculates a number of "stream lines" which cover the region affecting any given electrode. Each equipotential region is the area in a homogeneous medium in which the electric potential is between that of two corresponding adjacent measurement electrodes. Figure 2.3 illustrates the equipotential region corresponding to measurement electrodes M^+ and M^- during the current injection pattern at electrodes I^+ and I^-. Image reconstruction using this technique projects the change in measurement at each electrode pair across the equipotential region for that current injection pattern.
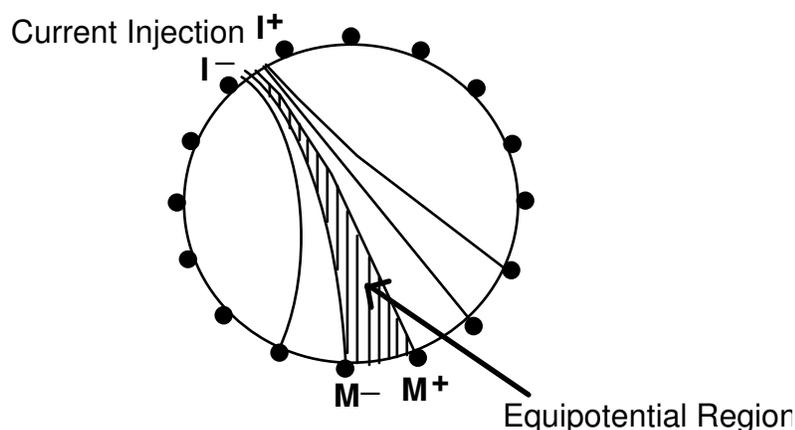
Figure 2.3: Equipotential backprojection regions for a measurement configuration.

Although backprojection has received theoretical support in the work of Santosa (1990), it has several problems. It is limited to a circular medium geometry, and current injection across adjacent electrodes. From a performance point of view, backprojection "pushes" reconstructed target positions towards the centre of the medium, and tends to produce streak-like artefacts in the image. Barber (1992) has since introduced a "filtered backprojection" algorithm, which can be understood as a type of sensitivity matrix technique.

Sensitivity matrix techniques have been introduced by various groups (Barber, 1992; Barber, 1988; Gencer, 1992) and perhaps can be best understood in terms of adaptive filter theory. Defining the *signal* as the change in measurement due to a change in conductivity, one can calculate a set of basis signals $\mathbf{z}_j$, $1 \leq j \leq N$, where N is the number of pixels in the image. Each signal corresponds to a small change in conductivity in a pixel:

$$\mathbf{z}_j = \frac{\mathbf{z}(\sigma_h) - \mathbf{z}(\sigma_h + \delta_j)}{\delta_j} = \frac{\partial \mathbf{z}}{\partial \sigma_j}(\sigma_h)$$

(2.17)

where $\mathbf{z}(\sigma_h)$ is the signal from a homogenous medium, and $\mathbf{z}(\sigma_h + \delta_j)$, the signal from an almost homogeneous medium with a small perturbation in pixel j. This set of signals forms a basis for the mapping of an image onto a measurement, and defines the sensitivity matrix $\mathbf{H}$ for the reconstruction, $\mathbf{H} = [\ \mathbf{z}_1\ \ \mathbf{z}_2\ \ ....\ \ \mathbf{z}_N]$. Within the region of validity of the linear approximation, the signal can be considered to be a superposition of signals from each pixel's conductivity change. Thus, the signal due to a vector $\mathbf{\Delta\sigma}$ of conductivity changes in each pixel is:

$$\mathbf{z} = \mathbf{H}\Delta\sigma$$

(2.18)

Given an unknown conductivity change, we can calculate the signal, $\mathbf{z}$, corresponding to this change, and can then decompose this signal into image components by finding the length of its projection on to each basis signal $\mathbf{z}_j$. The value of the image pixel at j is $\mathbf{I}_j$:

$$\mathbf{I}_j = \frac{\mathbf{z} \bullet \mathbf{z}_j}{\left\| \mathbf{z}_j \right\|}$$

(2.19)

This image reconstruction technique is very robust to image noise and produces reasonable quality images. However, due to the non-orthogonality of the signals in the basis, $\mathbf{H}$, these techniques do not have the resolution that can be obtained using regularized inverse techniques.

Several groups have proposed imaging techniques based on regularization (Hua, 1988; Adler, 1993; Shaw, 1993). An original conductivity change, $\mathbf{x}$, is defined to produce a signal $\mathbf{z}$ by the EIT measurement process $\mathbf{z} = \mathbf{H}\mathbf{x}$, and an estimate $\hat{\mathbf{x}}$ of $\mathbf{x}$ is calculated by minimising the error function, ϕ, with respect to $\mathbf{x}$,

$$\phi = (\mathbf{z} - \mathbf{H}\mathbf{x})^t\, \mathbf{W}(\mathbf{z} - \mathbf{H}\mathbf{x}) + \mu(\mathbf{x} - \mathbf{x}_\infty)^t\, \mathbf{Q}(\mathbf{x} - \mathbf{x}_\infty)$$

(2.20)

where $\mathbf{H}$, $\mathbf{W}$, $\mathbf{Q}$, μ and x_∞ are determined using *a priori* knowledge of the physics and geometry of the problem. Each proposed algorithm has used different heuristic arguments to assign values to these parameters. In terms of these parameters the estimate $\hat{\mathbf{x}}$ which minimises the error is

$$\hat{\mathbf{x}} = \left(\mathbf{H}^t\mathbf{W}\mathbf{H} + \mu\mathbf{Q}\right)^{-1}\left(\mathbf{H}^t\mathbf{W}z + \mu\mathbf{Q}x_\infty\right)$$

(2.21)

By using regularization, the EIT problem can be inversed using algebraic techniques. The parameter μ controls the amount of regularization in the inverse solution. Regularization allows control of the compromise between the noise performance and the resolution of the image. Reconstruction using a low value of μ has a higher resolution (is better able to resolve two image targets close together) but poorer rejection of measurement noise, while a larger μ is able to better deal with the noise at the expense of poorer resolution.

The advantage of the regularization formulation is its theoretical support, and the ability to adjust a number of parameters to take into account *a priori* information about the problem. Additionally, the inverse matrix can be precomputed, requiring only a matrix multiplication during image reconstruction, allowing regularization techniques to be as fast as other dynamic inverses.

Another dynamic imaging technique uses artificial neural networks (ANN) to image EIT data (Guardo, 1991; Adler, 1993; Adler, 1994). In these techniques, an ANN is "trained" with a set of EIT measurements and the (known) conductivity distribution from which the measurements were generated. These training sets can either be simulated (Adler, 1994; Adler, 1993), or measured experimentally (Guardo, 1991). The image reconstructions produce a good compromise of resolution and noise performance, but seem to be generally more sensitive to noise than other image reconstruction techniques. The advantage of neural networks is the conceptual simplicity and the ease of implementation, while the disadvantage is the large computation time required to train the neural network, and the lack of a theoretical interpretation of the results. Even once the network has been trained, it is specific to one problem geometry, and must be retrained for any change in the experimental condition.

One disadvantage of all dynamic imaging techniques is the unwarranted assumption on the background conductivity distribution that must be made. In order to reconstruct the change in conductivity from two sets of data, a sensitivity matrix is used which has been calculated about an assumed "average" conductivity distribution, normally a homogeneous one. The dynamic imaging technique assumes that only the

change in conductivity, and not the "background" conductivity distribution, affects the measured voltage differences. This assumption is not valid in the case of a thorax which has a very inhomogenous conductivity distribution, about which small changes take place.

2.4   Image Interpretation

Various practical difficulties affect EIT image interpretation *in vivo*. These include the three dimensional extent of the medium above and below the measurement plane, the presence of anisotropically conducting tissues, and the movement of electrodes due to breathing and posture changes. The approach taken by most groups has been to develop more sophisticated image reconstruction techniques to take into account these difficulties. Very little work has been done to determine the effect on the images using available reconstruction techniques, and to guide the image interpretation accordingly.

One assumption which has been used in most image reconstruction techniques is that the reactive component of the complex admittance distribution, $\tilde{\jmath}\quad_o$, can be ignored. However, the reactive component can only be ignored if $\ll\quad_o$, and this condition is only valid for frequencies below 1 kHz in typical biological systems (Plonsey, 1969). Certain groups (for example, Griffiths, 1987) propose imaging changes in the reactive component between two different excitation frequencies. Some authors have proposed an image reconstruction technique which completely separates the in-phase and quadrature voltage measurements and reconstructs two images independently from these (for example see Riu, 1992). This simplification is, unfortunately, unjustified. Both the in-phase and quadrature measurements are functions of both the conductivity and the admittivity distributions.

Another assumption that is typically made by reconstruction algorithms is that the impedance distribution is isotropic. However, in the body, many tissues conduct anisotropically, the most important being the muscles, neural tissue and blood vessels. An investigation by Brekton (1992) uses a differential geometry approach and concludes that anisotropy in the conductivity distribution will have an effect on the positioning of the reconstructed contrasts. Similarly, Eyüboğlu et al. (1992) simulate the effect of anisotropic conductivity in a circular region in an otherwise circular homogeneous

conductor, and calculate a signal due to the change in isotropy of the region. They conclude that this signal is sufficient to perturb the image and must not be neglected in image reconstruction. Karlon (1994), uses a 3D finite element model to study the effect of skeletal muscle anisotropy for simulated transthoracic defibrillation, and concludes that this anisotropy can cause a variation of electrical parameters, such as the electrode to electrode transthoracic impedance, by as much as 50 percent. Some steps toward reconstructing images of the anisotropy have been taken by Glidewell et al. (1993, 1994), who develop a model of the EIT forward problem based on a conductivity tensor formulation for a 3D finite element model of a canine thorax.

Several groups have discussed the effect of variability in electrode positioning. It has been shown that the dynamic imaging approach is significantly more robust in the presence of position errors than the static approach (Barber, 1988; Adler, 1994) as long as the electrodes do not move between the taking of the data sets. In clinical applications, however, there can be significant electrode movement due to breathing or posture changes.

Barber (1990) discusses the importance of accurately modelling the electrode positions and describes an algorithm using the measured EIT data to estimate and correct for these errors. Unfortunately the effect of residual errors in electrode positioning on the images is not discussed. Wolf et al. (1993) present an algorithm based on a 3D finite element model which determines electrode locations and boundary shapes based on impedance measurements. They do not discuss the effects of these errors on the images.
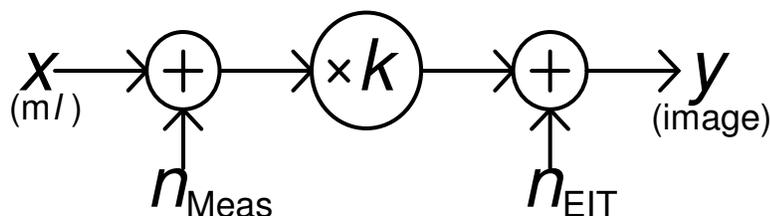
Figure 2.4: Model of EIT image formation and noise

A linear model for interpreting images has been proposed by Trudelle et al. (1995) which allows the image magnitude to be related to target volume. The model used (figure 2.4) describes the formation of an image contrast, y, from a target of volume x as a function of a factor, k, representing the radial position, relative height with respect to the electrode plane, and conductivity contrast of the target. In order to correct for

experimental sources of error, *k* is calculated from the data sets. *In-vitro* results show that the linear model is accurate over a wide range with a mean volume measurement error of 6 ml.

2.5   Clinical Applications

The *raison d'être* of the lung is to move air so that oxygen can enter the blood stream and carbon dioxide can leave. The conductivity of both air and blood contrasts with that of the surrounding tissues, blood being more conductive and air significantly less conductive, indicating that their movement could be measured by EIT. Another conductivity contrasting substance affecting lung function is the fluid leaving the capillaries which, normally, is removed by the lymph, but, under conditions of pulmonary edema (PE) can accumulate in the perivascular space and, eventually, can fill the alveolar spaces.

The magnitude and spatial distribution of the movement of these substances is of clinical interest, and the measurement of these quantities by EIT could possibly provide significant useful information for clinicians and researchers of pulmonary function. For a measurement technique to be clinically useful, it must be able to either provide information which will help in early diagnosis; assist in the decision on the type and degree of treatment; or help to monitor the progression of the pathology to understand its course and the effect of various types of treatments. The following characteristics represent an ideal measurement system for lung function (Leksell, 1991):

- **Accuracy / Repeatability:** Results should not vary depending on the clinician using the apparatus or between two measurements of the same patient.

- **Sensitivity:** The ability to measure small changes is important. For instance, it has been shown that currently available measurements techniques require a fluid increase of 25% before reliable detection of PE. An increased sensitivity would allow earlier detection, and hopefully a better prognosis.

- **Minimal Invasiveness:** This is especially important if a measurement is to be used as part of a patient screening.

- **Inexpensive**

- **Non cumbersome:** In an emergency or an intensive care unit where the patient cannot be easily moved and cannot co-operate with the staff doing the measurements, large, bulky equipment is inconvenient.

- **Imaging capable:** Lung function is rarely uniform but presents significant heterogeneity. A technique which provides a single datum to represent the state of the lungs is not as useful as an image which shows the distribution within the lungs.

The techniques proposed for measurement of pulmonary function can be evaluated with respect to these criteria (Staub, 1980; Leksell, 1991; West, 1992). The following techniques are used in clinical or research environments:

- **Chest radiograph**: This is the standard technique used. A plain film x-ray of the chest is taken and is interpreted by trained clinicians. The procedure has the advantage of minimal invasiveness, minimal cumbersomeness, and relatively low cost. It provides an image of the lungs from which it is possible, to some extent, to identify the pathologies, from characteristic patterns in the images. The disadvantage is the subjective nature of the analysis. X-rays also cannot be used to monitor a patient because the radiation dosage would be excessive.

- **Spirometer:** Tests of ventilatory capacity rely on the measurement of inspired and expired air volumes by spirometer. The measurement of the capacities and flow rates can provide a useful diagnostic to differentiate between various types of lung disease. These tests are limited by the lack of an absolute reference point for lung volume (one cannot, for instance, measure the total lung capacity) and the technique's inability to determine regional differences in ventilation across the lungs.

- **Magnetic Resonance Imaging:** MRI can directly provide 3D images of the proton density (and thus water concentration) in tissue. One special advantage is the ability to reject the contribution of blood fluid (by rejecting moving water), thus allowing measurement of only the lung fluids of interest. The disadvantage of MRI is the cumbersomeness and cost of the apparatus. Since preparing a patient for scanning is a complicated and, in intensive care conditions, a possibly dangerous procedure, it is not possible to monitor a patient's condition with MRI.

- **Nuclear Medicine:** Nuclear medicine images the distribution of a radioactive tracer introduced intravascularly or through the airways. It is moderately invasive because blood samples are needed for calibration. The technique gives a functional representation of the spatial distribution of ventilation and perfusion from the concentration of radioactive events. With the proper selection of the tracer molecule according to its diffusion properties, this technique can provide a measure of many properties of the lung. Nuclear medicine suffers from the fact that the equipment is bulky and the injection of the tracer is an invasive procedure.

- **Positron Emission Tomography:** PET allows the 3D imaging of the distribution of a radioactive tracer with reasonably high precision. By careful selection of the tracer molecule the various volumes of interest can be measured: the blood volume, intravascular volume, and the gas volume. The disadvantage of this technique is the cumbersomeness and the cost of the apparatus. Like the other imaging techniques mentioned, PET cannot be used for monitoring.

- **Indicator dilution:** The method of double indicator dilution allows the measurement of extravascular fluid by measuring the difference in diffusion time between two indicators introduced into the circulation. One of the indicators cannot diffuse through the blood vessel walls, while the other is highly diffusive in all lung tissues. This results in a difference in the effective diffusion volume for each indicator and can be used to calculate lung air and fluid volumes. Indicator dilution is inexpensive and has a reasonable accuracy. It is quite invasive, requiring a catheter for the insertion of the indicators, but in an intensive care environment such a catheter may already be in place. The invasiveness and inconvenience of the procedure means that indicator dilution cannot be used to monitor the state of lung function.

- **Histological Appraisal:** A microscope image of a slice of lung tissue can provide much information about the pathologies of the lung. Since a sample represents the lung condition in one place, it may not be indicative of the overall lung condition. While a trained clinician is able to learn much from this type of study, results do vary from expert to expert, and from sample to sample.

- **Transthoracic Impedance:** In this technique, two electrodes, one above and one below the thorax are used to inject a low amplitude AC current, while another set

of electrodes, placed near to each injection electrode, measures the voltage produced by this current. The voltage read is amplified, demodulated, and the transthoracic impedance value is calculated from the ratio of the demodulated voltage to the injected current magnitude. This impedance value depends on the anatomic and physiological condition of the thorax; it is sensitive to pulmonary activity, cardiac activity, posture, skin moisture, thorax shape and other factors. By carefully analysing the changes in impedance over the cycle times of these activities, various groups have been able to make useful physiological measurements from thoracic impedance data. For instance, Spinale et al. (1989) calculate extra-vascular lung water from the changes in the impedance value during the cardiac cycle. There are several problems with transthoracic electrical impedance, as pointed out by Fien et al. (1979). Firstly, impedance values depend on many factors from which it is difficult to determine the phenomena of interest. Because of the large effect of posture and electrode position on transthoracic impedance values, it is difficult to compare values from different patients and even from the same patient on different days. Additionally, an impedance value in ohms is difficult to relate to physiological quantities. Because of anatomical variations, there is no constant relationship between, for instance, one ohm of impedance change and a given change in air volume in the lungs.

In the light of the "ideal" pulmonary measurement system requirements, EIT shows significant promise. It is non-invasive and minimally cumbersome, requiring only the attachment of several electrodes and wires to the patient. This characteristic could be especially advantageous in an intensive care environment, where continuous monitoring of a patient's condition is desired. EIT is potentially relatively inexpensive, and is capable of producing an (albeit low resolution) cross-sectional image of the thorax. The sensitivity and accuracy of EIT in clinical applications have yet to be determined. In this thesis, these quantities are investigated for two substances, air movement associated with lung ventilation and extravascular fluid presence in pulmonary edema.

2.5.1 Lung Ventilation

Two broad categories of pulmonary diseases can be defined:

- **Obstructive diseases** are caused by an increased resistance to airflow. Distinctions between the various obstructive diseases are blurred; examples include chronic obstructive pulmonary disease (COPD), chronic bronchitis, emphysema, and asthma. Characteristic of these pathologies is a marked reduction in all indices of expiratory flow.

- **Restrictive diseases** are caused by a restriction in the expansion of the lung, due either to alterations in the lung parenchyma, disease of the pleura or the chest wall, or deteriorated neuromuscular control of breathing. These diseases are characterised by a reduced vital capacity and a smaller functional residual capacity (FRC). Examples of these diseases are interstitial pulmonary fibrosis, which increases the rigidity of the lung; pneumothorax, where air in the pleural space restricts the expansion of the lung; and pleural effusion, where the lung is restricted by the presence of pleural liquid.

EIT is a promising tool for the investigation of pathologies of lung ventilation. Some work has been done to evaluate the capability of EIT to measure lung ventilation. In these studies, EIT data was acquired from electrodes around the thorax while lung air volume was measured by spirometer. While results indicate good correlation between the measurements, they were obtained for individual patients, and no systematic work was undertaken to demonstrate whether these results can be reliably repeated.
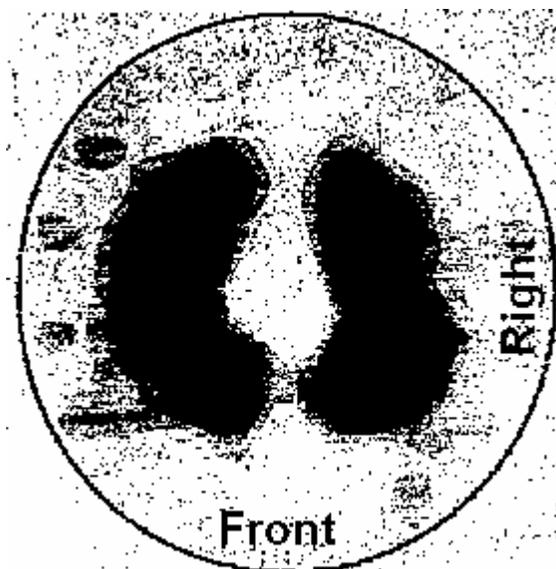
Figure 2.5: From Seagar (1987): Impedance Image at Maximum Inspiration
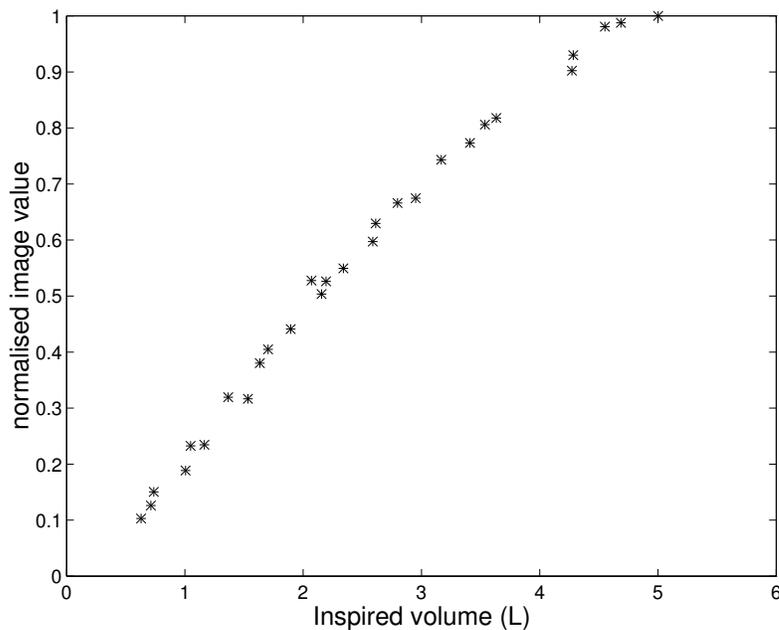
Figure 2.6: From Seagar (1987): Average change in image value over region of lungs as a function of inspired volume.

Seagar et al. (1987) present the results of an experiment to verify the measurement of lung ventilation by EIT. Figure 2.5 shows an image of the impedance change due to maximal inspiration. In this image, the two lungs can be clearly distinguished, but seem to be "pushed" toward the centre of the image compared to a normal anatomical position. They also measure the average image as a function of inspired volume, figure 2.6. This result shows an almost linear relationship between the image magnitude and lung volume.

Newell et al. (1993) measures the image magnitude in each lung during one cycle of inspiration and expiration as a function of the change in lung volume (figure 2.7). These results show a linear correlation between the EIT image magnitude and lung volume measurement, and also demonstrate the possibility of extracting ventilation information separately for each lung.

Clinical studies by Morice et al. (1993), and Campbell et al. (1994) use EIT to study patients with unilateral pleural effusion and pneumothorax. EIT images of normal ventilation were taken prior to therapy, showing conductivity change mostly in the non-affected lung. Subsequently, images were acquired during the aspiration phase of the therapy, showing conductivity changes mostly in the affected lung. They conclude that EIT can be used to measure changes in intrathoracic air content. Unfortunately, the small

number of cases investigated does not allow the question of the reliability of detection of these pathologies to be addressed.
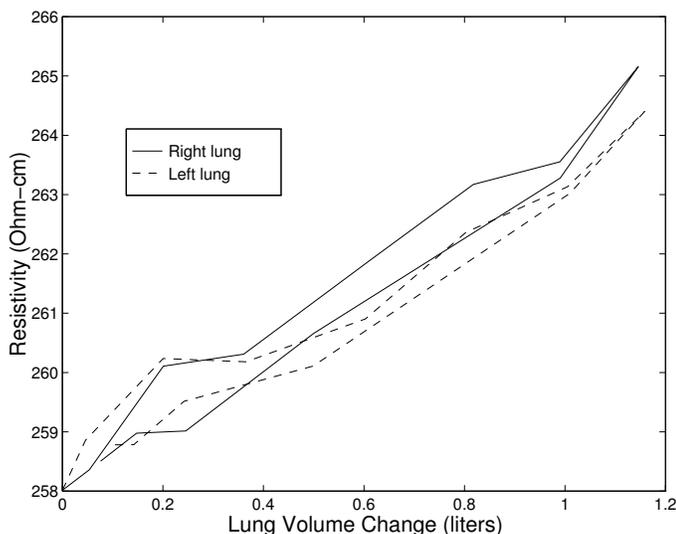
Figure 2.7: From Newell (1993): Peak resistivity in the lung field of a normal human subject increased as air was inspired.

2.5.2 Pulmonary Edema

Pulmonary edema is a pathological condition involving excess fluid in lung tissue. In a normal lung there is a considerable quantity of fluid, which, of course, is not edematous. This fluid is found in the pulmonary circulation, the intracellular fluid, the intravascular fluid, and the pleural fluid. PE results initially in an increase of extravascular fluid, and, as the condition progresses, a movement of fluid into the alveoli. The mechanisms that are involved in the movement of fluid into the lungs are described by the Starling equation which relates the movement of fluids across a boundary to the hydrostatic and osmotic pressures on either side and to the permeability of the boundary. Using this equation, the causes of PE may be classified in two categories:

• **Increased pressure:** An increase in the hydrostatic pressure in the pulmonary capillaries causes an increased flow of fluid into the interstitial spaces and, in severe cases, into the alveoli. Increased capillary pressure can be caused by congestive heart failure or any disease that impairs flow through the lung. Increased pressure edema

can also be due to an increased osmotic pressure due to a reduction in the protein or electrolyte concentration in the blood.

- **Increased permeability:** Increased flow out of the vascular system caused by an increase in the permeability of the pulmonary capillaries, often due to damage to the capillary bed from inhaled or circulating toxins. This condition leads to adult respiratory distress syndrome (ARDS).

Current methods for measuring lung water are limited to accuracies and sensitivities of approximately 25 percent, which suffices for measurements of gross PE but cannot be used for the early detection of interstitial edema (Staub, 1980). EIT is potentially able to detect changes in the level of PE with a higher sensitivity. Unfortunately, very little work has been done to evaluate the effectiveness of this application of EIT.

Vahid-Shahidi et al. (1993) uses a 3D finite element model of the thorax to simulate the detectability of localised pulmonary edema (PE) using EIT with random noise added to the measurements. Images are reconstructed using the backprojection technique (Barber, 1985). They conclude that changes of conductivity due to PE are detectable under achievable conditions of measurement noise. Unfortunately, this study only simulates random electronic measurement noise and does not take into account the various physiological sources of error that occur.

Newell et al., (1993, 1995) describe an experiment to verify the assessment of PE in dogs by EIT. A pseudo-static EIT reconstruction algorithm (Cheney, 1990) is used to calculate the complex conductivity distribution in the animal. Experimental animals were anaesthetised and ventilated, and, after a stabilisation period, PE was induced by the infusion of oleic acid, resulting in a steady increase in lung conductivity until death, 240 to 300 min later. The lungs were subsequently extracted and the ratio of wet to dry content was calculated. In the five animals which received oleic acid, lung conductivity rose steadily by 4 to 10 percent above its initial value, whereas in one animal which received only saline injection, conductivity increased by 1 percent. Figure 2.8 plots the change in conductivity as a function of wet/dry weight ratio; the Pearson correlation coefficient is 0.83. Results indicate the presence of a change in the conductivity when pulmonary edema is forming and an absence of this change when it is not.
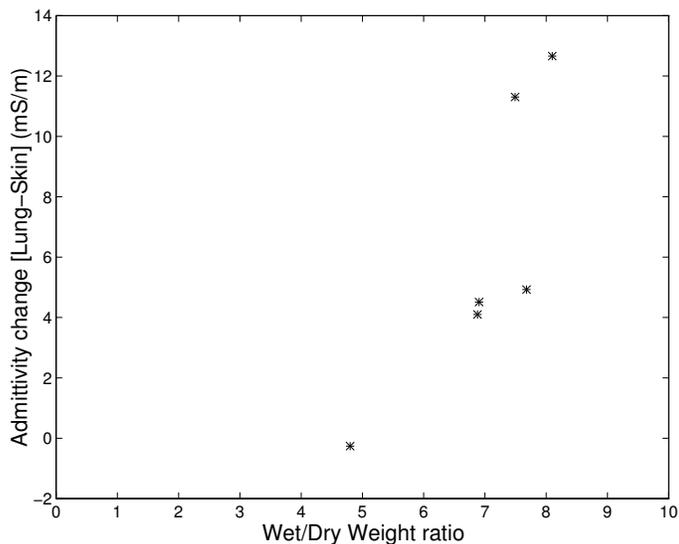
Figure 2.8: From Newell (1995): Changes in admittivity in the infused lungs plotted as a function of the wet/dry weight observed at the end of the experiment.

2.6   Conclusions

EIT as a medical imaging technique has matured significantly in the last decade. The problems initially considered were more concerned with engineering feasibility than clinical applicability. The first image reconstruction algorithms dealt with data measured from a cylindrical homogeneous phantom, and experimental data was measured from individual subjects and was presented without comparison to clinical reference standards. Recently, as the engineering feasibility of EIT has been demonstrated, there has been an increasing tendency to consider problems more relevant to the clinical application of the technique: image reconstruction techniques which use finite element models to simulate arbitrary medium geometries and take into account noise in the experimental data have been proposed; interpretation of EIT images reconstructed from data perturbed by various experimental difficulties such as electrode movement and anisotropy, has been considered; and, additionally, many groups have experimentally and clinically evaluated EIT.

In this spirit of undertaking work of clinical relevance, this thesis presents a, hopefully useful, contribution to EIT research.

CHAPTER 3:
A NEURAL NETWORK IMAGE
RECONSTRUCTION TECHNIQUE FOR
ELECTRICAL IMPEDANCE TOMOGRAPHY.

Authors:

Andy ADLER
Robert GUARDO

Published in:

Journal Reference:

Acknowledgements

3.1   Abstract

Reconstruction of Images in Electrical Impedance Tomography requires the solution of a non-linear inverse problem on noisy data. This problem is typically ill-conditioned and requires either simplifying assumptions or regularization based on a priori knowledge. This paper presents a reconstruction algorithm using neural network techniques which calculates a linear approximation of inverse problem directly from finite element simulations of the forward problem. This inverse is adapted to the geometry of the medium and the signal to noise ratio (SNR) used during network training. Results show good conductivity reconstruction where measurement SNR is similar to the training conditions. The advantages of this method is its conceptual simplicity and ease of implementation, and the ability to control the compromise between the noise performance and resolution of the image reconstruction.

3.2   Introduction

We consider the problem of dynamic imaging in Electrical Impedance Tomography (EIT), which involves estimating conductivity changes in a medium from electrical measurements on the medium boundary. Our tomographic system uses 16 injection/measurement electrodes, where a set of electrical measurements is made by differential voltage measurements at all adjacent pairs of electrodes for each of the 16 patterns of current injection. In order to reconstruct the conductivity changes during the interval t_2 - t_1 , two complete sets of measurements, one at t_1, and the other at t_2, are required.

By restricting our interest to the conductivity changes rather than absolute conductivity values (as in static imaging), we gain three principal advantages:

- due to variations in electrode contact resistance and positioning, and electronic hardware dependence on temperature, it is difficult to obtain sufficiently accurate measurements for static imaging. These variables tend to remain constant, however, allowing compensation for the inaccuracies produced by looking only at the changes in measurements.

- static image reconstruction is highly non-linear, and requires accurate knowledge of the electrode positioning and medium geometry. The dynamic imaging problem is much more linear, and, as we show in section VI, relatively insensitive to geometrical errors.

- Dynamic imaging has higher sensitivity to conductivity changes than static imaging, because it rejects the components of the signal and the noise which are common to the measurements. These changes in measurements produced by typical physiological phenomena rarely exceed 10 percent of the total measurements, thus allowing dynamic imaging to achieve a sensitivity improvement of 20 dB.

The techniques that are currently used for dynamic image reconstruction may be classified into linear and non-linear algorithms. Many linear algorithms for dynamic image reconstruction have been proposed including Equipotential Backprojection (Barber, 1986), (Guardo, 1991) and more recently, sensitivity matrix methods (Barber,

1988), and regularization methods (Hua, 1988), (Woo, 1993). The principal non-linear algorithm used is the modified Newton-Raphson method (Yorkey, 1987), (Adler, 1993), which requires several orders of magnitude more calculation time than linear techniques. All of these techniques, while giving reasonable solutions, require simplifying hypotheses about the problem. In this paper we propose a new technique based on neural networks, which has the advantage of a simple mathematical formulation not requiring any of these assumptions.

3.3   Forward Problem
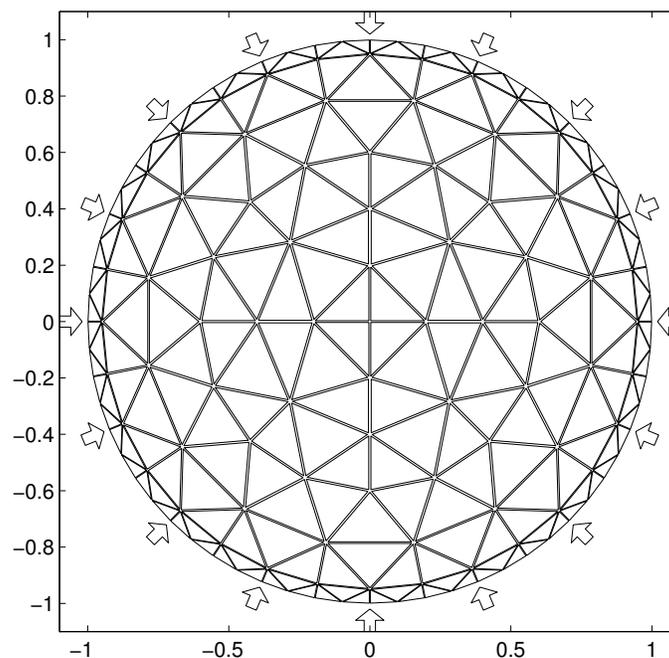
Figure 3.1: Finite element model and electrode placements.

In a very vulgar sense, the neural network training process may be described as presenting a series of problems and their solutions to the network until it "figures out" the problem-solving technique. To do this training, we therefore need a training set, consisting of voltage measurements (problems), and the conductivity distributions which produced them (solutions). Originally we produced this training set experimentally (Guardo, 1991), but found this method overly time consuming to obtain the necessary size of training set. In this paper we use a finite element model (FEM) of the medium to numerically simulate our training set.

The FEM used, figure 3.1, is a two dimensional model based on triangular elements. The interior has 120 elements in which the conductivity is allowed to vary, and the boundary is divided into 96 much smaller elements restricted to one conductivity value; the electrodes placements are marked by arrows. We do not use a three dimensional model because, due to the fact that we are considering the dynamic problem, the measurement sensitivity to conductivity changes in the electrode plane in a 3D model is almost identical to the sensitivity in the 2D model. The conductivity pattern of the medium is represented by the vector $\mathbf{r}$ representing a parametrization of the element conductivities. Our model has n=121 degrees of freedom. After setting one node to a reference potential, one can solve for $\mathbf{V}_{ij}$, the voltage at node i during current injection pattern j, by

$$\mathbf{V} = \mathbf{Y}(\sigma)^{-1}\mathbf{C} \tag{3.1}$$

where $\mathbf{Y}$ is the admittance matrix (a function of the tissue conductivity), and each element of $\mathbf{C}_{ij}$ represents the current injected into node i during the excitation pattern j. Calculation of the vector of differential measurements, $\mathbf{v}$, from $\mathbf{V}$ is represented by $\mathbf{v} = T(\mathbf{V}(\mathbf{r}))$. This operator selects and subtracts the voltages at the nodes corresponding to electrode pairs in the physical situation to be modelled.

Since we are looking for a linear solution, it is important to choose a good parametrization of the conductivity to maximise the solution linearity. Expressing the solution in terms of the conductivity σ is a poor choice, because negative values of σ do not represent possible conductivities in the medium, and we would therefore be forced to restrict the neural network to producing only positive solutions. We express the problem in terms of the log conductivity, which corresponds to a possible conductivity for all real values. The change in measurements caused by an inhomogeneity (in an otherwise homogeneous medium of conductivity σ) is a linear function of the size of the perturbation to within 10% in the range $.25 < \sigma < 4$ as long as the perturbation stays at least 10% of the radius away from the boundary. For perturbations outside of this range, the change in measurements saturates. The effect of this saturation in the inverse problem is to cause an underestimation of the conductivity changes.

The dynamic measurement vector, $\mathbf{f}$, (also referred to in this paper as the signal) is defined as the ratio of the measurements before and after the conductivity change

$$\mathbf{f}_i = \frac{\mathbf{v}_i^{after} - \mathbf{v}_i^{before}}{\mathbf{v}_i^{after} + \mathbf{v}_i^{before}} = \frac{T(\mathbf{V}(\mathbf{r}_a) - \mathbf{V}(\mathbf{r}_b))_i}{T(\mathbf{V}(\mathbf{r}_a) + \mathbf{V}(\mathbf{r}_b))_i}, \quad \text{for } 1 \le i \le N$$

(3.2)

where N is the total number of measurements, and $\mathbf{r}_b$ and $\mathbf{r}_a$ represent the conductivities before and after, respectively. Because the changes are small compared to the measurements themselves, the divisor in this expression can be estimated by the $\mathbf{v}$ calculated for a homogeneous conductivity r_h, giving

$$\mathbf{f}_i \approx \frac{T(\mathbf{V}(\mathbf{r}_a) - \mathbf{V}(\mathbf{r}_b))_i}{T(\mathbf{V}(r_h) + \mathbf{V}(r_h))_i} \approx \frac{T(\mathbf{V}(\mathbf{r}_a - r_h) - \mathbf{V}(\mathbf{r}_b - r_h))_i}{2T(\mathbf{V}(0))_i}$$

$$\approx \frac{T(\mathbf{V}(\mathbf{r}_a - \mathbf{r}_b))_i}{2T(\mathbf{V}(0))_i} - \frac{1}{2}$$

(3.3)

The r_h can be factored out of this equation because V is inversely proportional to an increase everywhere in conductivity.

Linearizing about $\mathbf{r} = \dfrac{\mathbf{r}_a - \mathbf{r}_b}{2}$ gives $\mathbf{f} = \mathbf{Sr}$, where

$$\mathbf{S}_{ij} = \frac{1}{T(\mathbf{V}(0))_i} \frac{\partial}{\partial \mathbf{r}_j} T(\mathbf{V}(\mathbf{r}))_i \bigg|_{\mathbf{r}=0}$$

(3.4)

The matrix $\mathbf{S}_{104 \times 121}$ is the sensitivity matrix for the FEM, containing, in each column i the change in signal produced by a small perturbation in element j of the medium. These vectors are subsequently used as training vectors for the neural network. The calculation of the partial derivative is calculated using the expression

$$\frac{\partial}{\partial \mathbf{r}_i} T(\mathbf{V}(\mathbf{r}))_i = -T\left(\mathbf{Y}^{-1}(\mathbf{r}) \frac{\partial}{\partial \mathbf{r}_i} \mathbf{Y}(\mathbf{r}) \mathbf{Y}^{-1}(\mathbf{r}) \mathbf{C}\right)_i$$

(3.5)

3.4   Inverse Problem

The inverse problem may be stated as finding the matrix $\mathbf{Z}$, which, in the presence of noise n, best approximates, in the least squared error sense,

$$\mathbf{r} \approx \mathbf{Z}(\mathbf{f} + n)$$

(3.6)

for all signals **f**. This **Z** is calculated by the training processes of the neural network, and subsequently is used as the reconstruction operator to estimate the conductivity changes **r** from the voltages measurements.
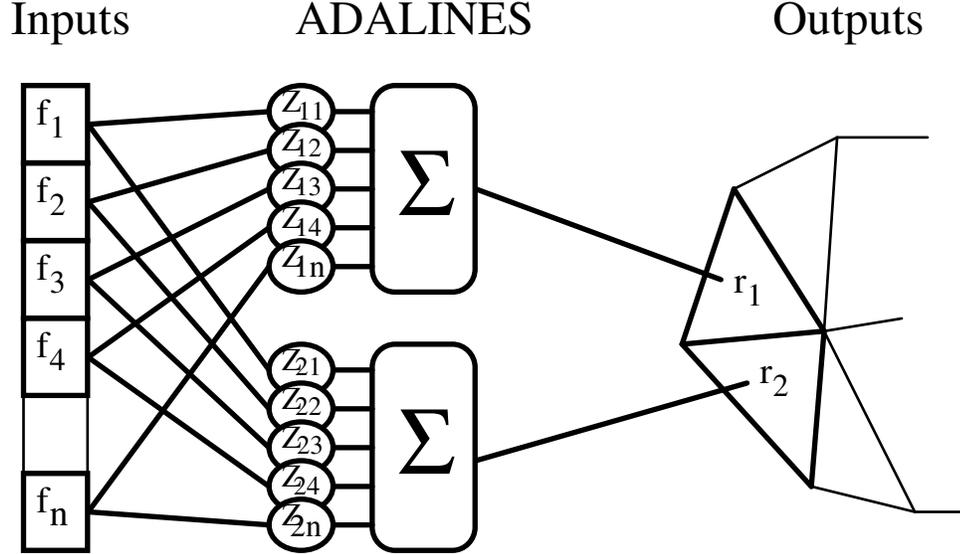
Figure 3.2: Neural Network configuration using ADALINEs.

The neural network model used here is the Adaptive Linear Element, or ADALINE (Rogers, 1991), (Widrow, 1990), as shown in figure 3.2. Each ADALINE calculates the value of one conductivity element of **r** by summing the inputs weighted by the elements of the corresponding column of **Z**. The output of ADALINE i is thus $\sum z_{ij} f_i$ summed over $1 \leq j \leq N$. The values of **Z** are calculated or "trained" by the Widrow-Hoff learning rule, using a set of input vectors $\mathbf{f}_k$ and their (known) desired responses from the network $\mathbf{d}_k$. Training aims to minimise the error, f, for all training sets k:

$$\phi = \sum_k (\mathbf{d}_k - \mathbf{Z}\mathbf{f}_k)^t (\mathbf{d}_k - \mathbf{Z}\mathbf{f}_k)$$

(3.7)

We choose the desired responses to be individual conductivity changes in each element, i.e. $[\mathbf{d}_1 \mathbf{d}_{2} ... \mathbf{d}_n] = \mathbf{I}$, for which the input vectors are $[\mathbf{f}_1 \mathbf{f}_{2} ... \mathbf{f}_n] = \mathbf{YI} = \mathbf{I}$. In order to train the network to deal with noise, we must include the expected noise, n, in the input. Using this training set, we carry out the following algorithm:

- Initially, set all weights, **Z**, to small random numbers.

- Choose a random order of presentation of the input vectors to the network.

- Begin training iterations: (Z_i represents the weights at iteration i)

- Present a training vector plus random noise to the network, outputting:

$$\mathbf{o} = \mathbf{Z}_i(\mathbf{f} + n)$$

(3.8)

- Calculate the error $\mathbf{e} = \mathbf{o}$ - $\mathbf{d}$, defined as the difference between the output, and the corresponding desired response.

- Update network weights by the learning rule:

$$\mathbf{Z}_{i+1} = \mathbf{Z}_i - \alpha\mathbf{eo}^t$$

(3.9)

- Continue iteration until the rms error $\sqrt{\mathbf{e}^t\mathbf{e}}$ is below an acceptable limit.

The parameter α controls the learning rate; for stability, it's value must be less than the reciprocal of the maximum eigenvalue of $\mathbf{YY}^t$ (Widrow, 1985).

Once the training is completed, $\mathbf{Z}$ can be used as a reconstruction operator which calculates the change in conductivity distribution during the interval t_2 - t_1, from the measured voltage vectors $\mathbf{v}_1$ and $\mathbf{v}_2$. First, the reconstructed element conductivities are calculated, using:

$$\mathbf{r}_{reconst} = \mathbf{Z}\left(\frac{\mathbf{v}_2 - \mathbf{v}_1}{\mathbf{v}_2 + \mathbf{v}_1}\right)$$

(3.10)

and then the element conductivies are interpolated onto a rectangular co-ordinate frame, which can be displayed using various graphics rendering techniques. Once the neural network has been trained, the image reconstruction process is extremely rapid, requiring only a matrix multiplication.

3.5   Ill-Conditioning of the Inverse Problem

It may seem natural to ask why we are using a neural network approach to solve a linear problem rather than algebraic techniques. The answer lies in the ill-conditioning of the problem. In order to achieve an acceptably uniform spatial resolution, we divide the

medium into 120 conductivity elements, which must be estimated from 104 voltage measurements (the reciprocity theorem (Geselowitz, 1971) states that only half of the 256 measurements taken are linearly independent and, additionally, we reject the measurements made at electrodes used for injection). This implies that the problem is under-determined, and that we require some source of extra information about the problem in order to determine the conductivity distribution from the measurements. This under-determination is worsened by the poor conditioning of the sensitivity matrix, which can be seen from the fact that conductivity changes in the middle of the medium produce much less signal than changes near the boundary; for instance, at 75 percent radius, the signal is ten times greater than it is in the centre.

The ill-conditioning and under-determination imply that any matrix inverse will require regularization, the quantity and form of which must be determined from the mathematical formulation and the experimental situation. Using the neural network approach, we are able to perform an inverse directly from the FEM and the estimated signal to noise ratio, without any additional assumptions or analysis.

The neural network training is affected by this ill-conditioning in various ways. The network initially "learns" to respond to training patterns near the boundary of the medium, and only begins to respond to training patterns near the centre once the performance on the boundary is nearly optimal. Additionally, the under-determination implies that the best possible spatial resolution is inferior to the size of the training patterns. Therefore, the network can never reproduce the training patterns exactly, and the error will never approach zero, but will only drop to a fraction of the initial error. This behaviour is discussed in section 3.6.

We define the signal to noise ratio (SNR) of the measurements as

$$\text{SNR}_{meas} = \frac{\mathbf{f}^t \mathbf{f}}{\mathbf{n}^t \mathbf{n}}$$

(3.11)

In the case of the training SNR, where there are many different training signals, $\mathbf{f}$ is defined as the signal produced by a unit conductivity change in an element in the centre. The SNR of the image is defined as the expected value

$$\text{SNR}_{image} = E\left[\frac{(\mathbf{AZf}_o)^t(\mathbf{AZf}_o)}{(\mathbf{AZn})^t(\mathbf{AZn})}\right] = \frac{\mathbf{f}_o{}^t\mathbf{Z}^t\mathbf{A}^2\mathbf{Zf}_o}{\displaystyle\sum_{i=1}^{m}\mathbf{n}_i{}^2\left(\mathbf{Z}_i{}^t\mathbf{A}^2\mathbf{Z}\right)}$$

(3.12)

where n_i is the rms noise value for measurement i, $\mathbf{Z}_i$ is the ith column of $\mathbf{Z}$, and $\mathbf{A}$ is a diagonal matrix of the areas of the elements (a_{ii} is the area of element i). The signal $\mathbf{f}_o$ is produced by a conductivity change in the centre with amplitude such that the measurement SNR equals one. The expected value can be expressed as a sum in the denominator because the elements of $\mathbf{n}$ are statistically independent.

The resolution of the image is a function of the radial position. We define the resolution of the reconstructed image at a given position as the square root of the area percentage occupied by 50% of the reconstructed image mass from a point conductivity change at that position. Thus, the image resolution is

$$\mathbf{r}_{image} = \sqrt{\frac{\mathbf{x}^t\mathbf{Ax}}{\mathbf{1}^t\mathbf{A1}}}$$

(3.13)

where $\mathbf{1}$ is a column vector of ones, and $\mathbf{x}$ is one in the elements closest to the image maximum accounting for 50% of the image mass, and zero elsewhere. Thus $\mathbf{x}$ must satisfy

$$\frac{\mathbf{x}^t\mathbf{r}}{\mathbf{1}^t\mathbf{r}} = \frac{1}{2}$$
.

(3.14)

The square root in equation 3.13 is used to express the resolution in terms of the diameter rather than the area.

In order to compare the neural network results with equipotential backprojection, we have calculated a matrix $\mathbf{Z}_{\text{backprojection}}$ which maps the backprojected image onto our FEM, allowing us to use the equivalent evaluation process on both techniques.

3.6   Results from Simulations

Neural networks N_0, N_1, and N_2 were trained using 1500 iterations on the circular finite element geometry of figure 3.1. N_0 was trained without adding any

expected noise to the training vectors, while N_1 and N_2 had SNRs of 5 dB and -10 dB respectively. The rms training error vs. iteration number is shown in figure 3.3.
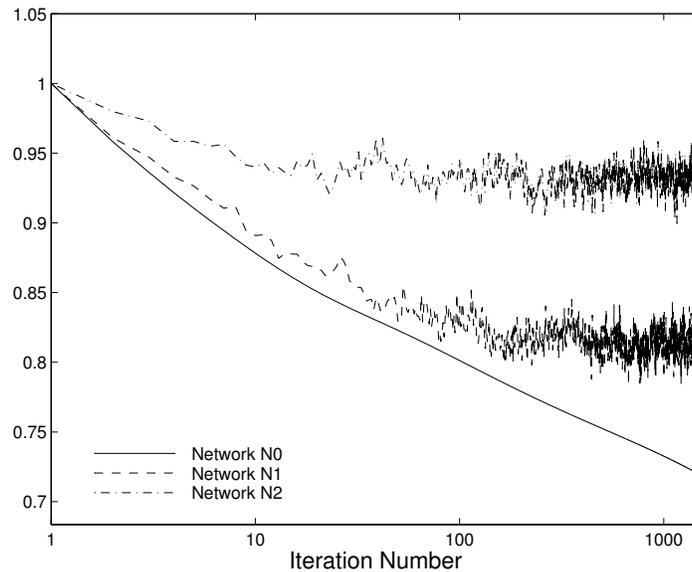
Figure 3.3: Training Error vs Iteration for Neural Networks

The performance of this reconstruction technique compared to equipotential backprojection on simulated data is shown in figure 3.4. Figure 3.4A shows the pattern to be imaged: two small non-conductive objects in a circular medium separated by one third of the diameter. This pattern was simulated on a much finer finite element mesh than was used for the training of the neural networks. Figures 3.4B, D, and F were reconstructed using the voltage measurements from 3.4A with no noise added, while figures C, E, and G used measurements with SNR of -5 dB. Reconstruction in B and C used weighted backprojection, D and E used network N_2, and F and G used network N_0.

The network N_0 has better spatial resolution at the expense of reduced ability to reject noise. Conversely, the N_2 has significantly improved noise performance (roughly equal to that of backprojection) with a reduction in spatial resolution. The spatial resolution of N_2 is better than that of backprojection, especially near the medium centre.
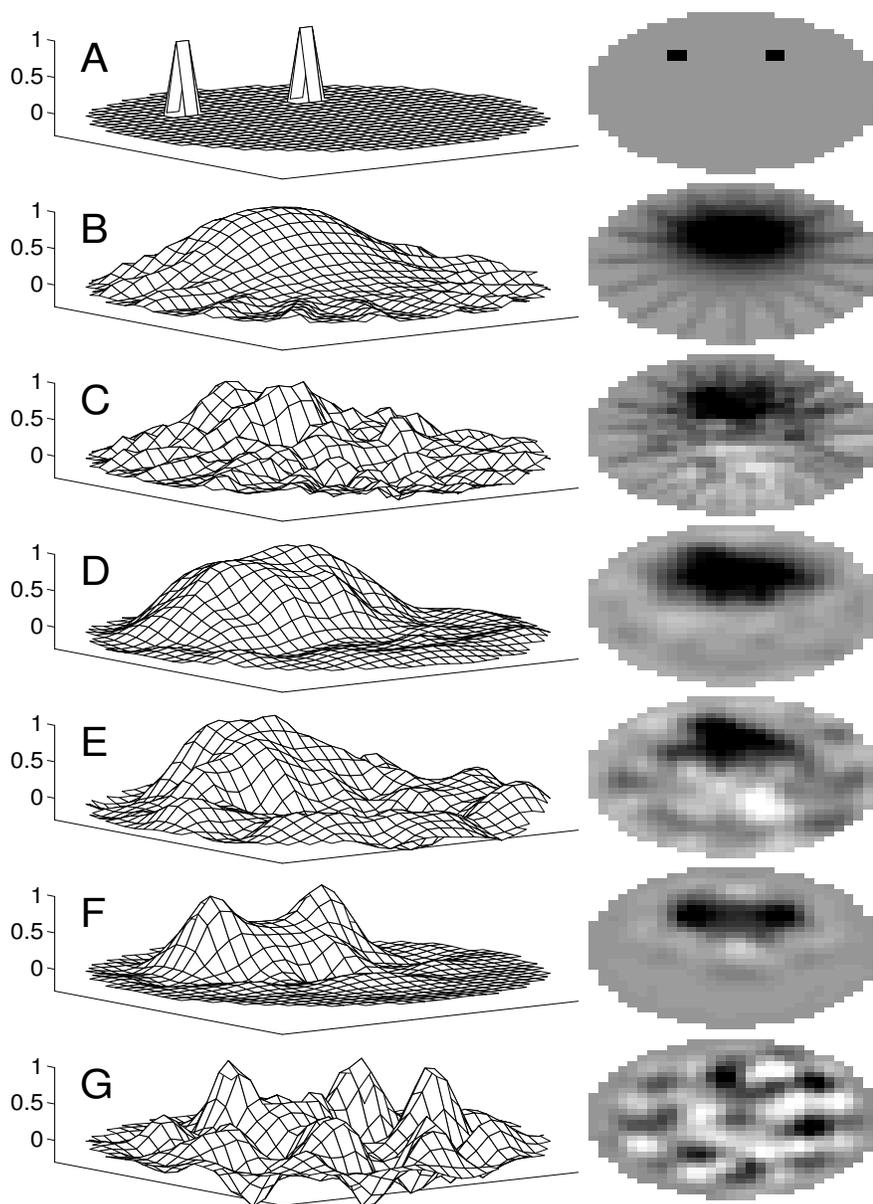
Figure 3.4: Reconstructed Images

A: Generating conductivity pattern
B: Image: *No Noise*   Backprojection
C: Image: *-5 dB SNR*   Backprojection
D: Image: *No Noise*   Network: *-10dB SNR*
E: Image: *-5 dB SNR*   Network: *-10dB SNR*
F: Image: *No Noise*   Network: *No Noise*
G: Image: *-5 dB SNR*   Network: *No Noise*

Table 3.1: Training SNR and Image SNR for various algorithms.

Algorithm	Training SNR	Image SNR
Backprojection		2.62
Network N_0	$\propto$	0.22
Network N_1	1.33	0.69
Network N_2	0.33	1.58
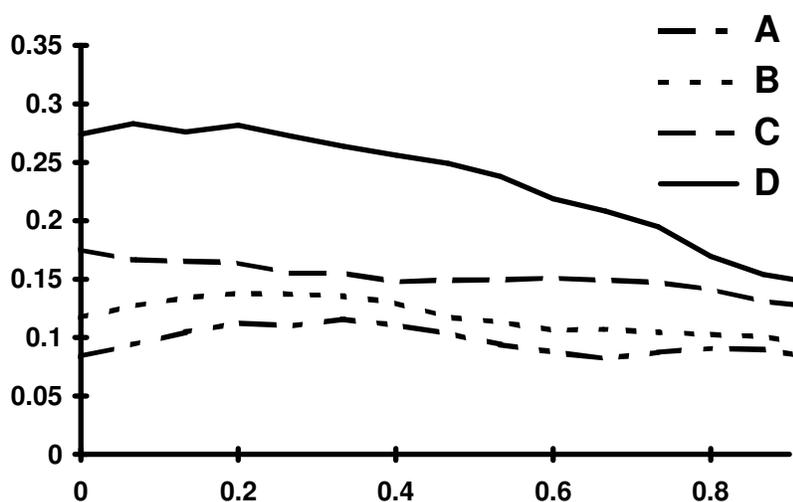
Figure 3.5: Spatial resolution vs. radial position
        A: Network N_0
        B: Network N_1
        C: Network N_2
        D: Backprojection

       The noise performance of the various networks, as measured by the image SNR, is compared with that of backprojection in table 3.1. As the SNR during the training is reduced, the network is able to better deal with noise, and the image SNR, for a given measurement noise, improves. Figure 3.5 shows the spatial resolution as a function of radial position for backprojection, and networks N_0, N_1, and N_2. The radial position of 0 represents the centre and 1 represents the medium boundary.

3.7 Geometrical Errors
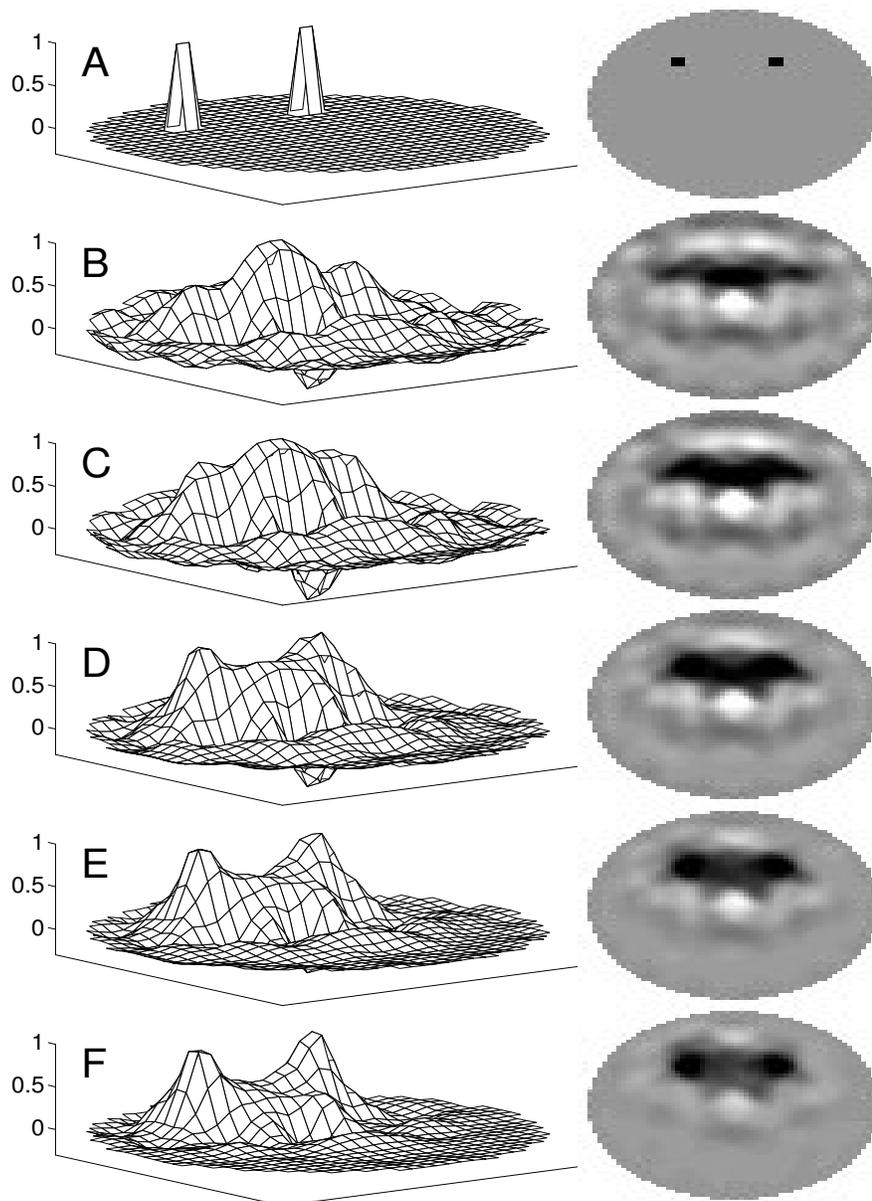
Figure 3.6: Reconstruction Errors due to elliptical deformation
A: Generating conductivity pattern
B: Deformation: height/width = 2.0
C: Deformation: height/width = 1.5
D: Deformation: height/width = 1.2
E: Deformation: height/width = 1.1
F: No Deformation: height = width

One possible problem with the neural network approach is its specificity to the geometry and measurement configuration used during the training phase, meaning that any measurements made on a medium with a different geometry than the one used during training would introduce errors into the reconstructed image. In order to test the severity of this problem, measurements were calculated from media deformed into ellipses of various height/width ratios, and the images were reconstructed using the neural network, N_0, trained on a circular medium; these images are shown in figure 3.6. The reconstruction error for each image is presented in table 3.2; it is defined as

$$\varepsilon_{reconst} = \sqrt{\frac{(\mathbf{r}_c - \mathbf{Zf})^t (\mathbf{r}_c - \mathbf{Zf})}{\mathbf{r}_c^t \mathbf{r}_c}}$$

(3.15)

where $\mathbf{r}_c$ is the generating conductivity pattern, and $\mathbf{f}$ is measured from the deformed medium.

Table 3.2: reconstruction error due to geometrical errors

Training height/width	Measurement height/width	Reconstruction error	Figure
1.0	2.0	1.48	3.6B
1.0	1.5	0.94	3.6C
1.0	1.2	0.64	3.6D
1.0	1.1	0.55	3.6E
1.0	1.0	0.49	3.6F

Geometrical errors, as long as they are small (<20%) seem to only introduce small errors (<30%) into the reconstructed images. This insensitivity is a property of the dynamic imaging method. Because of this property, we may use the neural networks trained on a circular geometry to image conductivity changes in the thorax, as shown in section 3.7.

3.8   Results from Measured Data

The reconstruction technique presented here is capable of giving acceptable results using data measured from our EIT system. Figure 3.7 shows images of two non-conductive objects in a saline solution inside a cylindrical frame: one object is 2/3 of the

radius toward the front and the other is 1/3 of the radius toward the right. Figure 3.7A is reconstructed using network N_2 while 3.7B uses backprojection. Figure 3.8 is an image of the conductivity change between expiration and inspiration in the thorax region of one of the authors (Adler). Data acquisition was gated on the QRS signal while the patient held his breath, thus the only conductivity change is due to change in lung air volume. Figure 3.8A is reconstructed using network N_2 while figure 3.8B uses backprojection. In these figures, the darker areas represent areas of decreased conductivity.
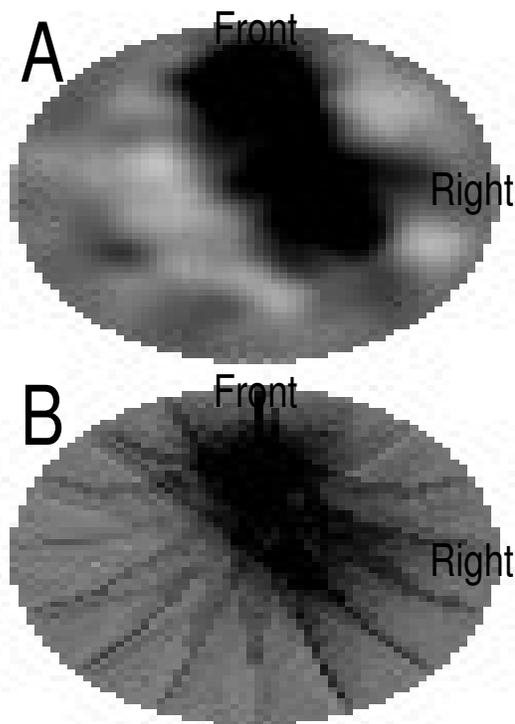
Figure 3.7: Images of two non conductive objects in saline solution
A: Image using neural networks
B: Image using backprojection

In the case of figure 3.7, the neural network technique appears to produce clearly superior images, both in terms of resolution and noise. In figure 3.8 it is possible to distinguish two regions of decreased conductivity in approximately the region of the lungs with both imaging techniques; however, the neural network is able to give a higher resolution image, and without the streak-like artefacts of the backprojection. As data from our tomographic system tends to be quite noisy, typically 0 to 20 dB SNR, it was

necessary to use the network trained with the highest noise level, and consequently lowest image resolution.
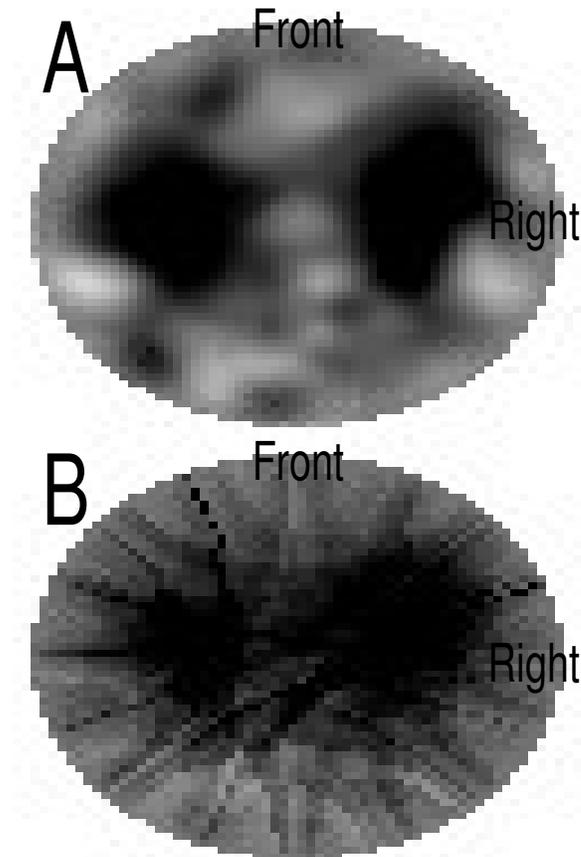
Figure 3.8: Image of conductivity changes (inspiration - expiration) in the author's thorax
        A: Image using neural networks
        B: Image using backprojection

3.9   Discussion

In this paper we have presented a neural network algorithm which trains a linear reconstruction operator to calculate the conductivity changes from the electrical measurements on a medium boundary. This operator is determined uniquely from a finite element solution of the forward problem and a knowledge of SNR expected in the real data. When trained without noise, the reconstruction has excellent resolution but poor ability to reject noise. Conversely, when trained with a large SNR, the reconstruction has

a much better noise performance, comparable to that of equipotential backprojection, and a resolution which, while poorer, is still better than that of backprojection. The advantages of this method are it's speed of image reconstruction, it's conceptual simplicity and ease of implementation, and the control of the compromise between the image resolution and image SNR. A possible disadvantage is the long calculation time required to train the neural network.

Even though able to produce good solutions in comparison to other techniques, the neural network algorithm presented here is unable to deal with the non-linear aspects of the problem, such as the saturation of measurements produced by large conductivity changes, or the effect of the interaction between multiple regions of conductivity changes. It would be feasible to expand the neural network formulation to treat the non-linearities by the addition of hidden layers into the neural network formulation. In order to allow the network to adapt to the much more complex non-linear nature of the problem, a much more complete training set would be required, including multiple element conductivity patterns of varied amplitudes. Such an approach would be interesting in that it would provide a much faster non-linear reconstruction technique than the iterative methods presently used.

CHAPTER 4:
ELECTRICAL IMPEDANCE TOMOGRAPHY:
REGULARIZED IMAGING AND CONTRAST DETECTION

Authors:

Andy ADLER
Robert GUARDO

4.1   Abstract

Dynamic electrical impedance tomography images changes in the conductivity distribution of a medium from low frequency electrical measurements made at electrodes on the medium surface. Reconstruction of the conductivity distribution is an under-determined and ill-posed problem, typically requiring either simplifying assumptions or regularization based on a priori knowledge. This paper presents a maximum a posteriori (MAP) approach to linearized image reconstruction using knowledge of the noise variance of the measurements and the covariance of the conductivity distribution. This approach has the advantage of an intuitive interpretation of the algorithm parameters as well as fast (near real time) image reconstruction. In order to compare this approach to existing algorithms, we develop figures of merit to measure the reconstructed image resolution, the noise amplification of the image reconstruction, and the fidelity of positioning in the image. Finally, we develop a communications systems approach to calculate the probability of detection of a conductivity contrast in the reconstructed image as a function of the measurement noise and the reconstruction algorithm used.

4.2   Introduction

Electrical Impedance Tomography (EIT) is a medical imaging technique which calculates the electrical conductivity distribution within a medium using electrical measurements from a series of electrodes on the medium surface. A low amplitude alternating current is successively injected across pairs of electrodes while the voltage differences produced on the remaining electrodes are measured. The conductivity distribution is then estimated using this measured data. We are particularly interested in dynamic EIT (the measurement of conductivity changes) because of its increased sensitivity and ability to compensate for measurement unknowns.

Dynamic EIT is of interest in studying physiological processes which modify the electrical conductivity of the body. For instance, cardiac, respiratory, and gastric activity modify the conductivity distribution by the movement of liquids or gasses and can be imaged using EIT. Several reconstruction techniques have been proposed for dynamic EIT, most of which use a linear reconstruction technique, although an iterative model has also been used, and are based either on a finite element or analytic models of the forward problem.

In this paper we present a new algorithm based on regularization of the linearized forward problem, using *a priori* knowledge of the distribution of conductivity change. This algorithm allows a control of the compromise between the noise performance and the resolution in the reconstructed image, based on knowledge of the measurement noise in the hardware and the magnitude of the conductivity changes to be detected. Because the algorithm is linear, the reconstruction process requires only a single matrix multiplication, and is several orders of magnitude faster than iterative techniques which require several matrix inversions. We also develop several figures of merit with which to compare our technique to other proposed algorithms.

Many proposed applications of EIT are concerned primarily with the detection of conductivity changes in a region of interest, and the image produced is used primarily as a means of rejecting contributions from activity in other areas. In order to determine the limits of detectability of image contrasts, we develop a model of the probability of detection of a contrast as a function of the noise variance and the image reconstruction algorithm used.

The first proposed EIT reconstruction algorithm (Barber, 1987), equipotential backprojection, performed dynamic imaging. This technique reconstructs images by projecting the change in measurements at each electrode pair across the equipotential region for that current injection pattern, multiplied by an image filter. This equipotential region is the area in a homogeneous medium in which the potential is between that of the adjacent measurement electrodes; it is the fraction of the medium which most affects the corresponding measurement. Backprojection produces reasonably good quality images with good performance under noise. However, unlike the x-rays used in CAT scanning, currents in EIT do not move in a line, but cover the region from the current source to drain. A bias is thus introduced into the image as the equipotential region is an approximation to the region producing the measurement change at each electrode. Another difficulty with backprojection is that, while it reconstructs an image pattern representing the conductivity change in the medium, it does not reconstruct the actual conductivity values. From a performance point of view, backprojection tends to "push" reconstructed object positions toward the centre of the medium, and to produce streak-like artefacts in the image.

An iterative reconstruction using the Newton-Raphson technique with Tikhonov regularization was originally proposed by Yorkey (1987) for static reconstruction of EIT. Most iterative regularized approaches also have been proposed for static EIT, although the technique has also been used for dynamic EIT (Adler 1993; Shaw, 1993; Woo, 1993). These approaches can be formulated as the minimisation of an error function, ϕ

$$\phi(\sigma) = \tfrac{1}{2}\left(\|\mathbf{z} - \mathbf{Z}(\sigma)\|_{\mathbf{W}}^2 + \mu\|\sigma\|_{\mathbf{Q}}^2\right)$$

(4.1)

where $\mathbf{z}$ is the measured signal, $\mathbf{Z}$ is a finite element model of the signal, and μ, $\mathbf{Q}$, and $\mathbf{W}$ are parameters of the reconstruction algorithm. The second term in equation 4.1 is a regularization term, the quantity of which is controlled by the parameter μ. The reconstructed image is the conductivity distribution σ which minimises the error. The identity matrix is used for both $\mathbf{Q}$ and $\mathbf{W}$ by Yorkey (1987) and Adler (1993) while Shaw (1993) and Woo (1993) use a matrix $\mathbf{Q}$ based on $\mathbf{Z}$. Selection of μ in these algorithms is done by the user, based on qualitative considerations.

4.3   Dynamic Imaging

In general, static reconstruction algorithms suffer from a high sensitivity to measurement errors (Barber, 1988), due to EIT being more sensitive to changes near the medium surface than to changes within the medium. Thus a slight error in the positioning of an electrode will have as much effect on the voltage measurements as a large inhomogeneity in the centre of the medium. The effect of these errors can be reduced by considering dynamic imaging, which takes measurement sets $\mathbf{v}^1$ at time t^1, and $\mathbf{v}^2$ at t^2, from which the change in conductivity distribution in the interval (t^1, t^2) is calculated (imaged).   While considering only changes in measurements results in a loss of information, most proposed applications of EIT are concerned with the conductivity change rather than its absolute value (Barber, 1986).

Dynamic Imaging offers many advantages in simplicity and robustness. The simplest EIT measurement configuration uses EKG type electrodes placed directly on the patient's skin. Many unknowns are introduced into the measurement process at this stage due to variability in the initial positioning of the electrodes, patient posture, electrode contact resistance with the skin and the gain of the acquisition electronics. Dynamic imaging is able to deal with this variability by assuming that these variables remain constant over time. If we model the effect of these unknowns on the EIT measurements by introducing random constants a_i and b_i for each pattern of current injection and voltage measurement, then the measurement set may be expressed by:

$$\mathbf{v}_i = a_i \mathbf{u}_i + b_i$$

(4.2)

where $\mathbf{u}_i$ is the theoretical measurement value, $\mathbf{v}_i$ is the actual measurement, and i is an index over all the measurements.

We define the dynamic signal, $\mathbf{z}$, for the time interval (t^1, t^2) as

$$\mathbf{z}_i = \frac{\mathbf{v}_i^{1} - \mathbf{v}_i^{2}}{\frac{1}{2}\left(\mathbf{v}_i^{1} + \mathbf{v}_i^{2}\right)}$$

(4.3)

which in terms of $\mathbf{u}$ is

$$\mathbf{z}_i = \frac{\mathbf{u}_i^{\ 1} - \mathbf{u}_i^{\ 2}}{\frac{1}{2}\left(\mathbf{u}_i^{\ 1} + \mathbf{u}_i^{\ 2} + 2\frac{b_i}{a_i}\right)} = \frac{\mathbf{u}_i^{\ 1} - \mathbf{u}_i^{\ 2}}{\frac{1}{2}\left(\mathbf{u}_i^{\ 1} + \mathbf{u}_i^{\ 2}\right)}\left(\frac{1}{1 + \dfrac{2b_i}{a_i\left(\mathbf{u}_i^{\ 1} + \mathbf{u}_i^{\ 2}\right)}}\right)$$

(4.4)

This implies that dynamic imaging removes the effect of any multiplicative unknowns in the data (a_i's) for small b_i, and reduces the effect of the additive unknowns (b_i's) by a factor of $\frac{1}{2}a_i\left(\mathbf{u}_i^{\ 1} + \mathbf{u}_i^{\ 2}\right)$. This greater immunity to variability in the measured data accounts for the robustness of dynamic EIT.

4.4   Linearization of the Forward Problem

Using the finite element method (FEM), we simulate the voltage distribution at E electrodes by current injection into a medium with a conductivity distribution discretized on N finite elements. This model of the forward problem accepts a $N \times 1$ vector $\boldsymbol{\sigma}$ of element conductivity values and calculates the voltage $\mathbf{V}_{ij}$ at each electrode i for each current injection pattern j

$$\mathbf{V} = \mathbf{Y}(\ )^{-1}\mathbf{C}$$

(4.5)

where $\mathbf{Y}$ is the admittance matrix of the FEM (and is a function of the conductivity distribution) and $\mathbf{C}_{ij}$ represents the current injected into electrode i during current injection pattern j. It is necessary to fix the voltage at one node to a constant potential in order for $\mathbf{Y}$ to be invertible. Our EIT system makes differential voltage measurements between adjacent electrodes at all electrodes not used for current injection, giving $M = E \times (E\text{-}3)$ measurements. All measurements are used in the image reconstruction, even though, due to reciprocity (Geselowitz, 1971), only half of these measurements are linearly independent. Calculation of the vector $\mathbf{v}$ of M voltage differences is represented by $\mathbf{v} = T[\mathbf{V}(\ )]$. For instance, if $\mathbf{v}_9$ is defined to correspond to the voltage difference between electrodes 4 and 5 during injection pattern 2, then the operator T will give $T[\mathbf{V}]_9 = \mathbf{V}_{42} - \mathbf{V}_{52}$. The dynamic signal $\mathbf{z}$ is defined as

$$\mathbf{z}_i = \frac{\mathbf{v}_i^{\ 1} - \mathbf{v}_i^{\ 2}}{\frac{1}{2}\left(\mathbf{v}_i^{\ 1} + \mathbf{v}_i^{\ 2}\right)} = \frac{T\left[\mathbf{V}\left(\sigma^1\right) - \mathbf{V}\left(\sigma^2\right)\right]_i}{\frac{1}{2}T\left[\mathbf{V}\left(\sigma^1\right) + \mathbf{V}\left(\sigma^2\right)\right]_i}$$

(4.6)

for each measurement i, $1 \leq i \leq M$, where $\boldsymbol{\sigma}^1$ and $\boldsymbol{\sigma}^2$ represent the conductivities at times t^1 and t^2, respectively.

Throughout this article we use a two dimensional finite element model because of the gain in calculation time by not considering several layers of finite elements. Although some amount of error is introduced into the simulated measurements by using a 2D model, the dynamic imaging process reduces this error as shown in section 4.3. Our simulations indicate that this error is reduced by approximately three orders of magnitude.
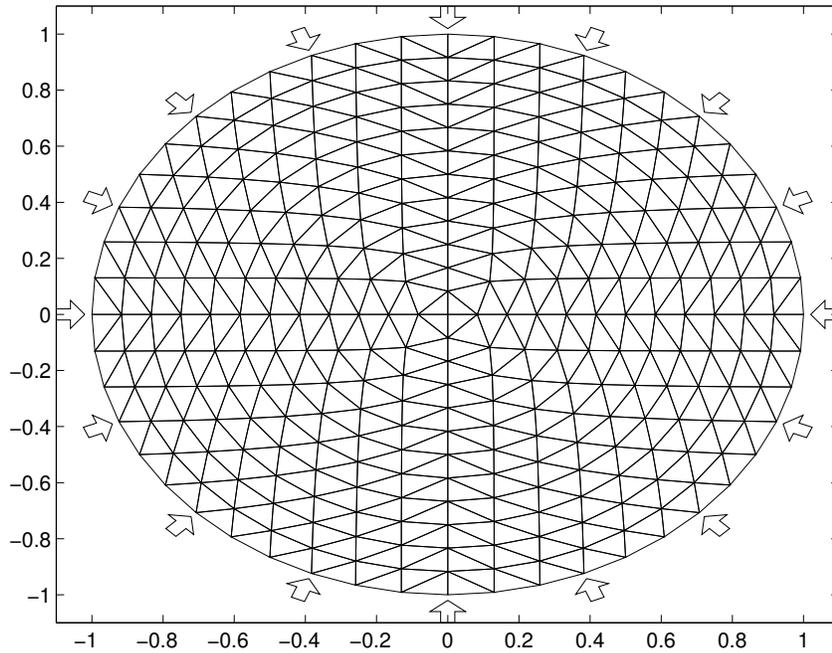
Figure 4.1: Finite Element Model used in this paper.

The results presented in this paper are calculated using the finite element model of figure 4.1, consisting of 572 triangular elements and 16 electrodes, indicated by arrows in the figure. The electrodes correspond to EKG style electrodes used by our tomographic system, and are used for both current injection and voltage measurement.

We linearize the forward problem by finding a matrix **H** and a parametrization f such that $\mathbf{z} = \mathbf{Hx}$ where

$$\mathbf{x} = f\left(\sigma^1\right) - f\left(\sigma^2\right) = \Delta f(\sigma) \tag{4.7}$$

f is chosen so that the linear approximation is valid over the largest possible range. Parametrization is necessary because, while conductivities of 0 and ∞ represent opposite

effects on the voltage distribution, they are not numerically equidistant from the background conductivity; a linear reconstruction algorithm can indicate conductivities decreasing to zero but cannot show increases to ∞. Another problem due to non-parametrization is the difficulty in interpreting reconstructions indicating negative conductivities.

The most commonly used parametrization is the logarithm conductivity, $\mathbf{x} = \log(\sigma^1) - \log(\sigma^2)$, which has the advantage of corresponding to a positive conductivity for any real value of $\mathbf{x}$. The log conductivity also allows easy interpretation of reconstructed values of $\mathbf{x}$: the fractional change in conductivity from σ^1 to σ^2 is

$$\frac{\sigma^1}{\sigma^2} = e^{\mathbf{x}}$$

(4.8)
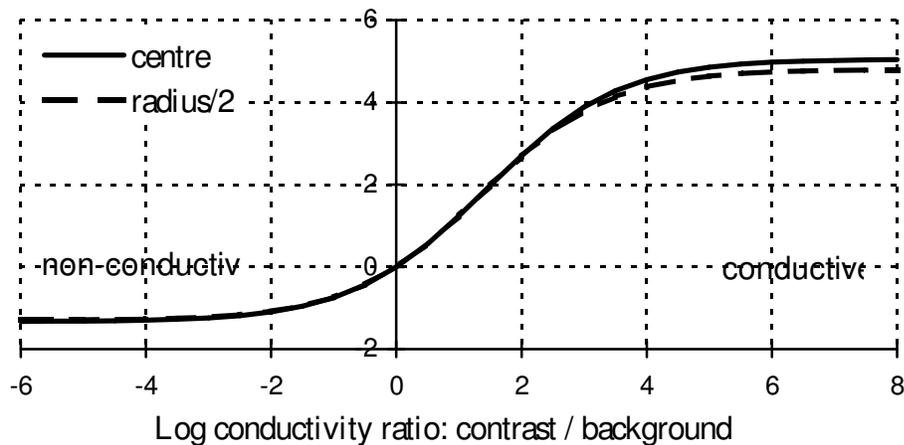
Figure 4.2: Normalised mean signal vs. change in log conductivity contrast ratio.

Figure 4.2 plots the mean signal due to a small contrast in a homogeneous medium normalised with respect to the area of the contrast as a function of the parametrization, $\mathbf{x}$, of equation 4.8. This relationship depends slightly on the radial position, and is shown for a contrast in the centre and half-way to the boundary. This function is linear to within 20% in the region from x = -1 to x = 3, after which the curve saturates, indicating no increase in signal from an increasing contrast. One interesting feature of this graph is the different saturation levels: conductive contrasts produce more signal than non-conductive ones. In clinical applications, however, the range of

physiologically realisable conductivities is relatively small, and the effect of this non-linearity will be reduced.

Another parametrization recently introduced by Shaw (1993) is

$$f(\sigma) = \frac{\sigma^h - \sigma}{\sigma^h + \sigma}$$

(4.9)

where σ^h represents the background conductivity of the medium. This parametrization has the advantages of a larger region of linearity with respect to the signal than the log conductivity, but still does not take into account the different conductive and non-conductive saturation levels. It also introduces the constant σ^h which may be difficult to define in clinical applications where the background is non-uniform.
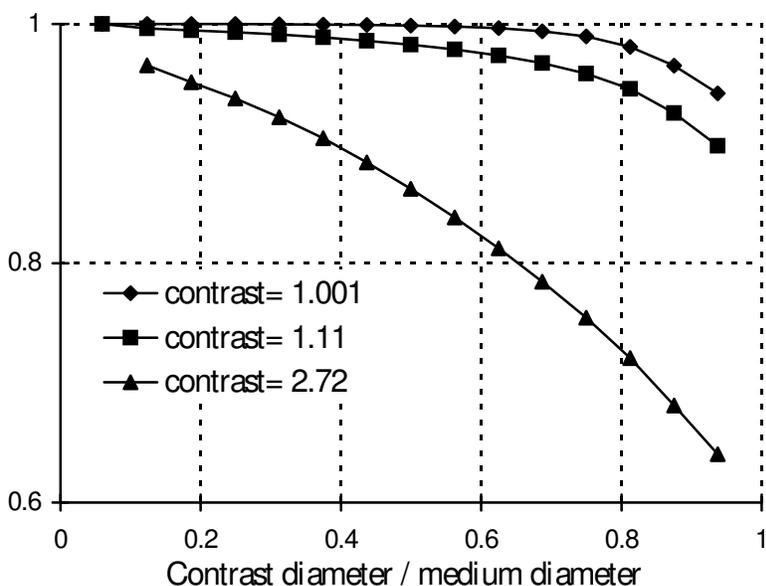
Figure 4.3: Normalised mean signal to area ratio for a circular contrast as a function of the contrast region diameter

Fortunately, in practice, EIT responds linearly to many physiological processes, such as those involving movement of a fluid of a constant conductivity into a region of interest, resulting in an enlargement of the area covered by the fluid. Figure 4.3 shows the normalised ratio of the mean signal from a circular contrast to the contrast area, as a function of the region diameter to medium diameter ratio. The mean signal produced by a change in conductivity in a region is very nearly proportional to the area of the region.

This range of proportionality is much larger than the linear range of figure 4.2. Many physiological activities, such as an accumulation of contrasting fluid, are more accurately modelled in terms of an expanding region of constant contrast, than a fixed region of increasing contrast. It is this characteristic which accounts for the linearity of EIT image amplitude as a function of the intensity of activity for many physiological processes.

In order to calculate the linear approximation matrix, $\mathbf{H}$, we express equation 4.6 in the case of a small change in conductivity distribution: $\sigma^1 = \sigma$, and $\sigma^2 = \sigma + \Delta\sigma$ where $\Delta\sigma \ll \sigma_2$.

$$\mathbf{z}_i = \frac{T[\mathbf{V}(\sigma) - \mathbf{V}(\sigma + \Delta\sigma)]_i}{\frac{1}{2}T[\mathbf{V}(\sigma) + \mathbf{V}(\sigma + \Delta\sigma)]_i} \approx -\frac{T[\mathbf{V}(\sigma + \Delta\sigma) - \mathbf{V}(\sigma)]_i}{T[\mathbf{V}(\sigma)]_i}$$

(4.10)

As a function of the conductivity parametrization $\mathbf{x}_o = f(\ )$, $\mathbf{x} = \Delta f(\ )$,

$$\mathbf{z}_i \approx -\frac{T[\mathbf{V}(f^{-1}(\mathbf{x}_o + \mathbf{x})) - \mathbf{V}(f^{-1}(\mathbf{x}_o))]_i}{T[\mathbf{V}(f^{-1}(\mathbf{x}_o))]_i}$$

(4.11)

Expanding around $\mathbf{x}_O$ for a small change $\mathbf{x}_j$ in each element of $\mathbf{x}$

$$\mathbf{z}_i \approx -\frac{1}{T[\mathbf{V}(f^{-1}(\mathbf{x}_o))]_i} \sum_{j=1}^{N} \left[\frac{T[\mathbf{V}(f^{-1}(\mathbf{x}_o + \mathbf{x}_j)) - \mathbf{V}(f^{-1}(\mathbf{x}_o))]_i}{\mathbf{x}_j} \right] \mathbf{x}_j$$

$$\approx -\frac{1}{T[\mathbf{V}(f^{-1}(\mathbf{x}_o))]_i} \sum_{j=1}^{N} \frac{\partial}{\partial \mathbf{x}_j} \left[T[\mathbf{V}(f^{-1}(\mathbf{x}))]_i \right]_{\mathbf{x}=\mathbf{x}_o} \mathbf{x}_j$$

(4.12)

From this expression, the $\mathbf{H}$ matrix in the linear approximation can be determined.

$$\mathbf{H}_{ij} = -\frac{1}{T[\mathbf{V}(f^{-1}(\mathbf{x}_o))]_i} \frac{\partial}{\partial \mathbf{x}_j} \left[T[\mathbf{V}(f^{-1}(\mathbf{x}))]_i \right]_{\mathbf{x}=\mathbf{x}_o}$$

$$= -\left[\frac{1}{T[\mathbf{V}(\sigma)]_i} \frac{\partial}{\partial \mathbf{x}_j} f^{-1}(\mathbf{x}) \frac{\partial}{\partial \sigma_j} [T[\mathbf{V}(\sigma)]_i] \right]_{\mathbf{x}=\mathbf{x}_o, \sigma = f^{-1}(\mathbf{x}_o)}$$

(4.13)

As a function of the admittance matrix of the FEM, this derivative may be calculated using

$$\frac{\partial}{\partial \sigma_j}\left[T[\mathbf{V}(\sigma)]_i\right] = -T\left[\mathbf{Y}^{-1}(\sigma)\frac{\partial}{\partial \sigma_j}\mathbf{Y}(\sigma)\mathbf{Y}^{-1}(\sigma)\mathbf{C}\right]_i$$

(4.14)

$\mathbf{H}$ is the *sensitivity matrix* of the linear transformation about the "background" conductivity distribution $\mathbf{x_O}$ (using image processing terminology it would be called the *degradation matrix*).

4.5   A MAP Regularized Inverse Model

Our linearized model of EIT can be stated as: Estimate the conductivity parameter $\mathbf{x}$ given a measured signal $\mathbf{z}$ and degradation process

$$\mathbf{z} = \mathbf{Hx} + \mathbf{n}$$

(4.15)

where $\mathbf{n}$ is random noise.   One standard approach used to solve linear estimation problems is the least squares estimate:

$$\hat{\mathbf{x}} = \left(\mathbf{H}^t\mathbf{H}\right)^{-1}\mathbf{H}^t\mathbf{z}$$

(4.16)

This estimate is unsatisfactory for several reasons. In a typical EIT configuration using E=16 or 32 electrodes, the maximum number of independent measurements possible is $\frac{1}{2}E(E-1)$ (Geselowitz, 1971). In order to achieve an acceptable spatial resolution in the reconstructed image the medium must be divided into a sufficient number of independent conductivity elements. As a rough estimate a resolution of 10 % of the medium diameter would require more than 10 conductivity elements in each direction, totalling more than 100 elements. However, the number of independent conductivity regions that can be calculated from these measurements using a least squares estimate is too low. Additionally, the matrix $\mathbf{H}^t\mathbf{H}$ is very poorly conditioned (with a condition number of 8.2×10^{19} for our FEM), because EIT makes current injection and measurement on the medium surface inducing higher current densities near the surface where conductivity contrasts will result in more signal than for contrasts in the centre. This kind of ill-conditioning problem is classic in image reconstruction and can be effectively approached using regularization.

The maximum a posteriori (MAP) approach to image reconstruction defines the solution as the most likely estimate $\hat{\mathbf{x}}$ given the measured signal $\mathbf{z}$ and certain statistical information about the medium. We choose this approach because it allows an elegant interpretation of the image reconstruction algorithm in terms of the statistical properties of the experimental situation. Non statistical models such as Tikhonov regularization can be used to express the image reconstruction algorithm presented here, but, we feel, make the significance of the various reconstruction parameters less clear. Additionally, the MAP approach can be implemented using relatively simple matrix algebra compared to other regularization techniques such as the truncated singular value decomposition or iterative techniques such as constrained least squares. This section summarises the details of the MAP approach which are more fully explained by Demoment (1989) and Fortier (1993). The following sections explain how this approach is applied to EIT image reconstruction.

In order to simplify the reconstruction algorithm, we assume that the image statistical properties can be modelled by a Gaussian distribution of mean $\mathbf{x}_\infty$ and covariance $\mathbf{R}_x$:

$$\mathbf{x}_\infty = \mathrm{E}[\mathbf{x}] \tag{4.17}$$

$$\mathbf{R}_x = \mathrm{E}\left[(\mathbf{x} - \mathbf{x}_\infty)^t (\mathbf{x} - \mathbf{x}_\infty)\right] = \mathrm{E}\left[\mathbf{x}^t \mathbf{x}\right] - \mathbf{x}_\infty{}^t \mathbf{x}_\infty \tag{4.18}$$

Given these parameters we can model the distribution function of the image, $f(\mathbf{x})$

$$f(\mathbf{x}) = \frac{1}{(2\pi)^{N/2}\sqrt{|\mathbf{R}_x|}} e^{-\frac{1}{2}(\mathbf{x} - \mathbf{x}_\infty)^t \mathbf{R}_x^{-1}(\mathbf{x} - \mathbf{x}_\infty)} \tag{4.19}$$

The *a posteriori* distribution function of $\mathbf{z}$ given a conductivity distribution $\mathbf{x}$ is derived from the definition of the problem (equation 4.15).

$$f(\mathbf{z}|\mathbf{x}) = \frac{1}{(2\pi)^{M/2}\sqrt{|\mathbf{R}_n|}} e^{-\frac{1}{2}(\mathbf{z} - \mathbf{Hx})^t \mathbf{R}_n^{-1}(\mathbf{z} - \mathbf{Hx})} \tag{4.20}$$

The difference $\tilde{\mathbf{z}}\mathbf{Hx}$ is entirely due to the noise $\mathbf{n}$, which is assumed to be Gaussian, white, zero mean with covariance $\mathbf{R}_n$. Thus

$$\mathbf{R}_n = \mathrm{E}\!\left[\mathbf{n}\mathbf{n}^t\right] = \begin{bmatrix} \sigma_1^2 & 0 & \cdots & 0 \\ 0 & \sigma_2^2 & & 0 \\ \vdots & & \ddots & \vdots \\ 0 & 0 & \cdots & \sigma_M^2 \end{bmatrix}$$

(4.21)

where σ, in this and all subsequent equations in this paper, represents the square root of the variance and not the conductivity.

The MAP estimate, $\hat{\mathbf{x}}$, maximises the *a posteriori* probability distribution $f(\mathbf{x}|\mathbf{z})$. This can be understood as finding the most likely image, $\mathbf{x}$, to have produced the measured signal, $\mathbf{z}$.

$$f(\mathbf{x}|\mathbf{z}) = \frac{f(\mathbf{z}|\mathbf{x})f(\mathbf{x})}{f(\mathbf{z})}$$

$$= \frac{e^{-\frac{1}{2}\left[(\mathbf{z}-\mathbf{Hx})^t \mathbf{R}_n^{-1}(\mathbf{z}-\mathbf{Hx}) + (\mathbf{x}-\mathbf{x}_\infty)^t \mathbf{R}_x^{-1}(\mathbf{x}-\mathbf{x}_\infty)\right]}}{(2\pi)^{(M+N)/2}\sqrt{|\mathbf{R}_x||\mathbf{R}_n|}\,f(\mathbf{z})}$$

(4.22)

$f(\mathbf{x}|\mathbf{z})$ is maximised when the exponent is minimised

$$\hat{\mathbf{x}} = \arg\min_x \left[(\mathbf{z}-\mathbf{H}\hat{\mathbf{x}})^t \mathbf{R}_x^{-1}(\mathbf{z}-\mathbf{H}\hat{\mathbf{x}}) + (\hat{\mathbf{x}}-\mathbf{x}_\infty)^t \mathbf{R}_n^{-1}(\hat{\mathbf{x}}-\mathbf{x}_\infty)\right]$$

(4.23)

yielding the estimate

$$\hat{\mathbf{x}} = \left(\mathbf{H}^t \mathbf{R}_n^{-1}\mathbf{H} + \mathbf{R}_x^{-1}\right)^{-1}\left(\mathbf{H}^t \mathbf{R}_n^{-1}\mathbf{z} + \mathbf{R}_x^{-1}\mathbf{x}_\infty\right)$$

(4.24)

4.6   Parameters of the MAP estimate

The noise covariance, $\mathbf{R}_n$, measures the noise power in each component of the signal. Measurement noise on each channel of the tomograph can be determined from the hardware; in this paper we consider each channel to have equal noise variance σ_n. $\mathbf{R}_n$ is calculated using the definition of the signal [equation 4.6]

$$[\mathbf{R}_n]_{ii} = \left(\sigma_n / \mathbf{v}_i^h\right)^2$$

(4.25)

where $\mathbf{v}^h$ is the measurements from the medium on which the noise measurements were taken. We define a matrix $\mathbf{W}$ such that $\sigma_n^2 \mathbf{W} = \mathbf{R}_n^{-1}$.

One convenient use of this matrix is to naturally deal with data sets containing faulty electrodes or measurement channels, which introduce large errors into the images. In the case of a faulty electrode, we assume that the noise on all signal components using that electrode is infinite, and the corresponding elements of $\mathbf{R}_n^{-1}$ are replaced with zeros. This formulation will then reconstruct the conductivity image corresponding to a reduced data set, which excludes the erroneous measurements.

The properties of the image $\mathbf{R}_x$ and $\mathbf{x}_\infty$ are less concrete than the noise properties and can only be estimated from a knowledge of the experimental configuration. The expected change in the image E[$\mathbf{x}$] is represented by $\mathbf{x}_\infty$. Without any specific knowledge of the physiological system being measured, conductivity changes are equally likely to be conductive as non-conductive; the expected image is therefore one of no conductivity change, and is best modelled by $\mathbf{x}_\infty = 0$.

The covariance of the image $\mathbf{R}_x$ includes information on the amplitude of the image and also on the spatial frequency distribution. The diagonal elements $[\mathbf{R}_x]_{ii}$ represent the variance of the amplitude of each image element, whereas the off diagonal elements are a function of the correlation coefficient r between a pixel in element i and a pixel in element j.

$$[\mathbf{R}_x]_{ij} = r\sqrt{[\mathbf{R}_x]_{ii}[\mathbf{R}_x]_{jj}}$$

(4.26)

Since EIT has low spatial resolution due to the small number of measurements, it is unable to detect high spatial frequency contrasts in the image, indicating that the spatial frequency of the reconstructed distribution of conductivity change has little high frequency content. Therefore, elements close to each other will have correlated reconstructed values. Image reconstruction algorithms which assume no correlation between pixels tend to produce results dependent on the number of elements into which the medium is divided, because the area within each element, which is effectively forced to be correlated, becomes uncorrelated as the area is split into several elements.

Instead of using equal image pixel variance, some groups (Shaw, 1993; Woo, 1993) use a scaled diagonal $\mathbf{R}_x$ matrix such that

$$[\mathbf{R}_x]_{ii} = \left|\mathbf{H}^t\mathbf{H}\right|_{ii} = \sum_j \mathbf{H}_{ji}^2$$

(4.27)

We avoid this approach as it tends to "push" reconstructed contrasts toward the centre of the medium. Instead, diagonal elements of $\mathbf{R}_x$ are set to σ_x^2, while the off-diagonal elements account for the resolution of the medium. For instance, using 16 electrodes there is not enough information to "see" resolution on the order of 5 % of the medium diameter. We assume that pixels closer than this distance are highly correlated and pixels further apart are not correlated, with a gradual diminishing between the two extremes. $\mathbf{R}_x$ can be interpreted as a spatial low pass filter.

Unfortunately, this formulation is numerically unstable and difficult to invert. Instead, we construct a regularization matrix, $\mathbf{Q}$, directly using a high pass filter to represent $\mathbf{R}_x^{-1}$. A Gaussian high pass filter of spatial frequency ω_0 has the form

$$F(u, v) = 1 - e^{-\omega_0\left(u^2 + v^2\right)}$$

(4.28)

using Fourier transform, the convolution kernel in the spatial domain is

$$f(x, y) = \delta(x, y) - \frac{\pi}{\omega_0^2} e^{-\frac{\pi^2}{\omega_0^2}\left(x^2 + y^2\right)}$$

(4.29)

where $\delta(x,y)$ is the Dirac delta function. The filtering matrix $\mathbf{F}$ multiplies an image vector $\mathbf{x}$ to give a filtered image $\mathbf{Fx}$. $\mathbf{F}_{ij}$ is calculated by centring the high pass filter in element i and integrating across element j

$$\mathbf{F}_{ij} = \int_{E_j} \left[\delta(x - x_i, y - y_i) - \frac{\pi}{\omega_0^2} e^{-\frac{\pi^2}{\omega_0^2}\left((x - x_i)^2 + (y - y_i)^2\right)}\right] dxdy$$

(4.30)

where E_j is the area of the element j and the centre of element i is (x_i, y_i) . This integration was performed numerically on a mesh of 512×512 pixels. We find it more convenient to express the filter cut-off frequency ω_0 in terms of the percentage of the diameter. Using a grid of $N_p \times N_p$ pixels,

$$(\% \text{ diameter}) = \frac{N_p}{2\pi\omega_0}$$

(4.31)

The regularization matrix $\mathbf{Q}$ is required to be symmetrical, and is calculated from

$$\mathbf{Q} = \sigma_x^2 \mathbf{F}^t \mathbf{F} \tag{4.32}$$

Since the filter convolution kernel has infinite extent, this formulation does not integrate over the complete domain of the filter. The sum of each row of $\mathbf{F}$ will therefore not equal zero but be slightly positive, especially for those elements which are close to the medium boundary, indicating that the filter will include some filtering component at all spatial frequencies. This behaviour is necessary in order for $\mathbf{Q}$ to be non-singular.

This formulation of regularization may be interpreted as a penalization on high frequency components in the reconstructed image. Regularization thus tends to improve the conditioning of the inverse solution at the expense of a degradation in the resolution.

4.7 Regularization Parameter

Using this formulation of the regularized inverse there remain two free parameters, σ_n and σ_x, which we combine into a single hyper-parameter μ which controls the amount of smoothing of the solution

$$\mu = \frac{\sigma_x^2}{\sigma_n^2} \tag{4.33}$$

from which we have the regularized inverse

$$\hat{\mathbf{x}} = \left(\mathbf{H}^t \mathbf{W} \mathbf{H} + \mu \mathbf{Q}\right)^{-1} \mathbf{H}^t \mathbf{W} \mathbf{z} = \mathbf{B}(\mu)\mathbf{z} \tag{4.34}$$

where $\mathbf{B}(\mu)$ is the image reconstruction matrix for a given value of μ. We calculate a matrix $\mathbf{B}$ and multiply by $\mathbf{z}$ rather than solving the linear system as this allows the imaging problem to be separated into off-line and on-line sections. $\mathbf{B}$ is calculated once for a given application; subsequent on-line calculation of the image from the measurements requires only a matrix multiplication, followed by mapping of $\mathbf{x}$ onto the finite element model, which is much less time consuming than solving the linear system. Using the FEM of figure 4.1 on a SUN SPARC 10/30 computer, the calculation of $\mathbf{B}$ requires 537 seconds, while the subsequent matrix multiplication and image reconstruction requires 0.25 seconds. With some optimisation, this algorithm could be used for real-time imaging.

Many criteria can be used to guide the selection of this hyper-parameter of the MAP model (Galatanos, 1992). The value of μ depends on many factors such as the number of finite elements in the image, and the regularization matrices $\mathbf{W}$ and $\mathbf{Q}$. In order to take these factors into account, we select the regularization parameter in order to control the amplification of noise in the reconstructed image. Using the communications systems model of figure 4.4, we consider the reconstruction matrix to be a signal receiver: at the input there is a signal $\mathbf{z}$ and noise $\mathbf{n}$ producing the output signal $\mathbf{Bz}$ with noise $\mathbf{Bn}$.
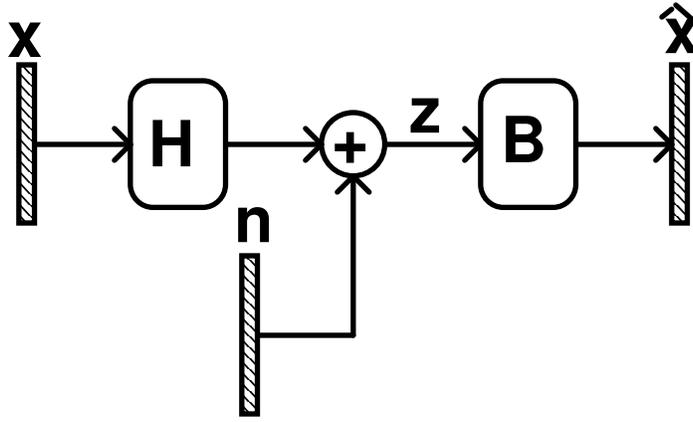
Figure 4.4: Equivalent communications systems block diagram

The signal to noise ratio of a random variable s is

$$\mathrm{SNR}_s = \frac{\mathrm{E}[s]}{\sqrt{\mathrm{Var}[s]}} = \frac{\frac{1}{N}\sum_{i=1}^{N} s_i}{\sqrt{\frac{1}{N}\sum_{i=1}^{N}(s_i - \bar{s})^2}}$$

(4.35)

Using this definition, the SNRs for the input and output signals, $\mathbf{z}$ and $\mathbf{x}$ can be calculated.

$$\mathrm{SNR}_{\mathrm{in}} = \frac{\mathbf{1}^t \mathbf{z}}{\sqrt{M \cdot \mathrm{trace}\,\mathbf{R}_n}} = \frac{\mathbf{1}^t \mathbf{z}}{\sigma_n \sqrt{M \cdot \mathrm{trace}\,\mathbf{W}^{-1}}}$$

(4.36)

$$\mathrm{SNR}_{\mathrm{out}} = \frac{\mathbf{1}^t \mathbf{ABz}}{\sqrt{N \cdot \mathrm{trace}\left(\mathbf{ABR}_n\mathbf{B}^t\mathbf{A}\right)}} = \frac{\mathbf{1}^t \mathbf{ABz}}{\sigma_n \sqrt{N \cdot \mathrm{trace}\left(\mathbf{ABW}^{-1}\mathbf{B}^t\mathbf{A}\right)}}$$

(4.37)

where $\mathbf{1}$ represents a column vector of ones, $\mathbf{A}$ is a diagonal matrix such that A_{ii} is the area of element i, and M and N represent the number of measurements and image elements, respectively. The noise figure (NF) is the output SNR to input SNR ratio. This NF depends only on the reconstruction matrix and is a function of μ.

$$NF = \frac{SNR_{in}}{SNR_{out}} = \frac{\left(\mathbf{1}^t \mathbf{z}\right)\sqrt{N \cdot \mathrm{trace}\left(\mathbf{ABW}^{-1}\mathbf{B}^t\mathbf{A}\right)}}{\left(\mathbf{1}^t \mathbf{ABz}\right)\sqrt{M \cdot \mathrm{trace}\left(\mathbf{W}^{-1}\right)}}$$

(4.38)

The signal used in this definition is $\mathbf{z} = \mathbf{Hx}_C$, where $\mathbf{x}_C$ is a small contrast in the centre of the medium. In a given application, the desired noise figure for the reconstruction algorithm is chosen from a knowledge of the signals of interest and the level of noise present, and the value of μ corresponding to this NF is used.

The reconstruction matrix with the minimum possible NF is calculated by the limit

$$\mathbf{B}_{min\mathrm{NF}} = \lim_{\mu \to \infty} \left(\mathbf{H}^t\mathbf{WH} + \mu\mathbf{Q}\right)^{-1}\mathbf{H}^t\mathbf{W} = \frac{1}{\mu}\mathbf{Q}^{-1}\mathbf{H}^t\mathbf{W}$$

(4.39)

At this lower limit, $\mathbf{B}$ corresponds to the sensitivity matrix formulation for an appropriate choice of the matrix $\mathbf{Q}$. For instance, the algorithm of Gencer (1992), can be formulated as $\mathbf{B} = \mathbf{Q}^{-1}\mathbf{H}^t\mathbf{W}$ where $\mathbf{Q}$ is a diagonal matrix such that

$$\mathbf{Q}_{ii} = \left[\mathbf{H}^t\mathbf{WH}\right]_{ii}$$

(4.40)

There is no practical upper limit to the noise figure; decreasing μ will increase NF until the matrix inversion becomes numerically unstable. Of course, a reconstruction matrix which amplifies noise to this extent has no practical application. The NF is a practical figure of merit with which to compare the noise performance of EIT image reconstruction algorithms. Figure 4.5 illustrates the effect of the NF on the image reconstruction, where each image is shown as a wire frame mesh on the left hand side and as a grey-scaled image on the right. Figure 4.5A shows the pattern to be imaged: two small conductive contrasting regions in a circular medium separated by one third of the diameter. This pattern was simulated on a much finer finite element mesh than was used for the image reconstruction. Figures 4.5B, D, and F are reconstructed using the voltage measurements from 4.5A with no noise added, while figures C, E, and G use the measurements with SNR of -3 dB. Reconstructions in B and C use weighted backprojection, D and E use a reconstruction matrix $\mathbf{B}_1$, and F and G, matrix $\mathbf{B}_2$. Both reconstruction matrices are calculated with a spatial filter matrix $\mathbf{Q}$ filtering 10% of the diameter; the NF of $\mathbf{B}_2$ is 2.0, while that of $\mathbf{B}_1$ is 0.4, equivalent to that of backprojection.
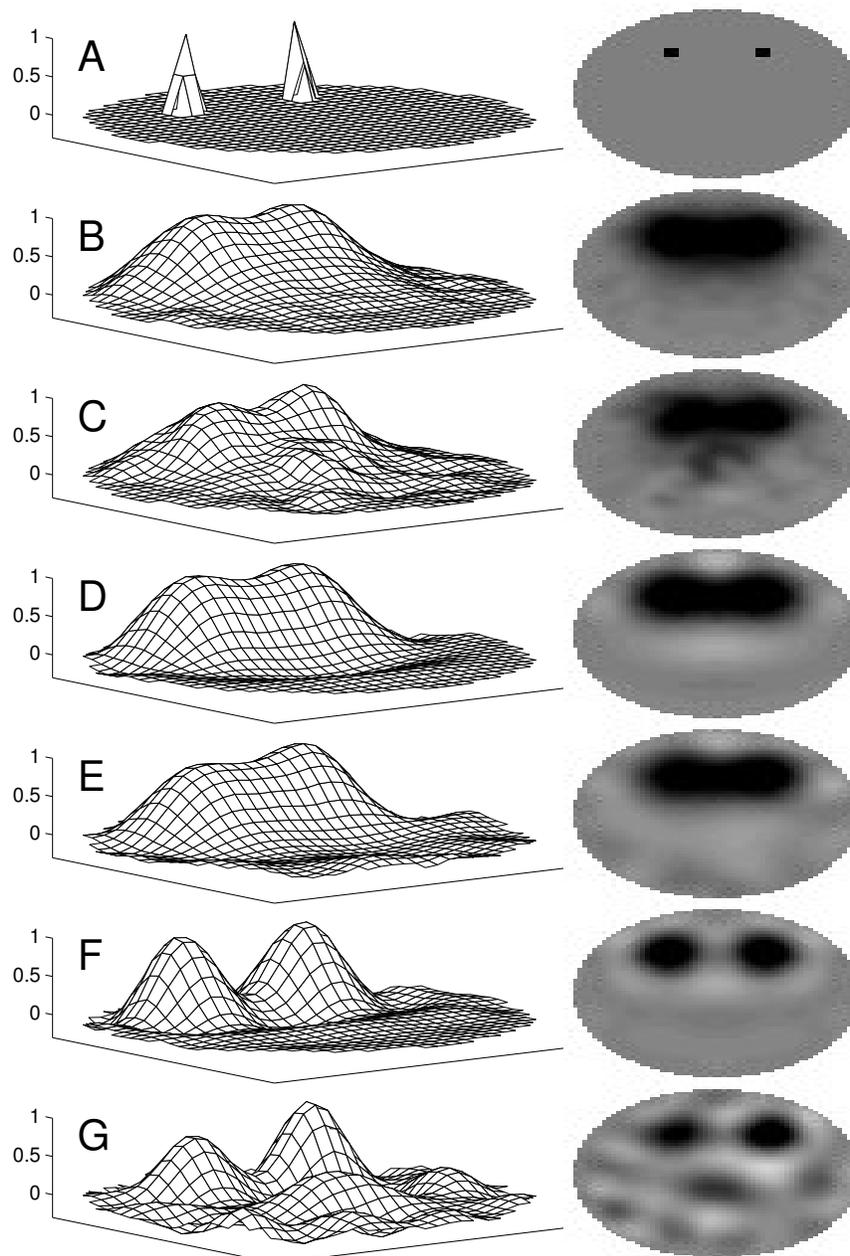
Figure 4.5: Reconstructed Images

A: Generating Conductivity Distribution

B: Measurements: No Noise   Reconstruction: $\mathbf{B}_{ebp}$

C: Measurements: -3dB SNR Reconstruction: $\mathbf{B}_{ebp}$

D: Measurements: No Noise   Reconstruction: $\mathbf{B}_1$, NF=0.4

E: Measurements: -3dB SNR   Reconstruction: $\mathbf{B}_1$, NF=0.4

F: Measurements: No Noise   Reconstruction: $\mathbf{B}_2$, NF=2.0

G: Measurements: -3dB SNR   Reconstruction: $\mathbf{B}_2$, NF=2.0

Matrix $\mathbf{B}_2$ has better spatial resolution at the expense of reduced ability to reject noise. Conversely, $\mathbf{B}_1$ has significantly improved noise performance with a reduction in spatial resolution compared to $\mathbf{B}_2$ but has better resolution than backprojection with equivalent noise performance.

4.8 Algorithm Performance

Evaluating the performance of EIT reconstruction algorithms is made difficult because the spatial resolution and sensitivity of EIT is highly dependent on the radial position. Seagar (1987) presents an approach which characterises an image reconstruction algorithm on the basis of the figures of merit: resolution, accuracy, and contrast. We propose that the accuracy and contrast can be more naturally described by the noise figure and the detectability of a contrast. We also introduce a new figure of merit to measure the precision of localisation of the imaging.

The resolution quantifies how close two contrasts must be before the reconstruction will blur them into one form, and is a function of the point spread function of a small contrast. Because of the higher current densities near the boundary, there is considerably more sensitivity at the boundary than in the medium centre, and the resolution, which depends on the sensitivity, improves significantly as a contrast moves towards the boundary. We define the blur radius (BR) as a measure of the resolution.

$$\mathrm{BR} = \frac{r_z}{r_o} = \sqrt{\frac{A_z}{A_o}}$$

(4.41)

where r_o and A_o are the radius and area, respectively, of the medium, and r_z and A_z are the radius and area of the zone containing half the magnitude of the reconstructed image from a point contrast. Thus $A_o = \mathrm{trace}\ \mathbf{A}$, and

$$A_z = \sum A_{ii} \text{ for all } i \text{ such that } \mathbf{x}_i > \delta$$

(4.42)

where the threshold δ is defined such that

$$\left(\sum \mathbf{x}_i \text{ for all } i \text{ such that } \mathbf{x}_i > \delta \right) = \tfrac{1}{2} \left(\sum \mathbf{x}_i \text{ for all } i \right)$$

(4.43)

We use this definition based on the image magnitude rather than the more traditional definition of width at half maximum, because the image maximum has a

higher variance due to noise than the image magnitude. This definition is also more convenient when defining the probability of detection of a conductivity change.

The precision of localisation of the imaging measures how well the position of an object is reconstructed. Many algorithms, especially the backprojection algorithm, tend to "push" a reconstructed object towards the centre of the medium. We measure this tendency with the position error (PE)

$$PE = \rho_{simulated} - \rho_{reconstructed} \tag{4.44}$$

where ρ is the radial position. Thus, a positive PE indicates that a contrast is imaged closer to the centre than it should be. The reconstructed position is defined as the centre of gravity of the zone, A_z, used to define the blur radius.

There are two adjustable parameters in this reconstruction technique, the regularization parameter, expressed in terms of the NF, and the filter low-pass cut-off frequency ω_O, expressed in terms of diameter percentage. Figure 4.6 plots the PE as a function of radial position for different NFs with a filter of 10% diameter, and figure 4.7 plots the BR as a function of radial position under the same conditions. In both of these graphs the performance of the reconstruction improves with increasing NF.

Figure 4.6: Position error vs. radial position for different noise figures
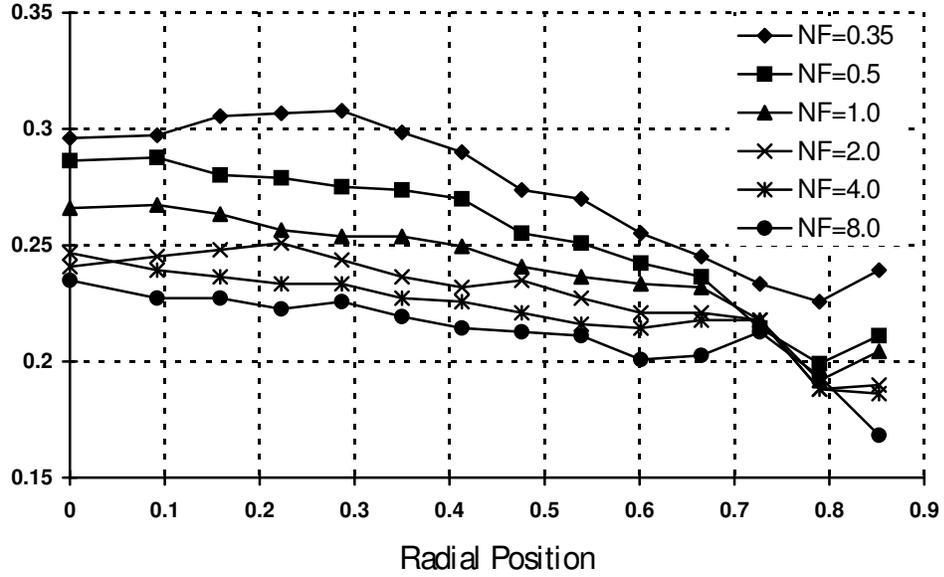
Figure 4.7: Blur radius vs. radial position for different noise figures

Using these criteria the different algorithms proposed by various groups can be compared with the approach presented here. The following six reconstruction matrices are calculated:

$$\mathbf{B}_5 = \left(\mathbf{H}^t\mathbf{W}\mathbf{H} + \mu\mathbf{F}_5^t\mathbf{F}_5\right)^{-1}\mathbf{H}^t\mathbf{W}$$

$$\mathbf{B}_{10} = \left(\mathbf{H}^t\mathbf{W}\mathbf{H} + \mu\mathbf{F}_{10}^t\mathbf{F}_{10}\right)^{-1}\mathbf{H}^t\mathbf{W}$$

$$\mathbf{B}_{20} = \left(\mathbf{H}^t\mathbf{W}\mathbf{H} + \mu\mathbf{F}_{20}^t\mathbf{F}_{20}\right)^{-1}\mathbf{H}^t\mathbf{W}$$

$$\mathbf{B}_I = \left(\mathbf{H}^t\mathbf{W}\mathbf{H} + \mu\mathbf{I}\right)^{-1}\mathbf{H}^t\mathbf{W}$$

$$\mathbf{B}_Q = \left(\mathbf{H}^t\mathbf{W}\mathbf{H} + \mu\mathbf{Q}_S\right)^{-1}\mathbf{H}^t\mathbf{W}$$

$$\mathbf{B}_{ebp}$$

$$(4.45)$$

The matrices $\mathbf{B}_5$, $\mathbf{B}_{10}$, and $\mathbf{B}_{20}$ are calculated using the method presented here with the spatial filter cut-off frequency set to filter 5%, 10%, and 20% of the diameter, respectively. $\mathbf{B}_I$ corresponds to the method of Yorkey (1987), and $\mathbf{B}_Q$ corresponds to the method of Woo (1993), where the $\mathbf{Q}_S$ is a diagonal matrix such that

$$\left[\mathbf{H}^t\mathbf{W}\mathbf{H}\right]_{ii} = \left[\mathbf{Q}_S\right]_{ii}$$

$$(4.46)$$

The $\mathbf{B}_{ebp}$ is calculated by mapping the equipotential backprojection formulation of Barber (1987) onto our finite element mesh and scaling the resulting matrix by the backprojection filter. Each element i,j of $\mathbf{B}_{ebp}$ is

$$\left[\mathbf{B}_{ebp}\right]_{ij} = \int\limits_{E_i}\left[\frac{1-x^2-y^2}{\left(x-x_j\right)^2+\left(y-y_j\right)^2}\right]dxdy$$

(4.47)

if element i is in the equipotential region for current injection pattern j and zero otherwise. The co-ordinates (x,y) are integrated across the area of element i, and (x_j,y_j) is the location of the current injection dipole. The NF of $\mathbf{B}_{ebp}$ was calculated to be 0.40. In order to meaningfully compare the different techniques, the regularization parameter μ for each reconstruction matrix was selected so all NFs equalled that of backprojection.

Figure 4.8 compares these algorithms in position error as a function of radial position, and figure 4.9 in blur radius versus radial position. In comparing these algorithms, the one that immediately stands out as having the poorest resolution and the highest position error is backprojection. Of the remaining algorithms, the one with the lowest, and most uniform BR is $\mathbf{B}_Q$. This performance, however, is achieved at the price of a significantly larger position error. It seems that the use of a scaled matrix $\mathbf{Q}$ introduces a bias into the reconstruction.
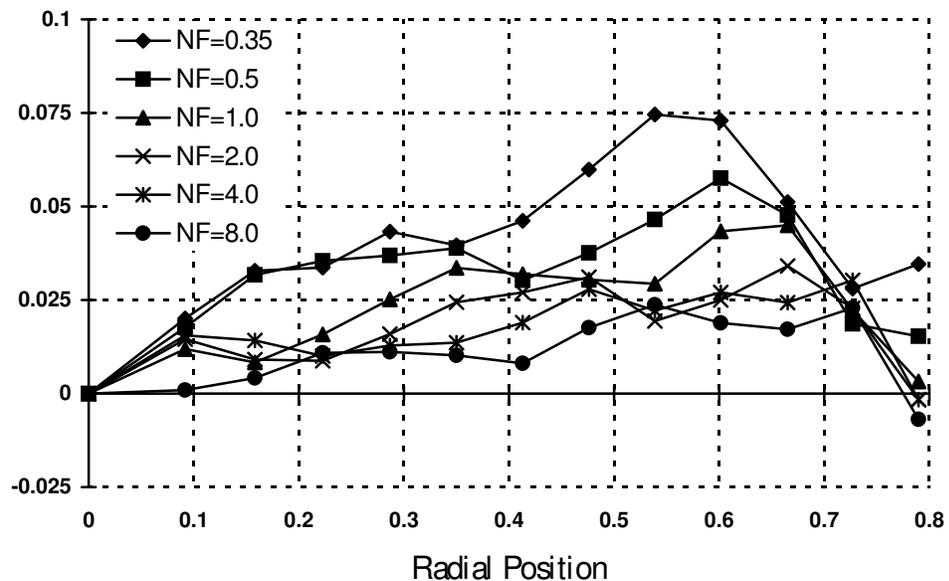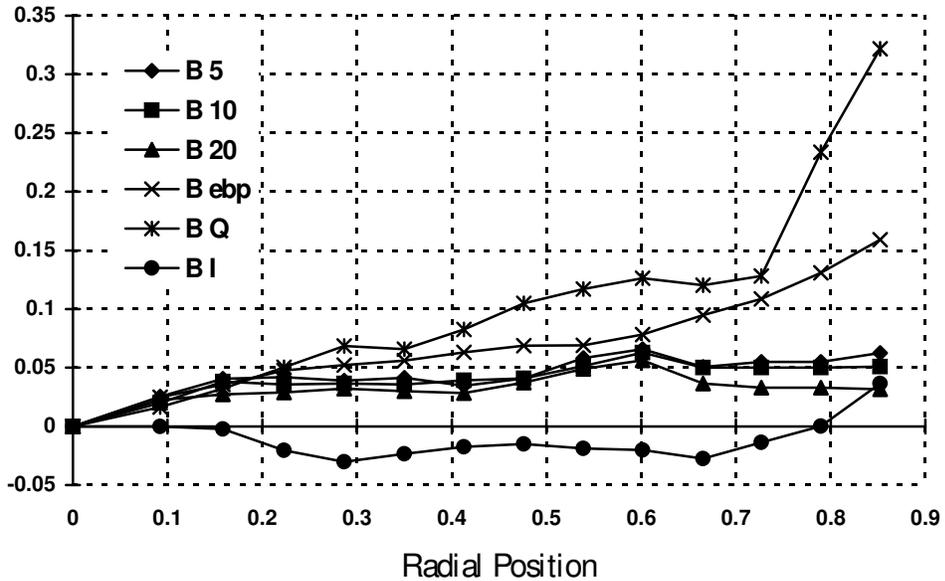

Figure 4.8: Position error vs. radial position for different algorithms
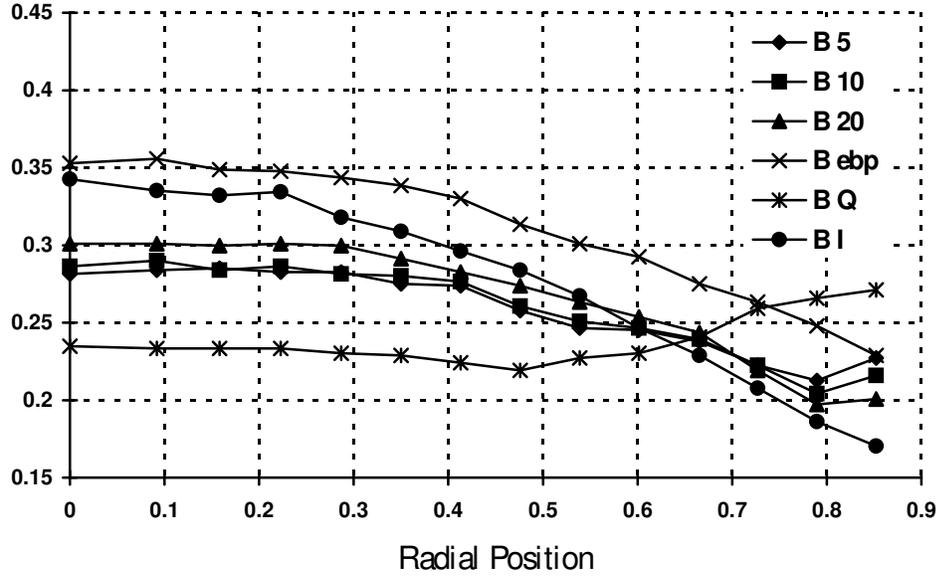
Figure 4.9: Blur radius vs. radial position for different algorithms

Besides these two, the algorithms perform similarly, except for a trade-off of resolution in the centre for resolution on the boundary. For instance, while $\mathbf{B_5}$ has the lowest BR in the centre, it has the highest on the boundary. At the opposite extreme is $\mathbf{B_{20}}$ and $\mathbf{B_I}$. It is natural that $\mathbf{B_I}$ would continue the trend of increasing filter diameter ratio, because the identity matrix is the limiting case for very large filter wavelength. The best overall compromise of image resolution while avoiding significant PE is $\mathbf{B_{10}}$.

4.9 Quantitative Imaging

Although EIT is typically used for detection and monitoring of conductivity changes, it is important to understand how well the reconstruction process conserves the image amplitude, at least in the region where the linear approximation is valid. Given a conductivity change $\mathbf{x}$, the image reconstruction process calculates an estimate $\hat{\mathbf{x}} = \mathbf{BHx}$. While this reconstruction degrades the image resolution, it should not affect the total image magnitude. We define the quantitative gain (QG) as a figure of merit for the average amplification of the images by the reconstruction. By summing the contribution of a uniform signal in each element of $\mathbf{x}$,

$$QG = \frac{\sum\limits_{i,j} [\mathbf{ABH}]_{ij}}{\sum\limits_{i,j} \mathbf{A}_{ij}}$$

(4.48)
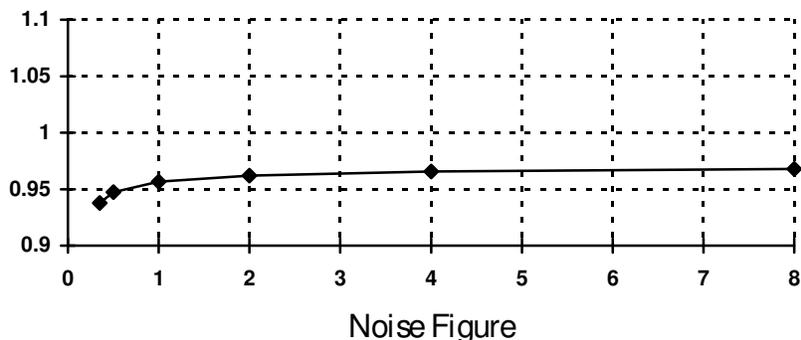
Figure 4.10: Quantitative Gain versus Noise Figure

Figure 4.9 shows the QG versus the NF for a 10% diameter spatial filter. Except for NF close to the minimum value, $NF_{min} = 0.26$, the QG remains constant at a value of 0.97, indicating that the reconstructed images can be interpreted quantitatively. This is not the case for backprojection, however, where the QG is significantly greater than one, and also depends on the number of elements into which the medium is divided.

4.10 Contrast detection

In many practical clinical applications, EIT is used to detect conductivity changes in various organs, and it is important to be able to quantify this capability in order to determine, for a given application, whether the quantities of interest will be detectable.

Using the model of figure 4.4, and a communications systems approach to calculating the error probability, the following quantities can be identified. Given a symmetric channel where one of two possible signals $\mathbf{z}$ associated with the presence or absence of a conductivity contrast, $\mathbf{x}_O$, is transmitted across the channel $\mathbf{B}$ to the receiver. Thus,

$$\mathbf{z} = \begin{cases} \mathbf{Hx}_0 + \mathbf{n} \\ \mathbf{n} \end{cases}$$

(4.49)

The receiver, $\mathbf{r}$, consists of summing the reconstructed elements conductivities in a region of interest surrounding the expected conductivity change. The received signal is a scalar, s, with possible values

$$s = \begin{cases} s_o + n \\ n \end{cases} = \begin{cases} \mathbf{r}^t\mathbf{ABHx}_0 + \mathbf{r}^t\mathbf{ABn} \\ \mathbf{r}^t\mathbf{ABn} \end{cases}$$

(4.50)

where the noise n has zero mean and variance

$$\sigma^2 = E\left[\left(\mathbf{r}^t\mathbf{ABn}\right)^2\right] = \mathbf{r}^t\mathbf{ABR}_n\mathbf{B}^t\mathbf{Ar} = \sigma_n^2\mathbf{r}^t\mathbf{ABW}^{-1}\mathbf{B}^t\mathbf{Ar}$$

(4.51)

By setting the decision threshold at $s_0/2$, the probability of non-detection (the probability of error) can be shown to be (Papoulis, 1984)

$$P(\varepsilon) = \tfrac{1}{2}\,\mathrm{erfc}\left(\frac{1}{2\sqrt{2}}\frac{s_0}{\sigma}\right)$$

(4.52)

where *erfc* is the complimentary error function, and s_0/σ is the signal to noise ratio at the receiver. The simplest receiving filter uses the entire image as the received signal. In this case the receiving filter $\mathbf{r}$ is a vector of ones, $\mathbf{1}$. This result can be related to the definition of SNR_{out} (equation 4.36), for an object in the centre of the medium $\mathbf{x}_c$, multiplied by a factor, K, which takes into account the covariance between the elements summed together in the receiver.

$$K = \sqrt{\frac{N\cdot\mathrm{trace}\left(\mathbf{ABW}^{-1}\mathbf{B}^t\mathbf{A}\right)}{\mathbf{1}^t\mathbf{ABW}^{-1}\mathbf{B}^t\mathbf{A1}}}$$

(4.53)

For an arbitrary object $\mathbf{x}_0$, the SNR_{out} must be multiplied by a gain factor G

$$G = \frac{\mathbf{1}^t\mathbf{Hx}_0}{\mathbf{1}^t\mathbf{Hx}_c}$$

(4.54)

The probability of non-detection is, thus, a function of the original image, $\mathbf{x}$, the NF and the SNR_{in}.

$$P(\varepsilon) = \tfrac{1}{2}\,\mathrm{erfc}\!\left(\tfrac{1}{2\sqrt{2}}\,\mathrm{SNR}_{\mathrm{out}}\times G\times K\right) = \tfrac{1}{2}\,\mathrm{erfc}\!\left(\tfrac{1}{2\sqrt{2}}\,\frac{G\times K}{\mathrm{NF}}\,\mathrm{SNR}_{\mathrm{in}}\right)$$

(4.55)

This expression provides a natural way of understanding the significance of the NF parameter. As the noise figure increases, the image becomes noisier and probability of failing to detect contrasts in the reconstructed image increases, while at the same time, the resolution improves, increasing the precision of locating contrasts. The choice of compromise between resolution and noise performance can be based on this calculation. For example, in a clinical monitoring situation with EIT equipment of known noise output in which we want to be able to reliably detect 10 ml of fluid movement, the NF must be selected to constrain the probability of error from this signal to a desired tolerance.

This simple receiving filter is in fact a poor choice; it is possible, however, to improve this $P(\varepsilon)$ by using a receiving filter which is optimised to the region of interest in the image, and thereby rejecting noise outside of this region. We select a receiving filter which contains the blur region from a point contrast in the original image. By definition BR contains half the image magnitude, while the noise variance will decrease by the reduction in area due to the region of interest, $(\mathrm{BR})^2$, assuming that the noise variance is constant across the image. Even though this assumption is not valid, it allows an approximation of the improvement in detectability afforded by using a region of interest. The SNR in the region of interest will be

$$\mathrm{SNR}_{\mathrm{roi}} = \frac{1}{2\times(\mathrm{BR})^2}\,\mathrm{SNR}_{\mathrm{out}}$$

(4.56)

and the probability of non-detection of a contrast in a region of interest is

$$P(\varepsilon) = \tfrac{1}{2}\,\mathrm{erfc}\!\left(\tfrac{1}{2\sqrt{2}}\,\mathrm{SNR}_{\mathrm{roi}}\times G\times K\right) = \tfrac{1}{2}\,\mathrm{erfc}\!\left(\tfrac{1}{4\sqrt{2}}\,\frac{G\times K}{\mathrm{NF}\times(\mathrm{BR})^2}\,\mathrm{SNR}_{\mathrm{in}}\right)$$

. (4.57)

4.11 Discussion

We have presented an image reconstruction technique for dynamic electrical impedance tomography based on a *maximum a posteriori* regularization approach, and

have developed several figures of merit to evaluate its performance. This approach allows a theoretical interpretation of the image reconstruction algorithm which takes into account in a natural way the various *a priori* sources of information that we have: the noise magnitude in the measurement electronics, and the maximum spatial resolution attainable using a given number of electrodes. From a practical perspective, this information can be taken into account by pre-calculating a reconstruction matrix, so that subsequent imaging requires only a matrix multiplication and can be accomplished in real-time.

This approach has an adjustable regularization parameter which controls the trade-off between the noise performance and the resolution of the imaging. In order to compare different algorithms, we developed the noise figure as a parameter to measure the noise performance, so that two algorithms with equal NFs can be meaningfully compared in terms of resolution and imaging bias. Using this comparison, we demonstrated that the algorithm presented here, compared to previously proposed algorithms, achieves the best resolution while avoiding introducing significant bias (not "pushing" reconstructed contrasts toward the centre of the medium).

In order to quantify the significance of the NF, we introduced a communication systems approach to the detection of contrasts under measurement noise. Reducing the NF reduces the noise in the reconstructed image and reduces the probability of non-detection of a contrast. In practice, the NF may be selected to ensure a reasonable chance of detecting a physiological event of interest.

While the algorithm presented here performs well under zero mean, white Gaussian noise, a clinical measurement situation is not so simple: electrode contact quality is variable, electrodes move due to patient posture and breathing, and the medium is significantly inhomogeneous, to name just a few difficulties. In order to interpret clinical impedance images, there remains much significant work to be done to understand the behaviour of this algorithm under these conditions.

CHAPTER 5:
IMPEDANCE IMAGING OF LUNG VENTILATION: DO WE NEED TO ACCOUNT FOR CHEST EXPANSION?

Authors:

Andy ADLER

Robert GUARDO

Yves BERTHIAUME

5.1   Abstract

Electrical Impedance Tomography uses surface electrical measurements to image changes in the conductivity distribution within a medium. When used to measure lung ventilation, however, measurements depend both on conductivity changes in the thorax and on rib cage movement. Given that currently available reconstruction techniques assume that only conductivity changes are present, certain errors are introduced. A finite element model is used to calculate the effect of chest expansion on the reconstructed conductivity images. Results indicate that thorax expansion accounts for up to 20 percent of the reconstructed image amplitude, and introduces an artefact in the centre of the image tending to "move" the reconstructed lungs closer together. Although this contribution varies depending on anatomical factors, it is relatively independent of inspiration depth. For certain applications in which one is only interested in changes in the level of physiological activity, the effect of the expansion can be neglected because it varies linearly with impedance changes. We conclude that chest expansion can contribute significantly to the conductivity images of lung ventilation, and should be taken into account in the interpretation of these images.

5.2 Introduction

Electrical Impedance Tomography (EIT) is a medical imaging technique which images the conductivity distribution in a medium from electrical measurements resulting from low frequency current injection at electrodes on the skin. One of the promising applications of EIT is in cardio-pulmonary monitoring of intensive care patients. The phenomena of interest, lung ventilation, lung perfusion, cardiac output, and lung fluid content, induce conductivity changes large enough to be measured by EIT. The principal advantages of EIT in a monitoring environment are that it is non-invasive and minimally cumbersome, and potentially inexpensive enough to allow a system to be dedicated to each patient.

For example, our tomographic system (Guardo, 1991) uses 16 EKG style electrodes surrounding the patient's thorax, with a thin co-axial cable connecting each electrode to the tomograph. Because this configuration is not bulky or intrusive, and current injection is significantly below the threshold of cutaneous perception, it should not cause discomfort to a patient during prolonged monitoring.

Several difficulties have been identified with EIT, the most important being the low spatial resolution, on the order of 10% of the medium diameter using 16 electrodes. This resolution is far too low for anatomical imaging, but may be of interest for functional imaging of physiological processes. The application with which we are concerned in this paper, imaging of lung ventilation, is easily within the capacities of EIT.

The other major problem is the low sensitivity: the largest physiologically realisable conductivity changes cause a 10% variation in the voltages measured, and most events produce far less signal than this. It is generally recognised that EIT measurement hardware must have a precision of 0.1% (Guardo, 1991). Combined with this low sensitivity to conductivity change, EIT has many sources of error in measurements, especially due to electrode positioning and contact resistance, which are affected by patient movement, posture, and skin perspiration.

All imaging algorithms which have been proposed for EIT reconstruct the conductivity distribution assuming the electrical measurements depend uniquely on the conductivity (for example see Webster (1992)). Respiratory activity, however, causes a

movement of the chest by as much as 10 percent of the anterior-posterior dimension. In this paper the effect of this movement on the EIT measurements and on the reconstructed conductivity distribution is described, using a numerical model of the mechanical and electrical properties of the thorax.

5.3   Image Reconstruction

Two image reconstruction approaches have been proposed for EIT: static and dynamic imaging. Static imaging involves reconstructing the absolute conductivity distribution from the voltage measurements, whereas dynamic imaging reconstructs the change in the conductivity distribution. In general, static reconstruction algorithms suffer from a high sensitivity to measurement error (Barber, 1988), due to EIT being more sensitive to changes near the medium surface than it is to changes within the medium. In this paper we consider dynamic imaging, which, while less general than static imaging, is more robust. Images are reconstructed of the change in logarithm conductivity distribution between two sets of measurements, $\mathbf{v}^1$ and $\mathbf{v}^2$, taken at times t^1 and t^2 respectively. Our regularized linear reconstruction algorithm (Adler, 1995) defines the dynamic signal vector, $\mathbf{z}$, as

$$\mathbf{z}_i = \frac{\mathbf{v}_i^1 - \mathbf{v}_i^2}{\frac{1}{2}\left(\mathbf{v}_i^1 + \mathbf{v}_i^2\right)}$$

(5.1)

Each component, i, of the signal represents a different pattern of current injection and voltage measurement. Using this signal, the vector of image elements, $\mathbf{x}$, is estimated, using the regularised image reconstruction formulation

$$\mathbf{x} = \left(\mathbf{H}^t \mathbf{W} \mathbf{H} + \mu \mathbf{Q}\right)^{-1} \mathbf{H}^t \mathbf{W} \mathbf{z} = \mathbf{B} \mathbf{z}$$

(5.2)

This algorithm calculates a single reconstruction matrix $\mathbf{B}$ which takes into account various properties of the tomographic system in the parameters $\mathbf{H}$, $\mathbf{W}$, $\mathbf{Q}$, and μ. $\mathbf{W}$ is a diagonal matrix of the reciprocal noise variances in each signal element; its value can be calculated from the definition of the signal or measured from the tomographic system. $\mathbf{H}$ is a sensitivity matrix defined by

$$\mathbf{H}_{ij} = \frac{\partial [\mathbf{Z}(\mathbf{x})]_i}{\partial \mathbf{x}_j}\bigg|_{\mathbf{x}=\mathbf{x}_O}$$

(5.3)

where $\mathbf{Z}(\mathbf{x})$ is a finite element model of the measured dynamic signal, $\mathbf{z}$, due to a conductivity change $\mathbf{x}$, and $\mathbf{x}_O$ represents the background conductivity distribution. $\mathbf{H}$ has dimensions of the number of conductivity elements by the number of signal components. Since, in general, we do not have anatomical information from which the background conductivity distribution can be calculated, it is assumed to be homogeneous.

In order to avoid introducing artefacts by covering the medium too coarsely, the number of independently varying conductivity elements must allow a spatial resolution of at least 10% of the medium diameter. Using 16 electrodes does not provide enough independent measurements to estimate each conductivity element, and some form of *a priori* information must be introduced. $\mathbf{Q}$ is a regularization matrix which penalises high spatial frequency components in the reconstructed image. We penalise all image components of spatial frequency 10% diameter and higher because the quantity of independent measurements available with the electrode configuration used does not permit resolving detail at this level. The parameter controls the amount of regularization used, and has a strong influence on the performance of the image reconstruction. A low value tends to produce the highest resolution images but at the same time amplify noise in the measurements, while a high value reduces the image resolution for an improved noise performance. We determine μ in order to control the amplification of noise in the reconstructed image. Using a communications systems model, we consider the reconstruction matrix to be a signal receiver: at the input there is a signal $\mathbf{z}$ and noise $\mathbf{n}$ producing the output signal $\mathbf{Bz}$ with noise $\mathbf{Bn}$, and define the noise figure (NF) as the ratio of the input to output signal to noise ratio (SNR). This NF depends only on the reconstruction matrix and is a function of μ.

$$NF = \frac{SNR_{in}}{SNR_{out}} = \left(\frac{mean[\mathbf{z}]}{\sqrt{var[\mathbf{n}]}}\right)\bigg/\left(\frac{mean[\mathbf{Bz}]}{\sqrt{var[\mathbf{Bn}]}}\right)$$

(5.4)

All images reconstructed in this paper use a NF of 1. In our imaging system, the value of $\mathbf{B}$ is calculated off-line for the measurement configuration and geometry, and calculate only the matrix multiplication during the imaging. In this paper the images

reconstruct the conductivity at 256 triangular elements; this image reconstruction takes 0.10 s on our SUN SPARC 10/30 computer system.

In order to determine whether the results of our simulations are a function of the reconstruction algorithm, or are generally applicable to EIT imaging, images were also reconstructed using the equipotential backprojection technique of Barber et al. (Barber, 1987). The ratio of image magnitude produced due to expansion and due to conductivity change using backprojection was within 5 percent of the value calculated using the algorithm presented here. Since backprojection tends to "push" reconstructed contrasts towards the centre of the medium (Adler, 1995) artefacts due to electrode movement tend to be moved into the area of the lung images, and it is important to carefully select a region of interest that does not include these artefacts.

5.4   Dynamic Imaging

Dynamic imaging is able to significantly reduce errors due to unknowns in electrode position and medium geometry. In order to demonstrate this effect, we simulate the finite element geometries shown in figure 5.1. Figures 5.1A and 5.1B show a circular model with evenly spaced electrodes, indicated by arrows. This is the same model used to reconstruct the conductivity images in figure 5.2, and there is thus no geometrical error. Figures 5.1C and 5.1D show a medium with 10% rms position error on the medium geometry and the electrode configuration. Figures 5.1B and 5.1D contain two conductive contrasts spaced by 1/3 the diameter half way toward the top of the medium, while 5.1A and 5.1C are homogeneous. Figure 5.2 shows a wire frame plot of images reconstructed from these measurements. Figure 5.2A is the dynamic image due to the change in measurements from 5.1A to 5.1B, i.e. the image due to no geometrical error, figure 5.2B images A-D with error in one measurement set and not the other, and figure 5.2C images C-D with geometrical error in both measurements. The results show that while the artefacts due to position error make 5.2B unrecognisable, 5.2C is almost of the same quality as 5.2A, except for a bias introduced into the positions and shapes of the contrasts.
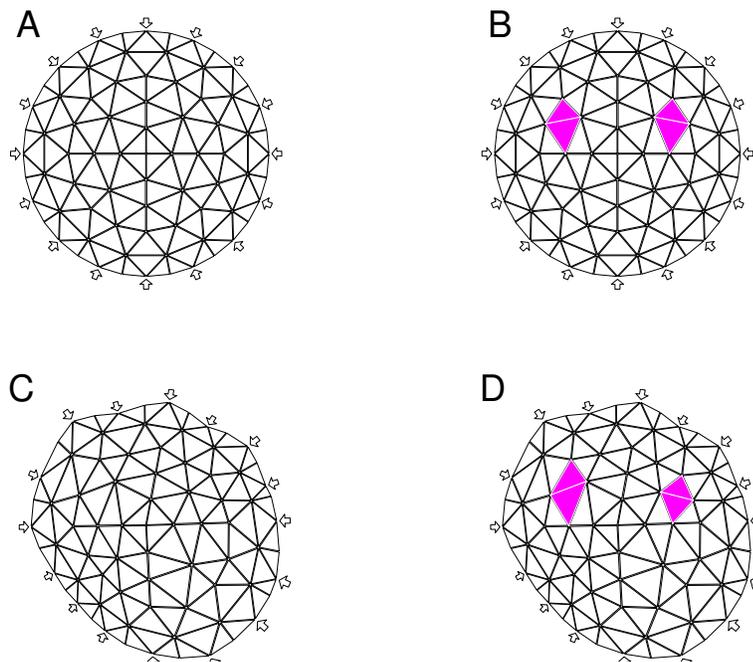
Figure 5.1: A measurement configuration with geometrical and electrode placement error
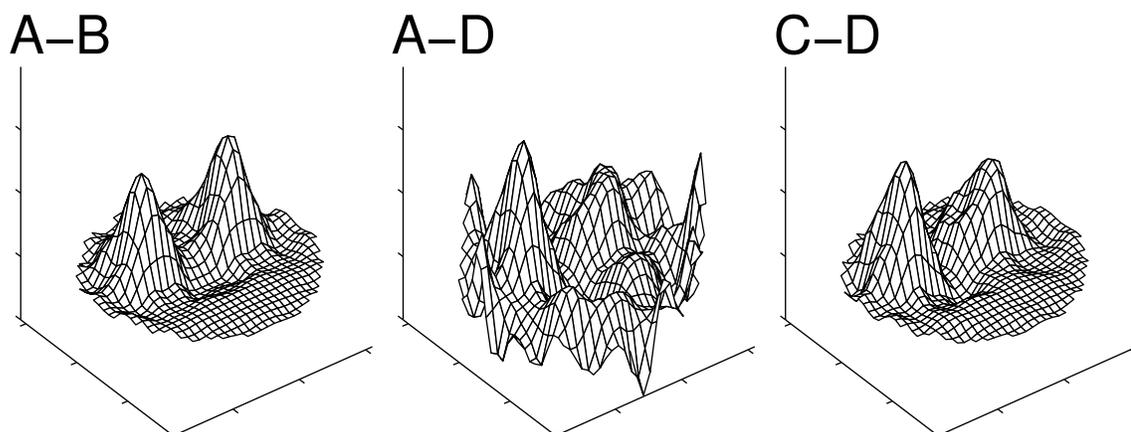
Figure 5.2: Images from media with geometrical errors.
A: Measurements A-B
B: Measurements A-D
C: Measurements C-D

Dynamic imaging is thus able to significantly reduce the effect of geometrical unknowns on image reconstruction as long as these perturbations stay constant over time. Additionally, dynamic imaging can deal with variability in the contact resistance and area

of electrodes, and differences in gains between channels of the measurement hardware. These physical constants are, in general, very difficult to control with sufficient accuracy. Iterative approaches to static image reconstruction (Woo, 1993; Yorkey, 1987) compare the measurements from the medium to those produced by the FEM and calculate the conductivity distribution necessary to best simulate these measurements. In the sense that iterative algorithms compare measured data containing geometrical errors to simulations on known geometries, they are subject to the imaging difficulties incurred in figure 5.2B.

5.5   Lung Ventilation and Electrode Movement
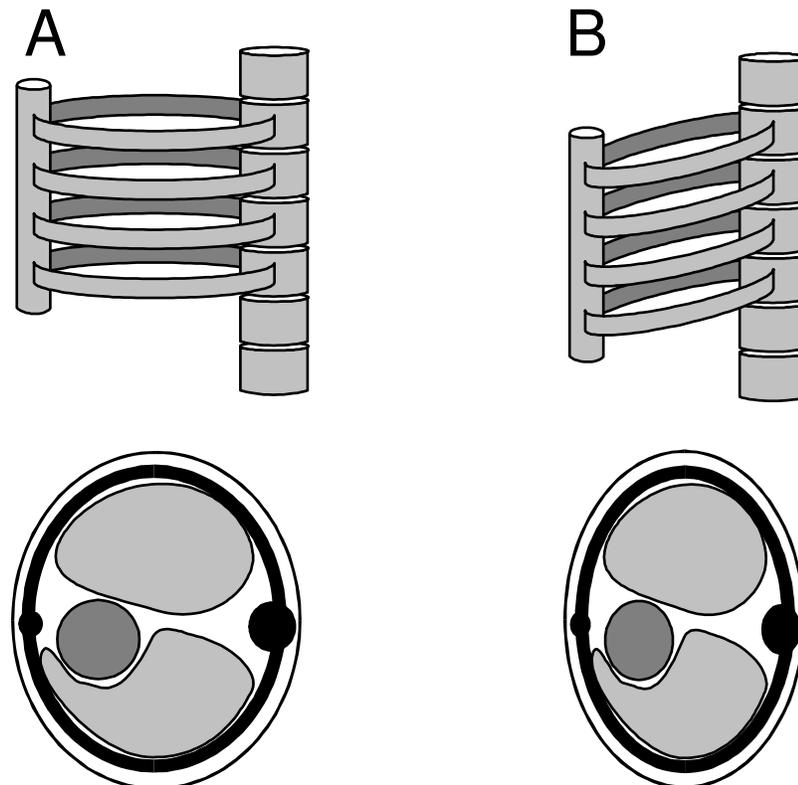
Figure 5.3:   Schematic diagram of rib cage movement during breathing.
A: Rib Cage at end-inspiration
B: Rib Cage at end-expiration

Respiratory activity involves a rhythmic movement of the rib cage by as much as 10 percent of the anterior-posterior dimension (Detroyer, 1985). This results in a movement of the electrodes, which violates the assumption of constant geometry of

dynamic imaging, and tends to introduce artefacts into the reconstructed images which need to be taken into account in image interpretation.

The three dimensional movement of the rib cage is complicated. Inspiration results from a combination of a contraction of the diaphragm, tending to vertically elongate the lungs, and an opening of the rib cage, tending to increase the lung cross sectional area. The increasing lung volume decreases pressure, and, if the airway is open, causes inspiration. This is schematically illustrated in figure 5.3. The movement in the upper chest can be approximated as an up-down movement of the sternum and the anterior portion of the ribs while the posterior portion of the ribs remains fixed at the spine. The relative contribution to the tidal volume from chest expansion and diaphragm movement can vary significantly, as a function of posture, tidal volume, and voluntary activity.
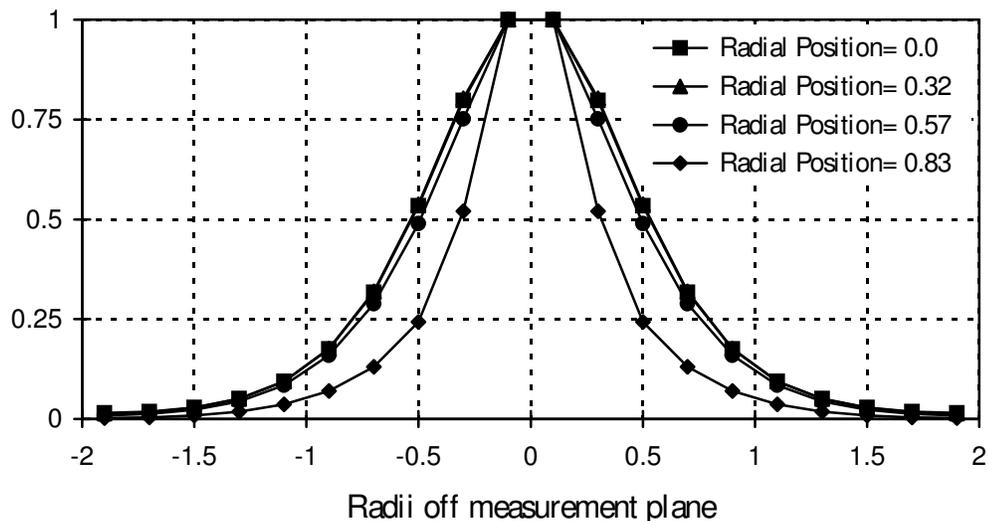
Figure 5.4: Normalised EIT sensitivity to off plane conductivity changes vs. radii of measurement plane

Figure 5.4 shows the sensitivity of EIT to conductivity changes off the plane of measurement, measured in radii of the medium. These results are simulated on a cylindrical medium for objects at four different radial positions, and the sum of all pixels in the reconstructed image is normalized with respect to the maximum value. Images were also reconstructed using the filtered backprojection technique, yielding substantially

similar results. A three dimensional FEM with an electrode diameter of 5 percent of the medium diameter was used for these simulations. The vertical sensitivity is relativity constant as a function of radial position, except close to the boundary where objects off the measurement plane are less visible, and is not strongly dependent on electrode size when electrodes are smaller than the vertical sensitivity. If a series of electrodes are placed in a plane around a cylindrical medium, the contribution to the measurements from contrasts off the electrode plane will be significant up to approximately one radius above or below the measurement plane, at which point its contribution to the EIT measurements is reduced to 13 percent of that of contrasts in the measurement plane. Since the lungs extend significantly above and below the electrode plane, vertical elongation of the lungs due to contraction of the diaphragm will have a much less significant effect on EIT than other factors. In this paper, only the effect of electrode movement due to chest expansion is modelled because this phenomenon should have the largest effect on impedance measurements.

This movement is modelled in two dimensions as a forward displacement of the rib cage by an amount proportional to the distance anterior of the centre of the thorax. The lateral movement of the rib cage can vary between individuals from almost zero to as large as the movement in the anterior-posterior (AP) dimension. The parameter L represents the ratio of the lateral to AP displacement. Given a movement fraction of M of the AP dimension, *APD*, a point (x,y) on the rib cage has a displacement

$$\vec{d} = M \cdot \left[(y - y_c)\bar{y} + L\frac{AP}{LD}(x - x_c)\bar{x} \right]$$

(5.5)

where *LD* is the lateral dimension, (x_c, y_c) are the co-ordinates of the centre of the thorax, and $\bar{x}$ and $\bar{y}$ are unit vectors in the lateral and AP directions, respectively. Thus for a movement fraction $M = 0.1$, for a thorax of 20 cm AP and 30 cm lateral dimension, with $L=0.5$, then the front (0 , +10 cm) and back (0 , -10 cm) of the thorax will move outward by 1 cm, and the sides ($\pm$15 cm , 0) will move outward by 0.5 cm.

5.6   Finite Element Modelling

We use the finite element method (FEM) to solve for the mechanical and electrical properties of the thorax. Our two dimensional FEM model based on 576 triangular elements is shown in figure 5.5.
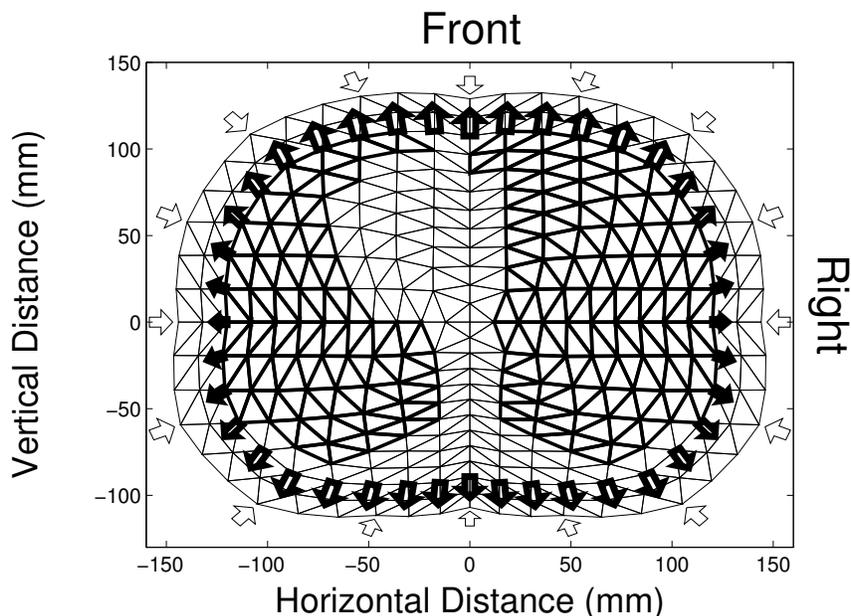
Figure 5.5: Finite element model of the electrical and mechanical properties of the thorax

More elements are used in the simulation of EIT measurements than for the image reconstruction because this allows better representation of anatomical details. The anatomy is based on CT scan data from a normal adult male. Elements drawn with thicker lines form the lungs, the arrows pointing toward the thorax show the location of the electrodes, and the arrows pointing outward show the displacement of the rib cage during inspiration. The medium is divided into three bulk tissue areas corresponding to the lungs, the spinal column and other tissue areas.

Each of these tissues is assumed to be homogeneous and isotropic in its electrical and mechanical properties. Thus, each tissue can be characterised by four properties: the modulus of elasticity, E, Poisson's ratio, υ, and the conductivity, σ, at expiration and inspiration. There is a certain amount of disagreement on the mechanical and electrical

properties of tissues in the literature. The values used in this study (Lai-Fook, 1976; Parker, 1990) are shown in table 5.1.

Table 5.1: Mechanical and electrical tissue properties used in this paper.

Tissue	Modulus of Elasticity (E)	Poisson's Ratio (υ)	Conductivity (σ) Expiration	Conductivity (σ) Inspiration
Lung	2 kPa	0.47	120 mS/m	60 mS/m
Skeletal Bone	5000 kPa	0.10	10 mS/m	10 mS/m
Other Tissues	20 kPa	0.495	480 mS/m	480 mS/m

Using the finite element method to solve the equations of elasticity, the displacement of all nodes can be calculated as a function of the rib cage displacement, the model geometry, and the elastic properties of each element. A set of EIT measurements for a given thorax geometry and conductivity distribution is simulated using the finite element geometry of the thorax adjusted by the displacement calculated from the mechanical model.

A two dimensional cross section of the thorax is modelled as a isotropic medium consisting of several bulk tissues of different mechanical properties. Since the thorax has significant vertical extent above and below the plane of interest, the vertical deformation is small, allowing the plane strain approximation, which assumes stresses in the z direction are zero. Additionally, since respiration is a relatively slow phenomenon, we neglect dynamic contributions due to the inertia of tissues. The static equilibrium conditions in terms of stress are:

$$\frac{\partial \sigma_x}{\partial x} + \frac{\partial \tau_{xy}}{\partial y} + f_x = 0$$
$$\frac{\partial \tau_{xy}}{\partial x} + \frac{\partial \sigma_y}{\partial y} + f_y = 0$$

(5.6)

where f_x and f_y are the externally applied body forces in the x and y directions, and σ and τ represent the stresses defined by

$$\begin{bmatrix} \sigma_y \\ \sigma_x \\ \tau_{xy} \end{bmatrix} = \begin{bmatrix} c_{11} & c_{12} & 0 \\ c_{12} & c_{22} & 0 \\ 0 & 0 & c_{33} \end{bmatrix} \begin{bmatrix} \varepsilon_x \\ \varepsilon_y \\ \gamma_{xy} \end{bmatrix}$$

(5.7)

where

$$\varepsilon_x = \frac{\partial u}{\partial x},$$

$$\varepsilon_y = \frac{\partial v}{\partial y},$$

$$\gamma_{xy} = \frac{\partial u}{\partial y} + \frac{\partial v}{\partial x}$$

(5.8)

where u and v are the displacements in the x and y directions, respectively. Substituting equations 5.**Error! Bookmark not defined.** and 5.7 into equation 5.6 we obtain the differential form of the plane elasticity equations (Reddy, 1992):

$$\frac{\partial}{\partial x}\left(c_{11}\frac{\partial u}{\partial x} + c_{12}\frac{\partial v}{\partial y}\right) + c_{33}\frac{\partial}{\partial y}\left(\frac{\partial u}{\partial y} + \frac{\partial v}{\partial x}\right) + f_x = 0$$

$$c_{33}\frac{\partial}{\partial x}\left(\frac{\partial u}{\partial y} + \frac{\partial v}{\partial x}\right) + \frac{\partial}{\partial y}\left(c_{12}\frac{\partial u}{\partial x} + c_{22}\frac{\partial v}{\partial y}\right) + f_y = 0$$

(5.9)

In an isotropic medium undergoing plane stress, the elasticity constants may be written in terms of the modulus of elasticity E and the Poisson's ratio υ of the material

$$c_{11} = c_{22} = \frac{E(1-v)}{(1+v)(1-2v)},$$

$$c_{12} = \frac{Ev}{(1+v)(1-2v)},$$

$$c_{33} = \frac{E}{2(1+v)}$$

(5.10)

Using this equation, the FEM is used to calculate the movement of all nodes as a function of the rib cage displacement. Additionally, we ensure that the contact area of the electrodes is not changed by the calculated change in geometry of the medium.

The electrical properties of a two dimensional isotropic medium can be represented by the electrical conductivity $\sigma(x,y,t)$ and relative permittivity $\varepsilon(x,y,t)$. Several tissues, especially muscle tissue, are anisotropic, but we do not consider this in

our model (Brekton, 1992). Current is injected along the medium boundary, which sets up a distribution of voltage and current flow in the medium. Within the medium there is an electrical field $\mathbf{E}(x,y,t)$ which induces a current

$$\mathbf{J} = \sigma\mathbf{E} + \varepsilon\varepsilon_o \frac{\partial \mathbf{E}}{\partial t}$$

(5.11)

where ε_o is the permittivity of free space. For the purposes of this study, we neglect the effect of the permittivity, because we consider it to introduce a perturbation of the results that is less significant than the simplifications of the mechanical problem, such as treating the problem in two dimensions, already made.

At low frequencies, we can approximate $\mathbf{E} = -\nabla V$, and $\nabla \cdot \mathbf{J} = 0$, giving

$$\nabla \cdot (\sigma\nabla V) = 0$$

(5.12)

The boundary conditions to this equation are determined by the distribution of current injection into the medium, and the requirement that the voltage be fixed at a reference point.

The FEM is used to solve this equation to calculate the EIT voltages measured at the electrodes for each rib cage expansion level and conductivity distribution.

5.7   Results

Using this model, the EIT measurements in table 5.2 were simulated, for a lateral to AP rib cage movement ratio, L, of 0.5 and a movement fraction, M, of 10 percent. In order to study the effect of expansion for a homogeneous medium, measurements were simulated for a condition where all tissue properties were set to those given for "other tissues" in table 1.

Table 5.2: EIT measurements conditions simulated

Measurement	Conductivity Condition	Expansion Condition
$\mathbf{V}_0$	Expiration	Expiration

V_1	Inspiration	Expiration
V_2	Inspiration	Inspiration
V_3	Homogeneous	Expiration
V_4	Homogeneous	Inspiration

The images reconstructed are shown in figure 5.6; each conductivity distribution is shown as a wire frame on the left side, where the vertical axis represents the negative logarithm conductivity, and as a grey scale plot on the right, where darker regions correspond to decreased conductivity. Each grey scale plot is normalised individually. Figure 5.6A images the change in conductivity distribution associated with inspiration due to both conductivity change and chest expansion, V_2-V_0; this corresponds to what would be actually measured on a patient. If chest expansion did not occur and there were only conductivity changes, this would result in imaging V_1-V_0, shown in figure 5.6B. Similarly, if there was only chest expansion without conductivity change, imaging would give V_2-V_1, shown in figure 5.6C. Figure 5.6D images the conductivity change due to expansion of a homogeneous thorax shaped medium reconstructed from measurements V_4-V_3. For purposes of comparison, we include an image of conductivity change between end-expiration and end-inspiration for a tidal volume of 4 l using thoracic impedance measurements from a normal subject taken using our EIT system, figure 5.6E.

The simulated images in both figures 5.6A and 5.6B are qualitatively similar to those produced experimentally except that the distribution of the lung images covers the thorax more uniformly than in the experimental image. The effect of the chest expansion is to add a large, low amplitude artefact in the centre of the thorax, which "moves" the reconstructed lung regions closer to the centre. The image produced by expansion of a homogeneous medium, 5.6D, has more than four times less contrast than the thorax expansion image, 5.6C. This can be explained by the fact that most of the space made available in the thorax by expansion is filled by the lungs which increases the area filled with low conductivity tissue.
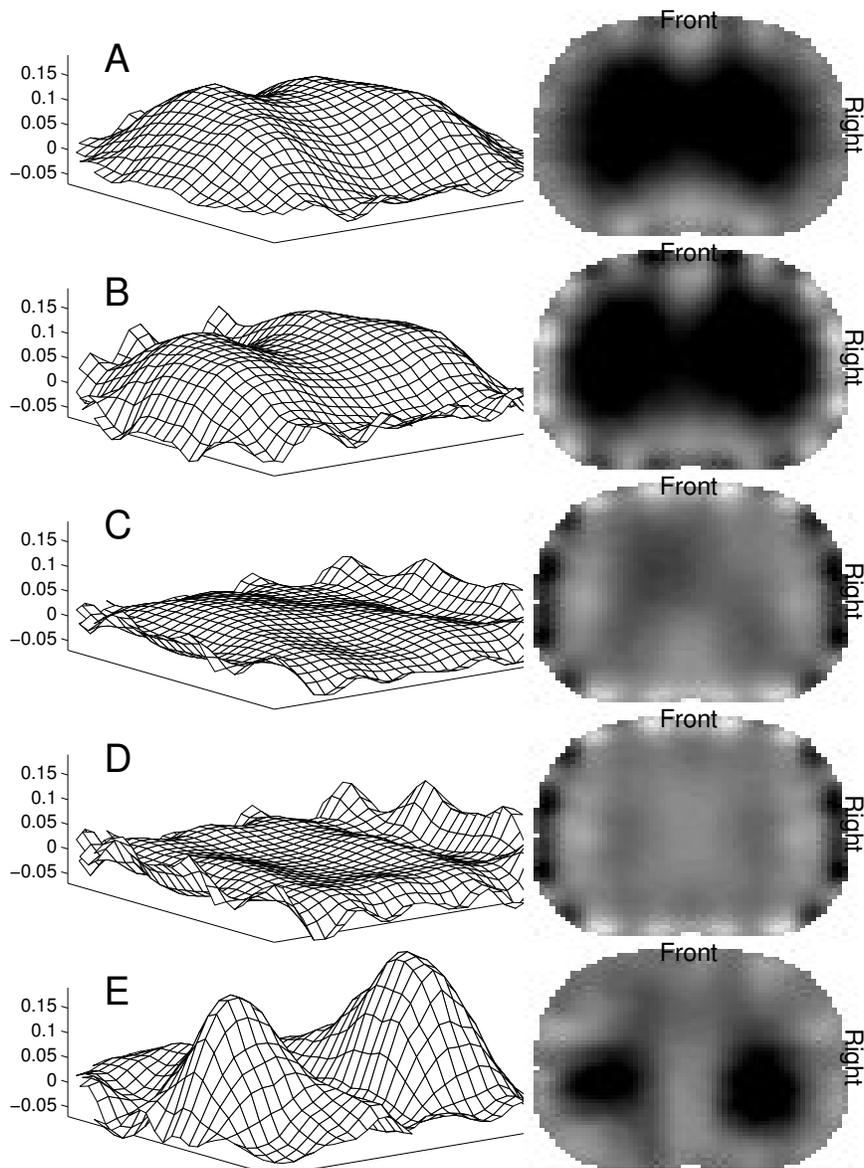
Figure 5.6: Images of conductivity change in the thorax.
A: Simulated expansion and conductivity change.
B: Simulated conductivity change only.
C: Simulated expansion only.
D: Simulated expansion for a homogeneous medium.
E: Measured data for tidal volume of 4 *l*.

In order to quantitatively compare the contribution of each component of the images, we define the image magnitude as the sum of the pixels in a region of interest (ROI) of the reconstructed image. The ROI chosen includes all the pixels except those

within 5 percent of the medium diameter of the boundary. This choice of ROI allows exclusion of the artefacts produced at the electrodes.

Figure 5.7 shows the normalized image magnitude as a function of the percent thorax expansion due to conductivity change and due to expansion for various values of the lateral to AP expansion ratio, L. In calculating these values, the conductivity was assumed to vary linearly between its maximum and minimum values as a function of expansion depth. In order to illustrate the percentage contribution of the two effects, figure 5.8 shows the ratio of expansion image magnitude to that of conductivity change as a function of percent thorax expansion. The contribution stays reasonably constant with respect to expansion, but varies considerably as a function of L, from an average value of 18% at $L = 1.0$ to 2.5% at $L = 0.0$.
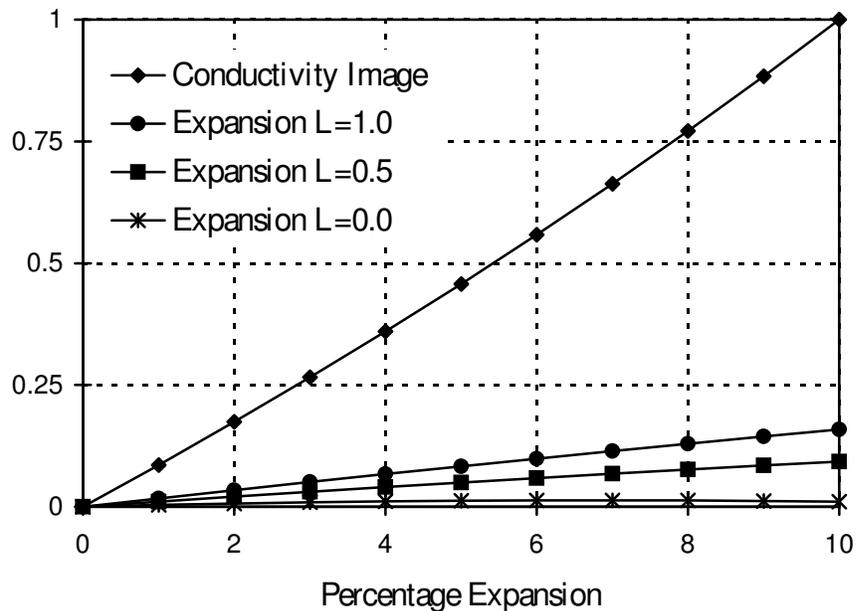
Figure 5.7: Normalized Image magnitude vs. percent thorax expansion
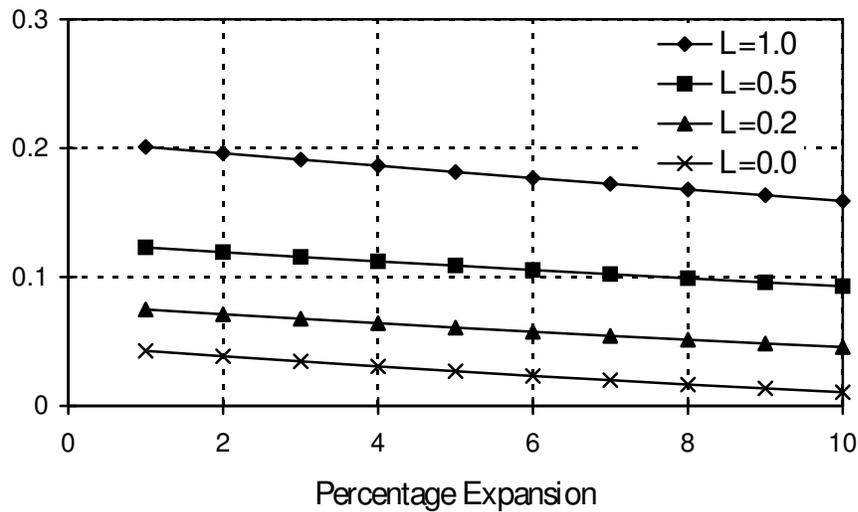
Figure 5.8: Ratio of expansion image magnitude to conductivity change image magnitude vs. percent thorax expansion

These results depend somewhat on the values of the mechanical parameters. In order to determine the sensitivity to these values, simulations were performed for a range of values of modulus of elasticity and Poisson's ratio for a thorax with $L = 0.5$ and one percent thorax expansion. The ratio of image magnitude due to expansion to that due to conductivity change is presented in table 5.3. The ratio remains relatively constant except where the simulated lung modulus or Poisson's ratio equals or exceeds that for other tissue. Variations of the mechanical properties of skeletal bone produced changes of less than 3 percent to the expansion to conductivity change ratio.

Table 5.3: Ratio of expansion image magnitude to conductivity change image magnitude for various mechanical parameters.

Expansion to conductivity change ratio	Modulus of elasticity (kPa) Lung	Modulus of elasticity (kPa) Other tissue	Poisson's ratio Lung	Poisson's ratio Other tissue
0.1195	2.0	20	0.47	0.495
0.1133	2.0	20	0.40	0.480
0.0695	2.0	20	0.49	0.480
0.1277	2.0	20	0.40	0.498

0.1184	2.0	20	0.49	0.498
0.1222	0.5	5	0.47	0.495
0.0893	4.0	5	0.47	0.495
0.1315	0.5	40	0.47	0.495
0.1222	4.0	40	0.47	0.495

5.8   Discussion

This paper presents an estimate of the magnitude of the artefact introduced into EIT images of pulmonary activity due to thorax surface electrode movement. We have considered only the contribution from rib expansion in a two dimensional cross section, as this effect is the most important cause of electrode movement. In order to completely characterise this problem, it will be necessary to use a much more detailed three dimensional anatomical model. Our model, however, allows us to make several conclusions.

• The expansion of the thorax contributes constructively to the measured change in conductivity. The perturbation introduced into EIT images by the expansion is a broad zone in the centre of the image accounting for from 2% to 20% of the image magnitude. The amplitude of this perturbation varies significantly with changes in the lateral to AP expansion ratio, and is affected by other anatomical differences also.

• The percentage contribution to the total image due to conductivity change and expansion remains relatively constant with increasing rib cage movement, varying by up to 3% of the total image. This effect indicates that image interpretation based on a reference level of physiological activity will largely eliminate the effect. For instance, if a given image is known to correspond to 400 m*l* tidal volume in a patient, then 800 m*l* tidal volume should produce twice the image amplitude, and the relative contributions of expansion and conductivity change can be ignored.

CHAPTER 6:
EXPERIMENTAL EVALUATION OF ELECTRICAL IMPEDANCE TOMOGRAPHY FOR MONITORING PULMONARY FUNCTION

6.1   Introduction

Many physiological processes of interest to studies of pulmonary function induce changes in tissue conductivity: heart and lung activity move air and blood and pulmonary edema introduces extravascular fluid, all of which contrast with the conductivity of thoracic tissue.   In the past, thoracic impedance has been proposed as a tool for monitoring pulmonary function *in vivo*; however, because of large variations in the normal values it was not considered a reliable technique.

Electrical Impedance Tomography is evaluated as a technique to measure several physiological phenomena of interest to pulmonary function while avoiding the problems associated with transthoracic impedance. Images of the change in conductivity between two sets of measurements taken at different times are reconstructed using the regularized linear reconstruction algorithm presented in chapter 4 with a noise figure parameter of 0.5. These images allow the effects of different physiological activities within the thorax to be separated by the different locations of the conductivity changes in the thorax image. Variations due to changes in electrode contact quality and skin resistance are typically seen at the outer edge of images and can be eliminated from the image interpretation by selection of an appropriate region of interest.   EIT also permits a relatively easy calibration so that measurements can be interpreted in terms of millilitres of volume change with an associated estimate of measurement error (Trudelle, 1995). Additionally, EIT is non-invasive, potentially quite inexpensive and minimally cumbersome, requiring only the connection of several electrodes and wires to the patient.

In this chapter the ability of EIT to determine quantities of physiological interest is studied. The following capabilities of EIT are verified:

• **Quantitative determination of physiological activity levels:** EIT measures the change in conductivity distribution from which it should theoretically be possible to quantitatively estimate a physiological function which modifies the conductivity distribution. This is experimentally verified by imaging different levels of lung ventilation and fluid instillation into a lung. Measurement of ventilation is verified by comparison to the ventilator tidal volume while instillation is verified by comparison to the fluid quantities instilled.

• **Rejection of extraneous physiological activities:** The Thoracic Impedance technique is considered to be unreliable because of its inability to reject physiological activities other than the one under investigation (Fein, 1979). EIT accomplishes this rejection by careful control of data acquisition and selection of an appropriate region of interest in the reconstructed image. This capability is experimentally validated in this study because measurement of ventilation requires rejection of cardiac activity and measurement of instillation requires rejection of both cardiac activity and lung ventilation.

• **Cross-sectional image production:** The advantage of EIT over currently used technologies for monitoring lung function is the ability to produce an image of conductivity change from which heterogeneities in lung function can be determined. This capacity is validated by verifying whether the lung subject to fluid instillation can be determined from the EIT images.

• **Monitoring:** An advantage of EIT over currently used medical imaging technologies is the ability to monitor physiological function over time. This capacity is verified by acquiring data during the reabsorbtion phase of the lung fluid and comparing the residual fluid quantity predicted by EIT to the value determined from the extracted lungs.

6.2   Methods

A block diagram of an EIT system is shown in figure 6.1. A series of ECG style electrodes are connected around the subject's thorax. The exact positioning of the electrodes is not critical, but it is important that they do not move during the monitoring.

These electrodes are connected to our EIT data acquisition controller (Guardo, 1991), from which data is sent to a computer which calculates the thorax image.
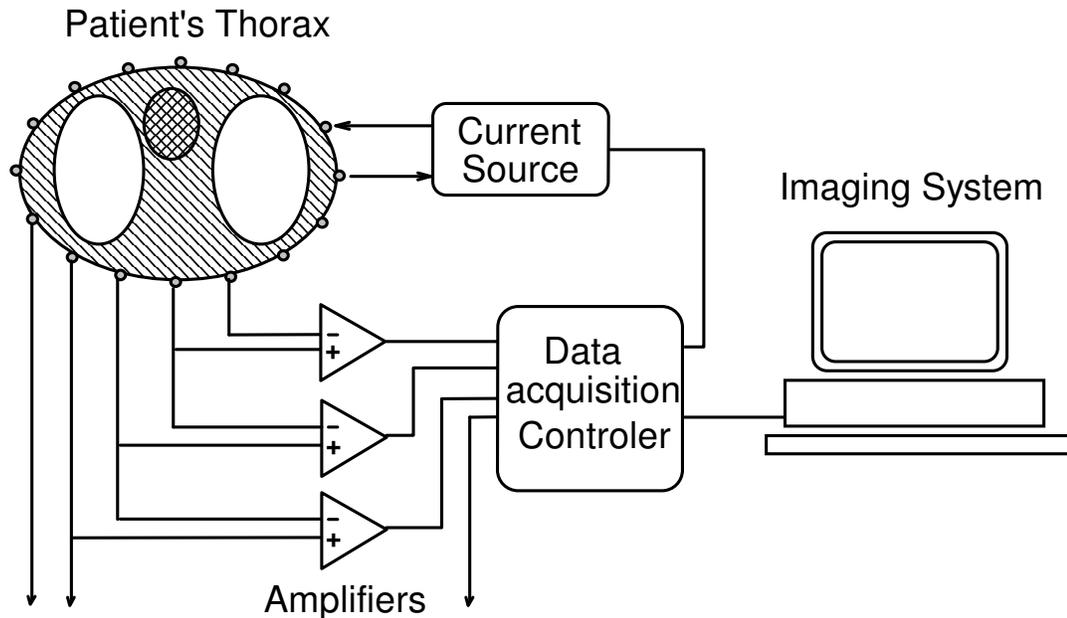
Patient's Thorax

Figure 6.1: Block Diagram of our EIT system.

Images are calculated of the change in the conductivity distribution in the patient's thorax between the taking of any two data sets. This imaging approach is called dynamic EIT, to distinguish it from static EIT, which aims at reconstructing the conductivity distribution from one data set. Dynamic imaging is significantly more robust because it is able to better compensate for measurement errors, variation in electrode positioning and is more sensitive to small conductivity changes (Adler, 1995).
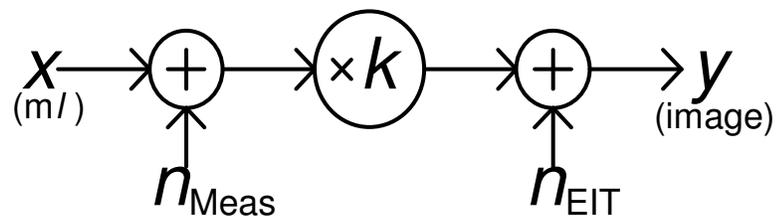
Figure 6.2: Model of EIT image formation and noise

The model of figure 6.2 describes the interpretation of an image contrast in a region of interest produced by a change in conductivity. For example, an amount of fluid (x ml) of known conductivity is introduced into a lung, and an EIT image is reconstructed of the conductivity change produced from which a sum of image pixels (y) in the region

of interest (ROI) is calculated. We would like to be able to calculate the volume of fluid and estimate the error in this calculation.

Two sources of error are modelled, an error of measurement of the fluid when it was introduced (n_{Meas}) and an error due to the electronic and imaging system (n_{EIT}). Additionally, there is a conversion factor, k, between volume and image contrast. The parameter k depends on the conductivity of the fluid, and its position relative to the plane of the electrodes. Trudelle (1995) has shown that n_{EIT} is a constant of the EIT system, and that this linear relationship is valid within 10 percent up to an instillation region covering 25 percent of the thorax diameter. Thus, after calculating y from the EIT image the fluid volume is calculated from

$$x = \frac{y}{k}$$

(6.1)

The standard deviation of the error in this calculation of the fluid volume is expressed by σ_x, which we define as the EIT measurement error and use as the figure of merit for the measurement of a physiological process.

The parameter k can be calculated numerically in situations where the geometry and anatomy can be accurately modelled. However, this is not the case in this study, and the values of k and σ_x are estimated from the experimental data using the following statistical calculations.

Given N experiments introducing quantities of fluid x_i producing EIT image pixel sum y_i ($1 \leq i \leq N$), k is defined to be the value which minimises

$$\sum_{i=1}^{N}(y_i - kx_i)^2$$

(6.2)

Thus k is given by

$$k = \left(\sum_{i=1}^{N} y_i x_i\right) \bigg/ \left(\sum_{i=1}^{N} x_i^2\right)$$

(6.3)

The EIT measurement error is the standard deviation in estimating the fluid quantity x from the EIT image, y, and is calculated by

$$\sigma_x = \sqrt{\frac{1}{N-1}\sum_{i=1}^{N}\left(\frac{y_i}{k} - x_i\right)^2}$$

(6.4)

The ROI used for the calculation of y includes all the thorax area except the 20 percent of the area closest to the surface. This choice ensures that the lung area is included while image artefacts on the surface due to electrode movement are excluded. The value of k calculated by this model is valid for a particular electrode placement geometry and anatomy and for a given fluid conductivity. Calibration of this parameter for various measurement configurations in a cylindrical saline filled thorax model is described by Trudelle et al. (1995).

During the reabsorbtion phase, the fluid content is modelled to decrease linearly with time at a rate of r ml/min, expressed by the model

$$\frac{y_t}{k} = x_o - rt$$

(6.5)

where t is the time in minutes after maximum instillation, x_o is the fluid volume at maximum instillation, and y_t is the ROI pixel sum in the EIT image at time t. The linear model used here is not ideal; the work of Mathay (1985) and Berthiaume (1988) shows that reabsorbtion in dog and sheep lungs can best be modelled using an exponential function. The experimental data, however, represents a relatively short period compared to the time required for complete reabsorbtion, during which the difference between an exponential and linear model is small. From a calculation of r, the expected error, σ_r, associated with the measurement of the fluid quantity during the reabsorbtion phase can be expressed by

$$\sigma_r = \sqrt{\frac{1}{N-1}\sum_{i=1}^{N}\left(\frac{y_r}{k} - x_o - rt\right)^2}$$

(6.6)

Two choices of the ROI are shown in figure 6.3: the instillation region, R_i, which corresponds to the half of the thorax which contains the lung undergoing instillation; and the control region, R_c, which corresponds to the opposite half. Two additional regions are defined: a whole thorax region, R_t, combining the pixel sum in both sides, and a difference region R_d, corresponding to the difference in pixel sum between R_i and R_c.

ROI for control lung
R_c

ROI for instilled lung
R_i

Instilled lung region
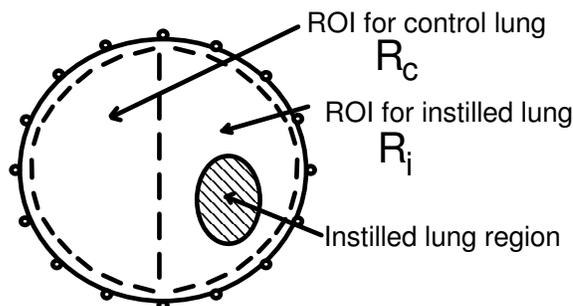
Figure 6.3: Choice of Region of Interest

EIT is most sensitive to conductivity changes in the plane of the electrodes (refered to as the measurement plane), but since the pattern of electrical current flow covers the volume between the electrodes, it does respond to changes which occur above and below this plane. The sensitivity drops to 50 percent at one half of the medium radius off plane. For example, for a subject with an anterior-posterior dimension of 20 cm, EIT will be most sensitive to conductivity changes within 5 cm above and below the measurement plane. Using a configuration of 16 electrodes does not provide enough information to allow EIT to produce a high resolution image; structures close to each other tend to be blurred together in the image. The measurement configuration and image reconstruction algorithm used allow contrasts separated by more than one quarter of the radius to be distinguished. The reconstructed position of a conductivity change is accurate to within 5 percent as long as the change is 10 percent of the diameter from the electrodes. Reconstructed positions of conductivity changes close to the electrodes tend to get "pushed" toward the centre of the medium.

When positioning the electrodes, it is not necessary to ensure that the spacing between all electrode pairs is exactly the same, as long as the electrodes do not move between the acquisition of the data sets to be compared (Section 4.4). Computer simulations indicate that electrode positioning variability of 1 cm on a thorax of diameter 20 cm produces no substantial change to the images produced.

6.3   Experimental Protocol

Ten large dogs (32.6 ± 6.3 kg) were anesthetized and paralysed. After tracheotomy, animals were mechanically ventilated in a prone position. In order to assess hemodynamic stability, heart rate, blood gas concentrations, and pulmonary arterial and

wedge pressures were monitored. 16 ECG style electrodes spaced evenly around the thorax 10 cm above the base of the rib cage, and 3 electrodes for measurement of cardiac activity were attached to each animal. A current of 500 μA at 13 kHz was injected across pairs of adjacent electrodes. EIT data acquisition was begun a minimum of one hour after preparation of the animal. Figure 6.4 shows a ventral view of the prepared animal with the EIT and ECG electrodes connected. The EIT electrodes are connected to the flat cable on the right side of the image.
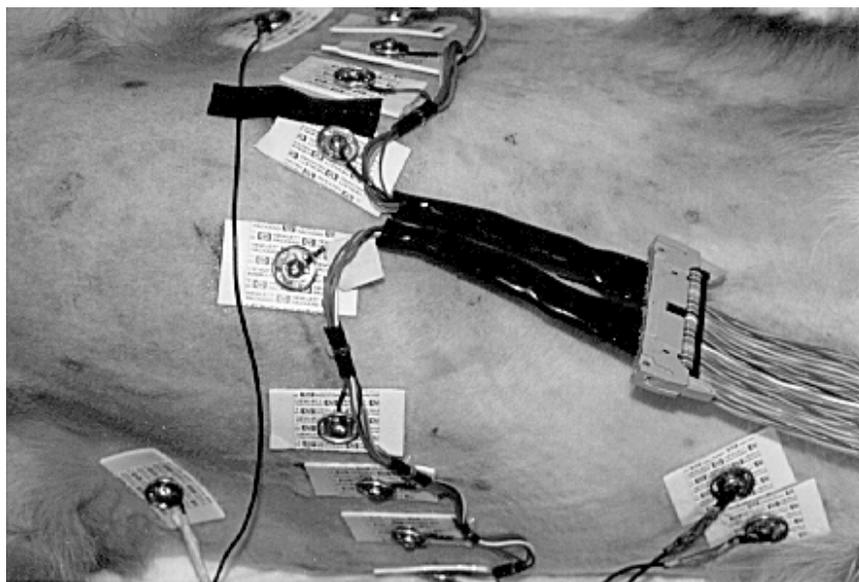
Figure 6.4: Prepared animal with electrodes attached for the ECG and for EIT data collection.

The data acquisition triggering protocol is shown in figure 6.5. The EIT system is capable of demodulating the voltage at all electrodes for one injection pattern in 40 ms. In order to reject any contribution from cardiac activity, all data acquisition was triggered 100 ms after the QRS peak. Data for each injection pattern was acquired after subsequent QRS peaks. One data set requires 16 heart beats during which the ventilation to the animal is stopped by clamping the airway tube from the ventilator. The ventilation tube is clamped at end-expiration to fix the lung volume, acquisition is triggered by the QRS peak until all current patterns have been applied, and then the ventilation is allowed to continue. This triggering ensures that the contribution to the conductivity distribution from cardiac and lung activity will be the same for both data sets and will not appear in the image of the change in conductivity. Control of ventilation and starting the EIT acquisition was done by human operators, while the QRS synchronization was performed

under computer control. All EIT data measurements were repeated three times to calibrate for experimental noise.
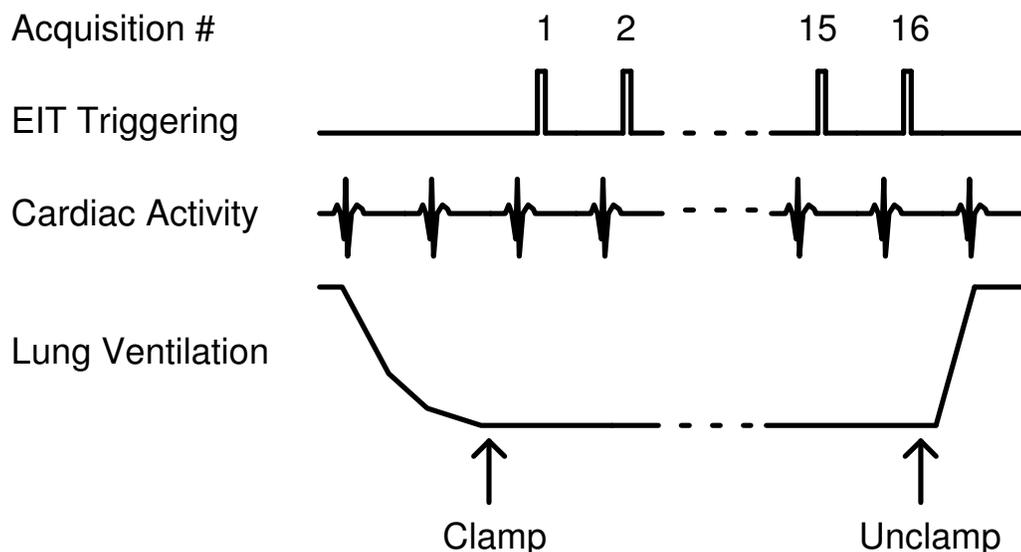
Figure 6.5: triggering schema for cardiac and pulmonary activity

Lung ventilation was measured by imaging the difference between EIT data sets at end expiration and end inspiration. Measurements were taken at ventilator tidal volumes of 200, 500, 700, and 1000 ml except on 3 dogs where all values from 100 ml to 1000 ml in 100 ml increments were taken. After each change of tidal volume, the animal was allowed 5 minutes to stabilise while ventilated at a tidal volume of 500 to 700 ml. All lung ventilation data was acquired before fluid instillation took place.

In order to measure lung fluid content all EIT data was acquired at end-expiration at a constant level of lung ventilation, and images were reconstructed relative to a reference data set taken at end-expiration prior to fluid instillation. Saline solution with added protein (5% Canine Albumin Solution) and a colouring marker (Evans' Blue) was instilled into a lobe of the right lung through a catheter positioned using a bronchoscope. Measurements were taken after successively instilling 10, 25, 50, 75 and 100 ml of fluid, and subsequently measurements were taken approximately every 30 min for the next four hours, to monitor fluid reabsorbtion.

Just prior to sacrificing the animal, a reference set of images were taken to confirm the orientation of the EIT image with respect to the animal. 10 m*l* of saline was injected sub-cutaneously underneath the electrode just left of the centre of the back. The

image reconstructed of this conductivity change allows the orientation of the animal in the images to be confirmed.

After the last data acquisition, the lungs were extracted and the residual fluid content was measured using a gravimetric lung water technique, where the normal lung served as a control to calculate the residual amount of water in the instilled lung. This technique has a coefficient of variation of 10% (Berthiaume, 1987), and is considered to be a standard for lung water measurement. Additionally, the lung into which the fluid was instilled as indicated by the lobe stained with the colouring marker in the solution was verified.

6.4   Results for Ventilation and Instillation

EIT images of ventilation were reconstructed from data sets taken at end inspiration and end expiration at each value of tidal volume, while images of instillation were reconstructed from the difference between the reference and the post instillation data sets. The reference image to confirm the orientation was calculated between end-expiration data sets taken before and after the saline injection. Figure 6.6 shows images of the conductivity changes for the dog in experiment #5. On the left hand side, each image is shown as a wire frame plot where the conductivity change corresponds to the height, and, on the right hand side, as a grey scale image where magnitude of conductivity change is indicated by increasing colour contrast. All wire frame images are shown at the same scale, whereas each grey scale was individually normalized to use the full range of colour contrast.

Figure 6.6A is an image of the change in conductivity due to a tidal volume of 500 m*l*, while figure 6.6B shows the conductivity change due to instillation of 100 m*l* saline in the right lung. Since inspiration of air produces a non-conductive change, and fluid instillation produces a conductive change, the ventilation image is inversed by comparing end-inspiration to end-expiration in order to show both images on the same vertical scale. Figure 6.6C shows the orientation reference image. The EIT images, while of low resolution, show the positions of the lungs, and clearly distinguish the right lung, which underwent instillation, from the control lung. Additionally, the position of the sub-cutaneous saline injection corresponds to the position imaged in figure 6.6C.
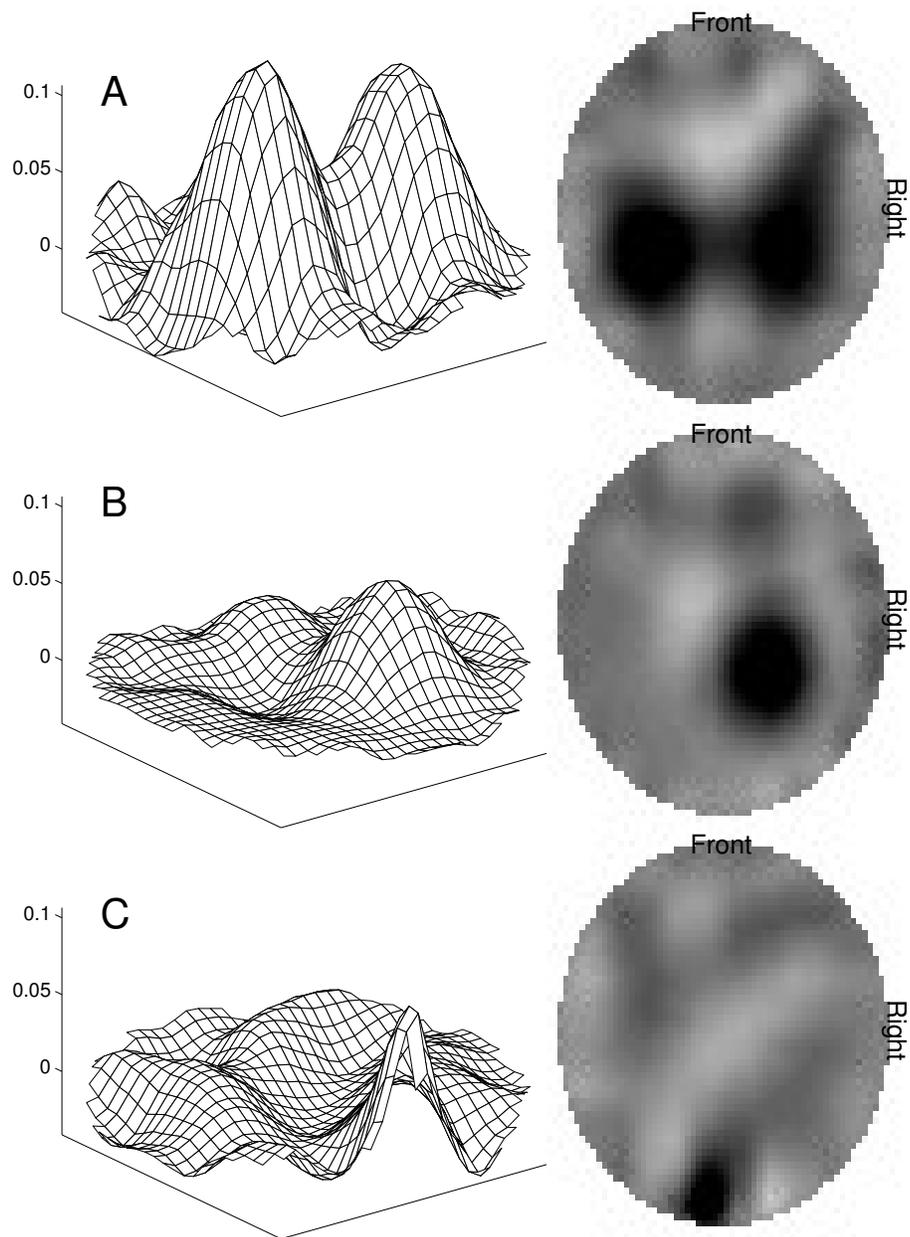
Figure 6.6: Images of the conductivity change in the thorax
        A: Due to 500 m*l* tidal volume
        B: Due to 100 m*l* fluid instillation
        C: Due to injection of 10 m*l* under dorsal electrode

Images are shown for a single animal, but are qualitatively similar to the images from the other animals. The major difference between animals was in the separation between the reconstructed lung areas. In some animals these areas were distinct whereas in others they were close enough together to form a single image contrast.
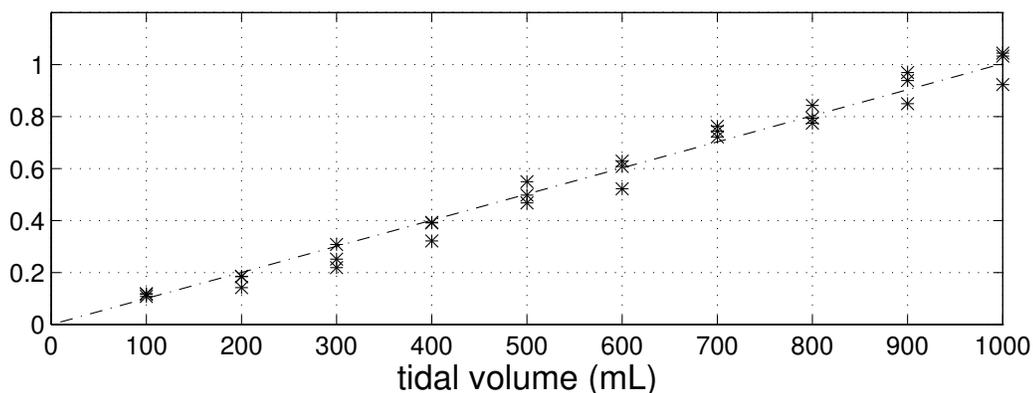
Figure 6.7: Conductivity change in the thorax from end
expiration to end inspiration vs. tidal volume
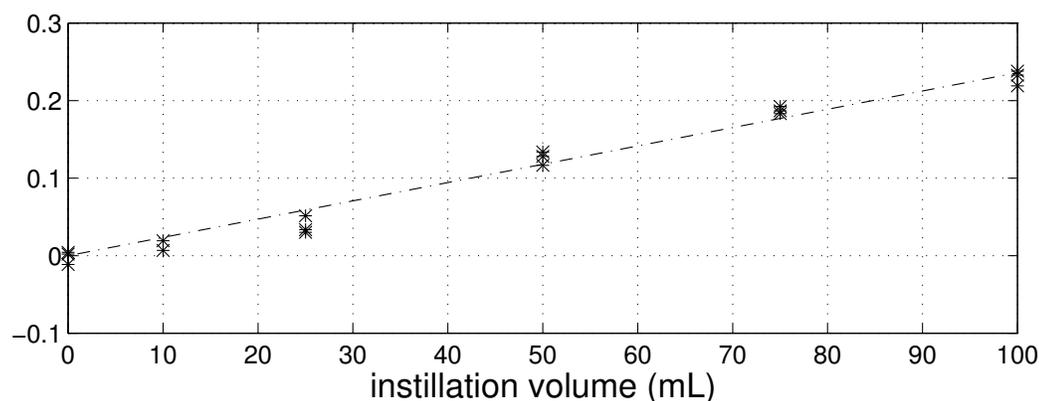
Figure 6.8: Conductivity change in the thorax vs. instilled fluid quantity

The relationship between the magnitude of the EIT image and the level of the physiological process is determined by calculating the sum of all image pixels and graphing this value with respect to the volume change between the taking of the EIT data sets. Figures 6.7 and 6.8 show graphs of the magnitude of the image sum as a function of the tidal volume and instillation fluid volume, respectively. This data was calculated from experiment #3 where all 100 m*l* volume steps were measured. The dashed line shows the best fit linear relationship. Both graphs are normalised with respect to the 1000 ml ventilation value.

Table 6.1 shows the EIT measurement error for each animal for ventilation and for instillation. In order to verify the linear model of figure 6.2, the Pearson *r* correlation coefficient is also calculated. Results are not available for instillation on dog #5 due to a computer operator's error.

Table 6.1: EIT Measurement error and correlation coefficient for ventilation and instillation data sets.

Dog #	Ventilation (m*l*)	Ventilation (*r* coefficient)	Instillation (m*l*)	Instillation (*r* coefficient)
1	153	0.975	4.1	0.997
2	69	0.995	2.7	0.999
3	95	0.988	9.7	0.983
4	43	0.998	5.7	0.995
5	40	0.998	N/A	N/A
6	72	0.994	12.7	0.980
7	68	0.994	6.8	0.991
8	168	0.959	37.5	0.717
9	82	0.992	7.3	0.992
10	112	0.977	4.4	0.997
Average	90	0.987	10.1	0.961

Another way to describe this data is to compare the fluid volumes calculated from the EIT image interpretation model to the fluid volume levels used. For instance, all EIT estimates for each dog for 50 ml fluid instillation are used to calculate a mean estimate and an associated standard deviation for this instillation level. This calculation is then repeated for each instillation and ventilation level. Figure 6.9 and table 6.2 show the values calculated for ventilation and figure 6.10 and table 6.3 show those for instillation. Additionally, a line showing the ideal linear relationship is plotted.

Given measurements of the EIT image sum, y_i, and a calculated value of k_i, $(1 \le i \le M)$ for a given level of activity for each animal, the average calculated activity level, $\bar{x}$ is

$$\bar{x} = \frac{1}{M} \sum_{i=1}^{M} \frac{y_i}{k_i}$$

(6.7)

and the standard deviation of the estimate of this value is

$$\sqrt{\frac{1}{M-1} \sum_{i=1}^{M} \left(\frac{y_i}{k_i} - \bar{x} \right)^2}$$

(6.8)
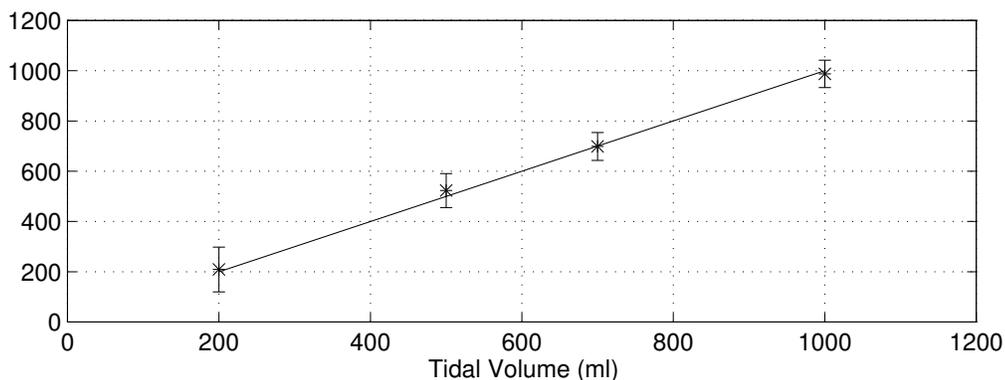
Figure 6.9: Average volume from EIT image vs. Tidal Volume
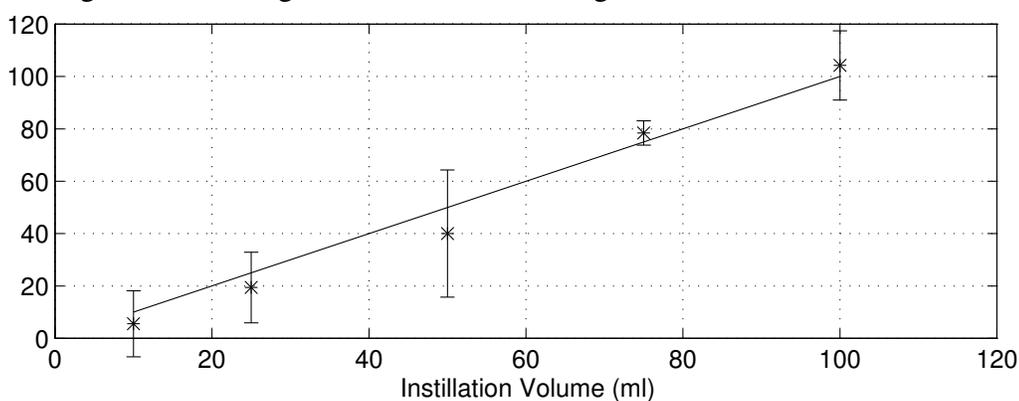
Figure 6.10: Average volume from EIT image vs. Instilled fluid Volume

Table 6.2: Average volume from EIT image and error for ventilation

Tidal Volume (ml)	Average volume from EIT image (ml)	Standard deviation Error (ml)
200	209	89
500	523	68
700	699	55
1000	988	55

Table 6.3: Average volume from EIT image and error for instillation

Instillation Volume (ml)	Average volume from EIT image (ml)	Standard deviation Error (ml)
10	5.6	12.6
25	19.4	13.5
50	40.0	24.3
75	78.5	4.6
100	104.2	13.2

6.5 Results for fluid reabsorbtion
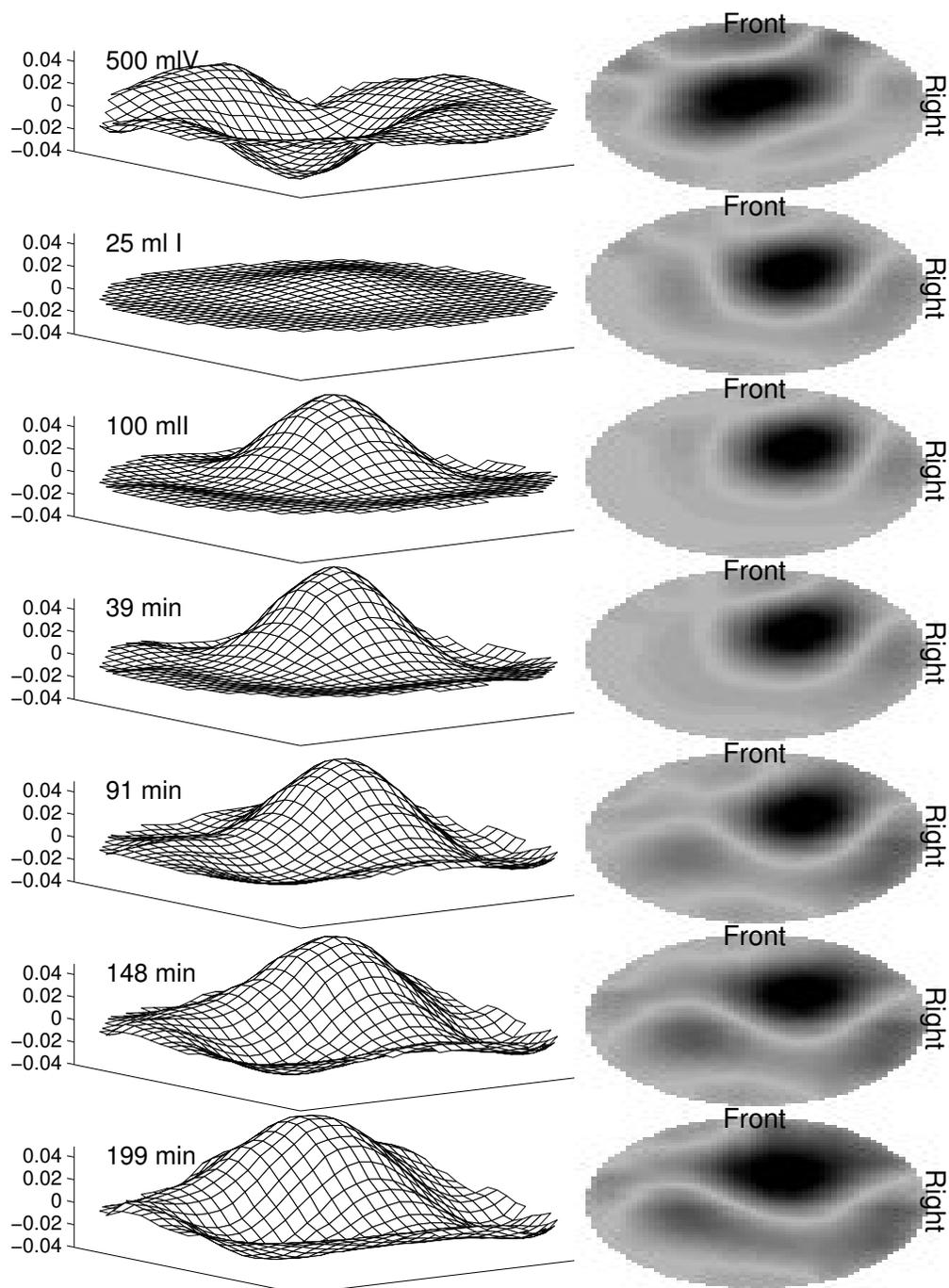
Figure 6.11: Images of conductivity change in the dog thorax for experiment #4.

Figure 6.11 shows images of conductivity changes in the thorax during the reabsorbtion of lung fluid for the dog of experiment #4. All images are reconstructed with respect to the reference data set taken at end-expiration just before fluid instillation. The image labelled "500 ml V" reconstructs the conductivity at end-inspiration. The next two images show different levels of fluid instillation, "25 ml I" and "100 ml I" reconstruct 25 and 100 ml of fluid instillation, respectively. While ventilation produces a decrease in the conductivity, fluid instillation produced a conductivity increase.

The subsequent images, labelled "39 min", "91 min", "148 min", and "199 min", reconstruct the conductivity distribution at these time intervals after instillation. It is interesting to note that the fluid region tends to move toward the front of the animal over the course of time. This effect is evident, to varying extents, in all the animals. Since the animals were in the prone position, this would indicate a downward movement due to gravity. The EIT images, while of low resolution, show the positions of the lungs, and clearly distinguish the lung which underwent instillation.
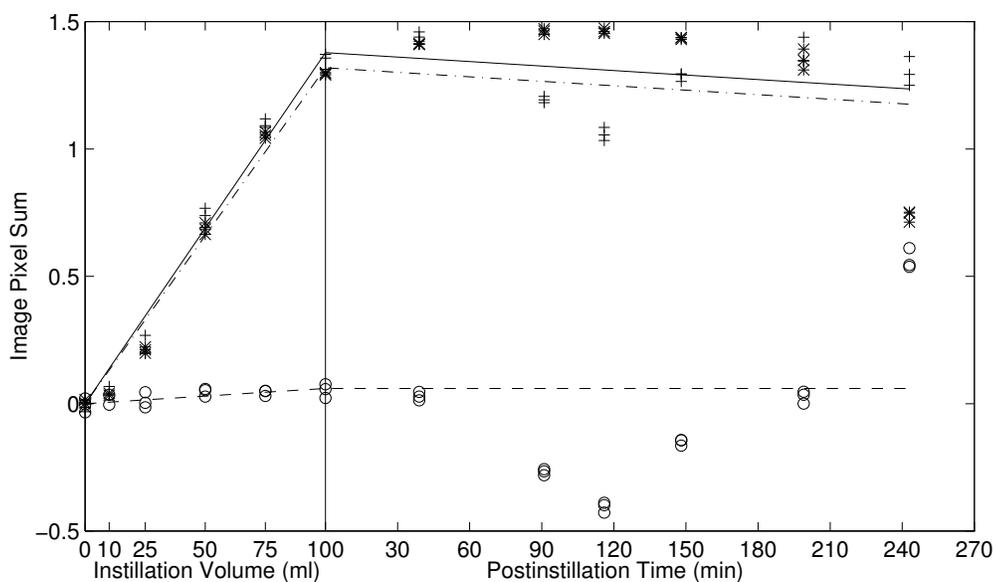
Figure 6.12: Image magnitude vs. instillation volume and reabsorbtion time.
Symbol + : Pixel sum in R_i
Symbol o : Pixel sum in R_c
Symbol * : Pixel sum in R_d

The EIT pixel sums in the regions R_i, R_c and R_d, are shown in figure 6.12 during the instillation and reabsorbtion phase of experiment #4. Additionally, the curves fitted

during the instillation (equation 6.4) and reabsorbtion (equation 6.6) phases are shown. During the instillation, the pixel sum in the region R_i is almost identical to that in R_d. During the reabsorbtion phase, however, there is a drift in both R_i and R_c, which is reduced by taking the difference between these regions, as in R_d.

Table 6.4 shows the values of the expected error of the EIT measurement for instillation, σ_i, and reabsorbtion, σ_r, for each animal and for each choice of ROI. Additionally, the residual fluid, $x_{t\max}$, at the end of the experiment, $t_{\max}$, is calculated from the EIT data by

$$x_{t_{\max}} = x_o - rt_{\max}$$

(6.9)

and is also calculated gravimetrically. Data was not available for these calculations for experiments #1 and #5.

Table 6.4: Residual water content and EIT estimation errors.

Dog #	Image	Error (ml) Instillation	Error (ml) reabsorbtion	Residual Fluid (ml)
2	gravimetric			63.7
	instilled	3.09	13.35	110.0
	difference	4.92	9.39	78.4
	total image	2.51	25.31	137.3
3	gravimetric			81.3
	instilled	7.97	9.25	72.9
	difference	8.51	10.69	106.6
	total image	9.67	12.52	50.2
4	gravimetric			78.5
	instilled	5.50	10.87	78.8
	difference	5.56	17.54	59.9
	total image	5.86	26.67	95.3
6	gravimetric			91.3
	instilled	8.23	17.94	62.8
	difference	7.23	25.55	185.5
	total image	12.04	35.48	-66.1
7	gravimetric			56.6
	instilled	3.86	17.75	-20.7
	difference	2.34	10.17	193.2
	total image	6.45	33.36	-152.9

8	gravimetric			50.1
	instilled	23.15	45.83	-196.0
	difference	15.04	24.29	-85.6
	total image	37.51	85.33	-313.3
9	gravimetric			13.2
	right	4.13	24.82	152.3
	difference	5.79	19.55	140.2
	total image	7.31	35.45	161.8
10	gravimetric			45.1
	instilled	6.35	1088.39	-4455.0
	difference	14.57	42.23	221.5
	total image	4.43	1446.54	-5937.8

6.6   Discussion

The performance of EIT in each of the four categories mentioned has been evaluated:

• **Quantitative determination of physiological activity levels:** EIT shows good performance in quantifying lung ventilation and fluid instillation:

Lung ventilation: EIT image magnitude is correlated linearly to lung tidal volume with a mean correlation coefficient of 0.987. This indicates that the image can be used as an estimate of tidal volume; the calculated average EIT measurement error for this application is 90 ml.

Fluid instillation: Image magnitude correlates well with the quantity of fluid. The mean correlation coefficient is 0.961 and is above 0.95 for all experiments except #8. The measurement error for EIT estimation of fluid quantity is 10 ml.

• **Rejection of extraneous physiological activities:** The data acquisition protocol used resulted in successful rejection of conductivity changes due to cardiac activity in both measurement of lung ventilation and tidal volume. It is possible that some of the error in the measurements is due to variability in lung volume. The relatively

low EIT measurement error values, however, indicate that the imaging process is quite effective at eliminating contributions from extraneous processes.

- **Cross-sectional image production:** Images of lung ventilation showed a zone of conductivity change distributed roughly equally on both sides of the thorax, while fluid instillation images showed a conductivity change zone clearly on one side of the image. The location of this zone corresponded in all experiments to the instilled lung.

- **Monitoring:** The calculation of the residual lung fluid by EIT does not correlate well with the values determined from the extracted lungs. The average difference between the residual fluid estimates in experiments #1 to #6 for the instillation region R_i is 20.9 ml. In experiments #7 to #10 these errors are significantly higher. This is possibly due to the fact that the EIT system was repaired between experiments #6 and #7 and the replaced parts may have had a larger electronic drift. This data indicates that the EIT system used for these experiments cannot monitor conductivity changes over periods of hours. It is, however, possible that this inaccuracy is caused by drift in the measurement electronics. If this is the case, it should be possible to correct for this with improved electronic design of the EIT system.

Certain sources of error have been identified in the experimental procedure. Firstly, the clamping of the airway tube by a human operator is potentially inaccurate. As the ventilator was pumping continuously the operator had to time the closing of the tube to coincide with end-expiration and end-inspiration. Some of the scatter of the data points at a given tidal volume (for example in figure 6.7) may be to due this difficulty. Since the air flow changes much more quickly at end-inspiration than end-expiration, variability in the clamping at end-inspiration would have more effect on lung volume than variability at end-expiration. Since the only image reconstructions which used data acquired at end-inspiration was for the lung ventilation, this would explain the higher EIT measurement error for ventilation than instillation.

Additionally, during time taken for the data acquisition the air volume in the lungs may have decreased due to uneven CO_2 / O_2 exchange rates. Under anesthesia dogs have a resting O_2 uptake of 6 ml/kg/min, or about 200 ml/min for a 35 kg dog (Cain, 1977; Shardonofsky, 1990). Under normal conditions the respiratory exchange ratio (the ratio of CO_2 out to O_2 in) is about 0.8, leaving a net volume loss in the lungs of approximately

40 ml/min. However, during periods of apnea, R falls and the net volume loss may increase considerably. Using a volume loss estimate of 40 ml/min during the average time taken of about 15 s from the clamping the airway tube until the end of data acquisition, there is an average of approximately 10 m*l* less lung volume at the end of the data acquisition than at the beginning. This value is relatively small compared to the ventilation tidal volumes measured. The development of more technically advanced EIT systems which can acquire data more rapidly should eliminate this problem.

Selection of the ROI has a significant effect on the calculated EIT measurement error. Table 6.5 compares the measurement errors for three different regions of interest: the instilled region (R_i), the difference region (R_d), and the whole thorax region (R_t). The average EIT measurement error is calculated for instillation for experiments #2 to #4 and #6 to #10 and the average error in measurement of the reabsorbtion is calculated for experiments #2,#3,#4 and #6. Since ventilation produces a conductivity change across the whole thorax, the ROI analysis cannot be used for these data sets. The lowest error is in R_i, followed by R_d, with the highest error in R_t. It seems that the selection of a smaller ROI contributes to reducing errors.

Table 6.5: EIT measurement errors for different ROIs.

ROI	Instillation (m*l*)	Reabsorbtion (m*l*)
R_i	7.8	20.9
R_d	8.0	38.2
R_t	10.7	69.7

CHAPTER 7:
DISCUSSION AND CONCLUSION

7.1   Summary

This thesis evaluates EIT as a technique for the measurement of lung function. There are several clinical applications which could benefit from this technology should it be feasible and have sufficient accuracy. Current pulmonary monitoring techniques, based on mechanical measurement of flows, volumes and pressures, typically measure one global parameter for lung function and do not allow investigation of regional inhomogeneities. Current imaging techniques, on the other hand, due to their invasiveness, cost, and cumbersomeness do not allow monitoring of the lung function over time.

Although EIT has low spatial resolution compared to these imaging modalities, it has the advantage, due to its non-invasiveness, of temporal resolution. With currently available technology, rates of 6 images/second are possible, and this should increase with newer versions of EIT equipment. The most attractive feature, however, is the possibility of continuously imaging over periods of hours, enabling the equipment to monitor changes in lung function associated with changing activity, administration of a drug or with the progression or resolution of a pathology.

In this thesis this question has been approached from two perspectives. From a theoretical perspective, image reconstruction algorithms were developed, and certain physiological difficulties which affect the image interpretation were modelled. From an experimental perspective, the ability of EIT to quantify some basic lung functions was verified.

Two different techniques for image reconstruction have been developed, an artificial neural network algorithm (ANN), and a maximum a posteriori (MAP) based regularization technique. The key advantage of both of these techniques is the ability to take into account properties of the measurement system, such as the level of noise in the

data and the maximum attainable spatial resolution. With the ANN technique this property is a function of the training set used; by using a higher noise level in the training data, the network was able to perform better in response to measurement noise. In the MAP approach this adaptation is possible because the algorithm is based on a statistical description of the measurement system.

One advantage of these techniques in an experimental application is the definition of algorithm performance in terms of the measurement system rather then the data set. If the reconstruction depends on the data, all calculations need to be done for each data acquisition, whereas these algorithms calculate a reconstruction matrix once, and each image reconstruction requires only a matrix multiplication and a mapping into image space. These differences can be significant: while the image reconstruction takes 0.25 seconds on a SUN SPARC 10 system, calculation of the matrix for the MAP algorithm requires 537 seconds, while for the ANN, network training requires several hours.

In order to compare these algorithms with reconstruction techniques proposed by other groups, several figures of merit were defined. The noise performance of an algorithm is measured with the *noise figure*, the *position error* measures the precision of reconstruction of an object's position, and the image resolution is measured by the *blur radius*. Using these figures of merit, the MAP technique is compared to the reconstruction techniques proposed by Yorkey et al. (1987) and Woo et al. (1993) in chapter 4, and the MAP and ANN algorithms are compared in annex A.

The non-linearity of EIT poses several difficulties, which, at present, are not taken into account in the image reconstruction techniques proposed. It is therefore important to be able to interpret reconstructed images with an understanding of the possible contributions of these difficulties. Chapter 5 discusses the determination of the effect of electrode movement on EIT images of lung ventilation. While several other image interpretation difficulties exist, it was felt that this was the most important consideration for interpretation of pulmonary function. A finite element model of the mechanical and electrical properties of the thorax was used to simulate the EIT measurement contribution from thorax expansion and from lung conductivity change during breathing. Results indicate that thorax expansion contributes constructively to ventilation images and accounts for from 2 to 20 percent of the image magnitude, depending on the geometry of the movements of the rib cage.

The ability of EIT to measure certain pulmonary functions was experimentally evaluated in dogs: measurement of the level of lung ventilation was validated by comparing the EIT image magnitude to the tidal volume measurement of the ventilator; quantification of fluid presence in a lung was compared to the volume of fluid instilled; and determination of which lung received the fluid was verified by comparison to the extracted lungs. Results indicate that EIT can always determine the affected lung, and can measure ventilation and instillation with a mean error of 90 m*l* and 10 m*l*, respectively.

Additionally, EIT measurement of the reabsorbtion of lung fluid was compared to gravimetric appraisal in the extracted lungs. Unfortunately, the amount of residual fluid calculated from the reconstructed image had a substantial error due to drift in the data measurements.   While EIT measurement of short time scale (less than an hour) phenomena was relatively good, measurement of changes over longer periods are subject to electronic drift in the measurements. This difficulty is possibly due to the design of the EIT system used (HEMOS III, see Guardo et al. (1991)) and may be less significant in the most recent system design (Savoie, 1994). These results are discussed in chapter 6.

7.2   Future Work

EIT is sufficiently new as a technology that abundant possibilities for improvement and validation exist. This section presents the open questions that, in the opinion of the author, are most important for the measurement of pulmonary function.

7.2.1   Image Reconstruction and Interpretation

•   **Complex impedance distributions.** Most image reconstruction algorithms typically assume that there is only a conductive component to the impedance. Lungs, however, show significant admittivity at the frequencies used by EIT (Surowiec, 1987; Foster 1989; Nopp 1993). The assumption that tissue is purely conductive may introduce errors into reconstructions. Some authors (for example Riu, 1992) propose separately reconstructing in-phase and quadrature images from the in-phase and quadrature measurements, respectively, but this assumption is clearly too simplistic.

It would seem that the MAP model proposed in chapter 4 could be adapted to take into account the admittivity of the medium. As previously shown, the voltage distribution in the medium can be expressed by

$$\nabla \bullet (\sigma - j\omega\varepsilon\varepsilon_o)\nabla V = 0 \tag{7.1}$$

The finite element model can be adapted to accept two parameters for each element, a conductivity and an admittivity, and calculate a vector, $\mathbf{v}$, of in-phase and a vector, $\mathbf{u}$, of quadrature voltage measurements. The dynamic signal vector, $\mathbf{z}$, would become

$$\mathbf{z}_{2i-1} = \frac{\mathbf{v}_i^1 - \mathbf{v}_i^2}{\frac{1}{2}\left(\left\|\mathbf{v}_i^1 + j\mathbf{u}_i^1\right\| + \left\|\mathbf{v}_i^2 + j\mathbf{u}_i^2\right\|\right)}$$

$$\mathbf{z}_{2i} = \frac{\mathbf{u}_i^1 - \mathbf{u}_i^2}{\frac{1}{2}\left(\left\|\mathbf{v}_i^1 + j\mathbf{u}_i^1\right\| + \left\|\mathbf{v}_i^2 + j\mathbf{u}_i^2\right\|\right)} \tag{7.2}$$

where each pair of components, $2i$-1 and $2i$, of the signal represents the in-phase and quadrature components, respectively, from a pattern of current injection and voltage measurement. Using this signal, the vector of image elements conductivities and admittivities, $\mathbf{x}$, is estimated, using the regularised image reconstruction formulation

$$\mathbf{x} = (\mathbf{H}^H \mathbf{W} \mathbf{H} + \mu \mathbf{Q})^{-1} \mathbf{H}^H \mathbf{W} \mathbf{z} \tag{7.3}$$

where $\mathbf{H}^H$ indicates the complex conjugate transpose of $\mathbf{H}$. The parameters $\mathbf{W}$, $\mathbf{Q}$, and μ would be the same as those used in the conductivity only algorithm, while the sensitivity matrix, $\mathbf{H}$, would be defined by

$$\mathbf{H}_{ij} = \left.\frac{\partial[\mathbf{Z}(\mathbf{x})]_i}{\partial \mathbf{x}_j}\right|_{\mathbf{x}=\mathbf{x}_o} \tag{7.4}$$

where $\mathbf{Z}(\mathbf{x})$ is a finite element model of the measured dynamic signal, $\mathbf{z}$, due to a conductivity and admittivity change, $\mathbf{x}$. The parameter $\mathbf{x}_O$ represents the background conductivity and admittivity distribution. $\mathbf{H}$ would have dimensions of twice the number of finite elements by the number of signal components.

Unfortunately, even with a reconstruction model of the complex impedance change, *in vitro* verification would be difficult. It would be necessary to construct several targets for the saline tank with the same conductivity but different dielectric properties.

•   **Regularization Schema.**   The MAP image reconstruction algorithm presented here uses a quadratic model for the regularization term because it allows a simpler, matrix algebra implementation from which the reconstruction can be performed without iterative calculations. The disadvantage, however, is that this term does have a strong tendency to blur edges. Recently, however edge preserving regularization schemes (for example Bouman, 1993) have been proposed. It might be possible to achieve improvement in image quality by adapting the regularization to this sort of approach.

•   **Use of an esophageal reference electrode.** The utility of an esophageal reference electrode has been suggested by Schuessler (1995) to improve image resolution and noise performance of the image reconstruction. The MAP image reconstruction model could be able to incorporate this information with relatively minor changes.

•   **2D reconstruction of 3D distributions.** Image reconstruction algorithms based on 2D models show good performance in reconstructing the position of a target in a 3D medium, although there is a certain tendency to "push" off-plane conductivity changes toward the centre of the image. In the case of imaging a target with large vertical extent, there would be a contribution from in-plane and off-plane conductivity changes. It would be important to understand the relationship between the vertical extent of the conductivity change to the amplitude of the image.

•   **Effect of the inhomogeneous "background" conductivity distribution.** In dynamic EIT, the reconstruction algorithms tend to calculate a sensitivity matrix using the assumption that the impedance variations are superimposed on a homogeneous background distribution. This assumption is not justified, especially in the case of the thorax. For instance, the non-conductive lungs "hide" the heart by reducing and distorting the current density in that region compared to that of a homogeneous medium. This could imply that cardiac conductivity changes are less visible and also possibly wrongly positioned. While it might be possible to obtain sufficient anatomical information to correctly reconstruct the background conductivity, it seems more promising to model this effect in order to understand how to interpret images in light of this difficulty.

•   **Resolving quantitative conductivity estimates.** Since EIT is sensitive to errors in the geometrical model, has low spatial resolution, cannot image the 3D extent of an object, and is non-linear in response to large conductivity changes, it would be

important to understand whether actual resistivity changes (in units of ohms) could be calculated from the image. While these values are calculated by algorithms such as the one proposed by Cheney (1990), their accuracy has not been carefully determined *in vivo*. This question can be considered to be equivalent to the problem of accurately determining the value of the conversion factor, *k*, of figure 6.2.

• **Effect of anisotropic tissue on image reconstruction.** While the development of image reconstruction algorithms which take into account tissue anisotropy presents significant difficulties, evaluation of its effect on image reconstruction should be relatively straight forward. *In vitro* modelling of anisotropic conductivities is currently possible with a saline filled tank, and it would also be possible to develop finite element models of the forward problem to take anisotropy into account.

7.2.2 Clinical evaluation

A recent version of the EIT hardware (Savoie, 1995), offers the capability of measuring 16 channels of EIT data at a frame rate of 5.5 Hz simultaneously with readings of the electrocardiogram (ECG) sampled at 90 Hz. Standard indices of airway flow, such as the forced expiratory volume or the forced expiratory flow, are typically measured over time intervals of a second or more, and are perhaps within the capabilities of this system. Another significant possibility would be the monitoring of variations in the functional residual capacity (FRC) over short periods. These variations are typical of restrictive lung diseases such as pneumothorax and pleural effusion, and cannot currently be measured without a pressure chamber which restricts access of medical staff to a patient. Since restrictive lung diseases typically have significant regional variation, EIT would offer the additional advantage of being able to produce a cross-sectional image of distribution of these variations.

Continuous monitoring of these variables for a patient in intensive care would allow changes in lung function over time to be recorded, and, in critical conditions, the setting of an alarm. In order to use EIT in these applications, certain questions need to be investigated experimentally.

• **Linearity of conductivity change with physiological processes.** While the results of chapter 6 indicate the linearity of EIT image magnitude as a function of the

level of lung ventilation or fluid instillation, these tests were performed in the normal physiological ranges and extreme conditions were not investigated. This relationship should be investigated over a wider activity range and for ventilation into each lung individually.

• **Comparing EIT measurements from two different subjects.** In order to compare physiological processes in two different subjects it is important to understand the relative contribution of the different processes. For instance, using the model of Trudelle et al. (1995) for the experimental data discussed in chapter 6, a parameter k_v can be defined relating image magnitude to ventilator tidal volume, and a parameter k_i which relates image magnitude to instilled fluid volume. While there is considerable variability in these values between animals due to anatomical differences, it is possible that the ratio k_i/k_v is relatively constant between animals. It would be important to determine whether this ratio is constant, and if not, whether its variability can be understood in terms of anatomical parameters.

• **Stability during long term monitoring.** Many physiological processes of interest take place over hours or days. While the results in chapter 6 show that the EIT system used had a significant measurement drift over four hours, it is possible that this problem can be overcome with improved electronic design of the measurement system.

• **Measurement of respiratory indices.** One potential application of EIT is the calculation of the indices of respiratory flow that are currently measured by spirometer. These indices of respiratory volume and flow have an important diagnostic function, especially in distinguishing between obstructive and restrictive lung diseases. EIT could provide additional information from the cross-sectional image of the lungs which would show the fraction of the lungs actually involved in communicating air. This could facilitate the detection of pneumothorax or pleural effusion.

Two standard indices of ventilatory capacity are most commonly used (West, 1992). The forced expiratory volume (FEV) measures the maximum volume exhaled in 1 second, while the forced expiratory flow (FEF) is the average flow during the middle half of the spirometer curve. The FEF is defined to be half of the vital capacity divided by the time taken to exhale from 25 to 75 percent of the vital capacity. In order to make these measurements EIT must be able to acquire data sufficiently rapidly. Since the standard

indices of respiratory function are typically normalised with respect to the vital capacity (West, 1990), there is no need to have an external measurement to allow conversion of the EIT image magnitude into volume units. If it were possible to acquire EIT data at 20 images per second, this would indicate a worst case error of 5 % in the measurement of the FEV, if no other sources of error were present. This level of error would be acceptable for this application especially since only relatively large changes in this index are considered to be clinically significant (West, 1992).

- **Measurement of air flow.** The measurement of air flow is more difficult than the measurement of volume because the EIT image can be most easily interpreted as an index of volume, and the flow must be calculated from the change in this volume as a function of time. Typically, this calculation amplifies the noise in a signal, and may make the calculated output too noisy to be useful diagnostically.

7.3   Conclusions

Although many questions still remain open with respect to the interpretation and accuracy of EIT results in experimental situations, this thesis does allow some conclusions to be made.

- **Image reconstruction.** Image reconstruction algorithms have been developed which provide fast image calculation and are able to take into account information about the configuration and measurement accuracy of the EIT system. Additionally, these algorithms are significantly robust in the presence of measurement uncertainties such as the electrode position and thorax shape.

- **Image interpretation.** Certain physiological sources of error such as electrode movement due to breathing introduce errors into EIT images. In the case of electrode movement, is possible to take into account these difficulties in the interpretation of images because the amplitude of the artefact introduced correlates linearly with the image magnitude.

- **Experimental Validation.** EIT can measure lung ventilation and lung fluid instillation which take place over short (less than one hour) time intervals with a clinically useful precision. The mean error for measurement of lung ventilation is 90 ml

and for lung fluid instillation is 10 ml. Additionally, EIT can produce an image from which the instilled lung can be determined. Thus, EIT is able to provide quantitative measurement of lung processes as well as an image from which certain spatial inhomogeneities in lung function can be determined.

ANNEX A:
COMPARISON BETWEEN NEURAL NETWORK AND MAXIMUM A POSTERIORI APPROACHES TO IMAGE RECONSTRUCTION

A.1   Introduction

Two approaches to image reconstruction have been proposed in this thesis. An algorithm based on artificial neural networks (ANN) is discussed in chapter 3, and a maximum a posteriori (MAP) technique is elaborated in chapter 4. The advantage of both of these techniques is their ability to adapt to the conditions in which the EIT measurements are made. Conditions such as the experimental noise level, the electrode positions, and the form of the thorax can be taken into account. The ANN takes these conditions into account by including them into the set of training measurements, and the MAP is adapted by careful selection of the *a priori* statistical descriptions of the medium on which the algorithm is based.

Another advantage of these techniques is the ability to reconstruct the conductivity image at low computational cost. While the calculation of the MAP estimation matrix is long, and the training of the reconstruction network even longer, the image reconstruction in both cases can be described by a single matrix multiplication, which can be calculated efficiently. Given a signal vector, $\mathbf{z}$, the conductivity change image, $\mathbf{x}$, is estimated from

$$\mathbf{x} = \mathbf{Bz} \tag{A.1}$$

where the matrix $\mathbf{B}$ has dimensions of the number of voltage measurements by the number of image elements. In order to keep notational consistency with chapter 3 the reconstruction matrix calculated by the ANN is labelled $\mathbf{N}$.

A.2   Performance of Neural Networks

The properties of the ANN reconstruction matrices are shown in table A.1. These are the same results presented in table 3.1 with an additional column representing the NF for each matrix, calculated using equation 4.38. Additionally, a matrix $\mathbf{B}_{ebp}$ is calculated which maps the filtered backprojection algorithm (Barber, 1987) onto the finite element geometry. This allows comparison of the algorithms using the figures of merit (blur radius (BR) and position error (PE)) developed to evaluate the MAP model.

Table A.1: Noise properties of backprojection and neural network algorithms.

Algorithm	Training SNR	Image SNR	Algorithm NF
$\mathbf{B}_{ebp}$		2.62	0.40
$\mathbf{N}_0$	∞	0.22	13.42
$\mathbf{N}_1$	1.33	0.69	2.05
$\mathbf{N}_2$	0.33	1.58	1.28
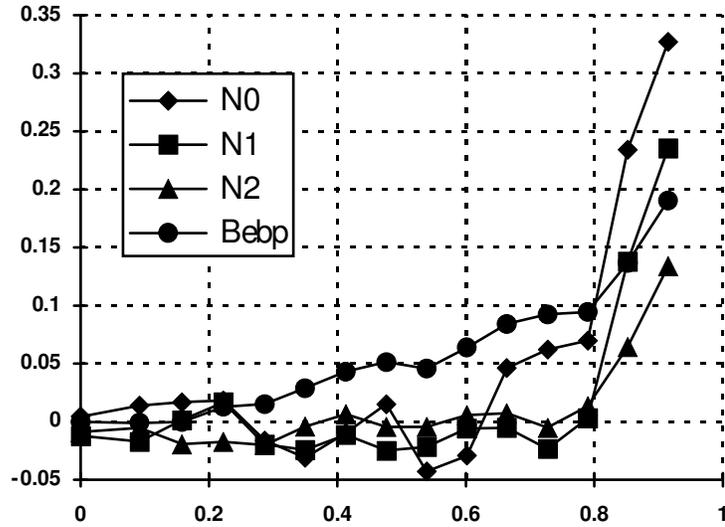
Figure A.1: Position error vs. radial position for different noise figures

Figure A.1 shows the PE and figure A.2 the BR as a function of radial position, where a radial position of 0 indicates the centre of the medium and 1 indicates the boundary. These results indicate that the algorithm trained without noise, $\mathbf{N}_2$, has the best performance in terms of position error and resolution, followed by $\mathbf{N}_1$, $\mathbf{N}_0$ and finally by

$\mathbf{B}_{ebp}$. These results are consistent with those of chapter 4, which indicate that an improvement of the performance of an algorithm in PE and BR tends to be at the expense of Noise performance.
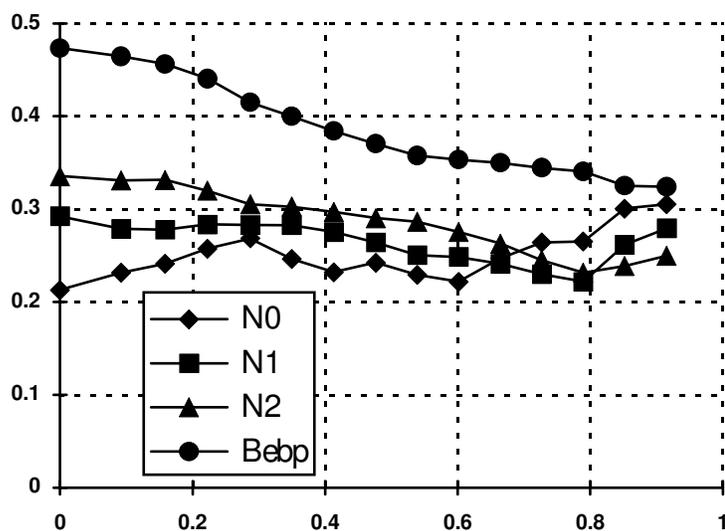

Figure A.2: Blur radius vs. radial position for different noise figures

A.3 Comparison of ANN and MAP techniques

In order to compare the ANN reconstruction algorithms to those developed using the MAP technique, matrices are calculated using the same FEM geometry (and thus the same number of image elements) as was used to train the ANN algorithms.

$\mathbf{B}_F$ is calculated using the MAP model with a spatial filter of 10 percent of the medium diameter and a regularization parameter chosen to ensure a NF of 2.0. Additionally, a matrix $\mathbf{B}_I$ is calculated corresponding to the technique proposed by Yorkey (1987), also with a NF of 2.0.

Figure A.3 illustrates image reconstructions of a simulated data set using these various techniques. Each image is shown as a wire frame mesh on the left hand side and as a grey scaled image on the right. Figure A.3A shows the target pattern. Figures A.3B, D, and F are reconstructed using the measurements from A.3A with no noise added, while figures C, E, and G use measurements with a SNR of 0 dB.
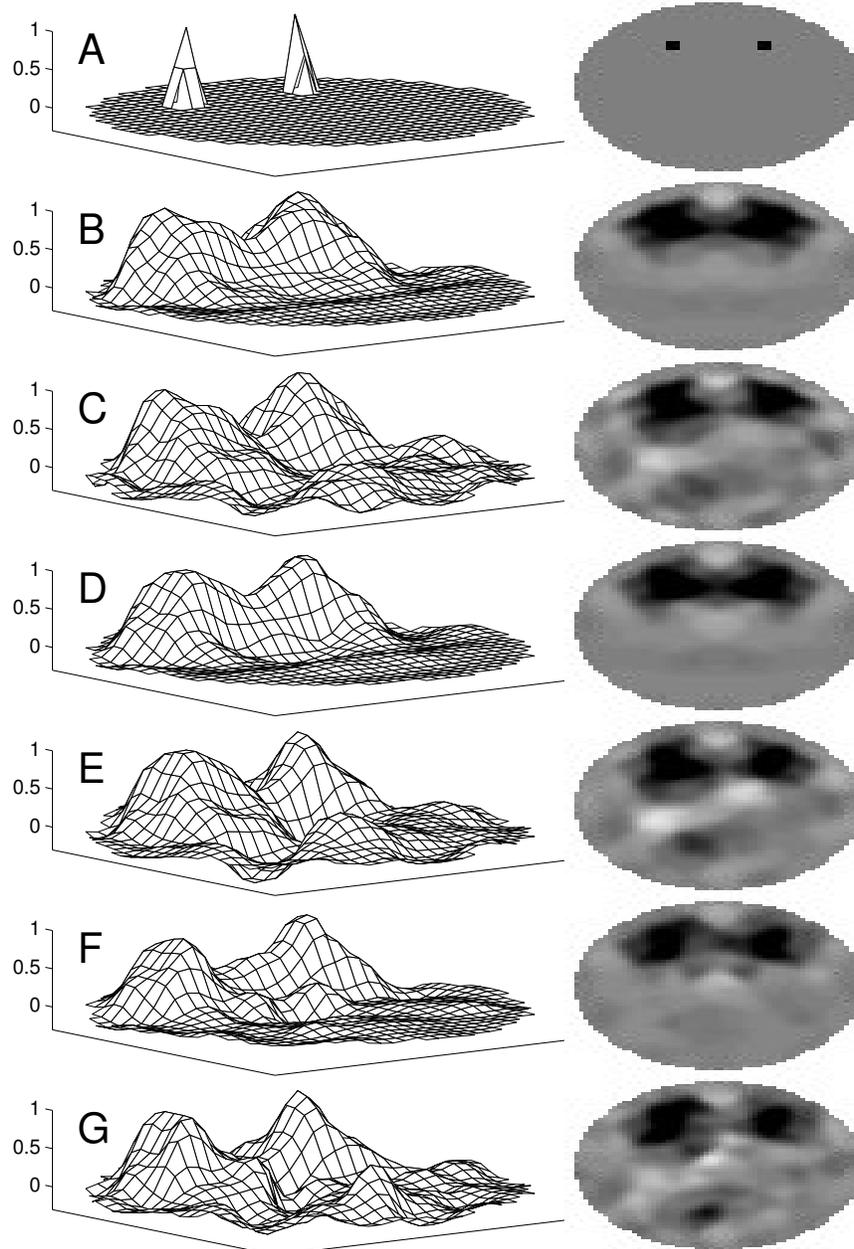
Figure A.3: Reconstructed Images

      A: Generating Conductivity Distribution

      B: Measurements: No Noise Reconstruction: $\mathbf{B}_I$, NF=2.0

      C: Measurements: 0 dB SNR Reconstruction: $\mathbf{B}_I$, NF=2.0

      D: Measurements: No Noise Reconstruction: $\mathbf{B}_F$, NF=2.0

      E: Measurements: 0 dB SNR Reconstruction: $\mathbf{B}_F$, NF=2.0

      F: Measurements: No Noise Reconstruction: $\mathbf{N}_I$

      G: Measurements: 0 dB SNR Reconstruction: $\mathbf{N}_I$

Reconstructions in figures A.3B and C use $\mathbf{B}_I$ (Yorkey, 1987), A.3D and E use $\mathbf{B}_F$ (MAP model), and A.3F and G use $\mathbf{N}_I$ (ANN model). All matrices have similar noise performance (as would be expected since they were calculated for the same NF), and although resolution is similar in all cases, $\mathbf{B}_F$ and $\mathbf{N}_I$ have slightly better resolution than $\mathbf{B}_I$.

Figure A.4: Position error vs. radial position for different noise figures

Figure A.5: Blur radius vs. radial position for different noise figures

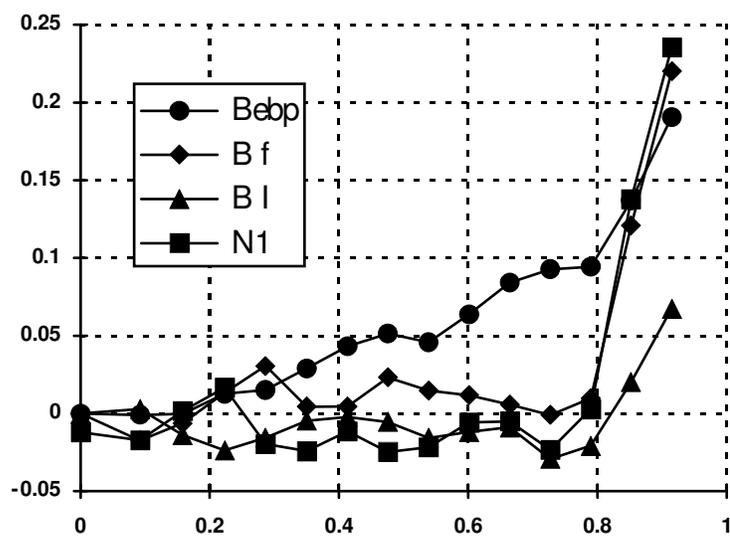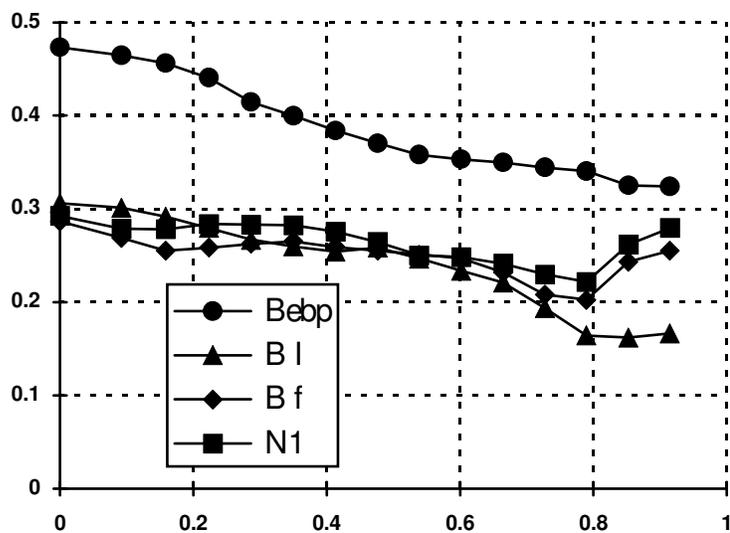The algorithms $\mathbf{N}_I$, $\mathbf{B}_F$, $\mathbf{B}_I$ and $\mathbf{B}_{ebp}$ are compared in terms of the figures of merit BR and PE. Figure A.4 shows the PE and figure A.5 the BR as a function of radial position. The algorithm which has the poorest performance, both in terms of PE and BR is backprojection. This comparison is somewhat unequal, however, because the noise performance of $\mathbf{B}_{ebp}$, with a NF of 0.40, is significantly better than that of the other algorithms, all of which have an NF of 2.0. In terms of PE, the three remaining algorithms have almost equal performance, averaging less than 0.02 when the radial position is below 0.8. In terms of BR, however, $\mathbf{N}_I$ and $\mathbf{B}_F$ have better resolution near the centre while $\mathbf{B}_I$ is better near the boundary.

It is interesting to note that the ANN and MAP techniques perform very similarly in resolution as a function of radial position. Unfortunately, since it is difficult to theoretically estimate the performance of an ANN algorithm, it is not possible to determine whether this functional similarity is due to a relationship between the algorithms. It is possible, however, that the fact that both MAP and ANN algorithms are designed to take into account the same properties of the measurement system ensures a certain similarity in performance.

BIBLIOGRAPHY

ADLER A., BERTHIAUME Y., GUARDO R., AMYOT R., (1995). "Imaging of Pulmonary Edema with Electrical Impedance Tomography", *Proc. 17th Ann. Int. Conf. IEEE Eng. Biol. Med. Soc.*, Montreal, Canada, Sept., **17** (1), 557-558.

ADLER A., GUARDO R., (1993). "An Iterative Reconstruction Technique for Electrical Impedance Tomography", *Proc. of. 1993 Conf. Canadian Medical and Biological Eng. Soc.*, Ottawa, Canada, **19**, 264-265.

ADLER A., GUARDO R., (1995). "Electrical Impedance Tomography: Regularised Imaging and Contrast Detection", Accepted for publication by *IEEE Trans. on Medical Imaging*.

ADLER A., GUARDO R., (1993). "Image Reconstruction in Electrical Impedance Tomography: A Neural Network Approach", *Proc. 15th Ann. Int. Conf. IEEE Eng. in Med. Biol. Soc.*, San Diego, USA, **15** (1), 269-270.

ADLER A., GUARDO R., (1994). "A Neural Network Image Reconstruction Algorithm in Electrical Impedance Tomography", *IEEE Trans. on Medical Imaging*, **13** (4)594-600.

ADLER A., GUARDO R., BERTHIAUME Y., (1995). "Impedance Imaging of Lung Ventilation: Do we need to account for chest expansion?", Accepted for publication by *IEEE Trans. Biomedical Engineering*.

ADLER A., GUARDO R., BERTHIAUME Y., (1994). "Imaging of Gastric Emptying with Electrical Impedance Tomography", *Proc. of. 1994 Conf. Canadian Medical and Biological Eng. Soc.*, Vancouver, Canada, **20**, 14-15.

ADLER A., GUARDO R., BERTHIAUME Y., (1994). "Impedance Imaging of Lung Ventilation: Do we need to account for chest expansion?", *Proc. 16th Ann. Int. Conf. IEEE Eng. in Med. Biol. Soc.*, Baltimore, USA, **16** (1), 534-535.

ADLER A., GUARDO R., BERTHIAUME Y., (1994). "Reconstruction d'Image en Tomographie d'Impédance Electrique", *Proc. of. 1994 Conf. Association Canadienne-Francaise pour l'Avancement des Sciences*, Montreal, Canada, 164.

BARBER D.C., BROWN B.H., (1988). "Errors In Reconstruction of Resistivity Images Using a Linear Reconstruction Technique", *Clin. Phys. Physiol. Meas.*, **9** (A), 101-104.

BARBER D.C., BROWN B.H., (1987). "Fast reconstruction of resistance images", *Clin. Phys. Physiol. Mes.*, **8** (A), 47-54.

BARBER D.C., BROWN B.H., (1992). "Image Reconstruction in Electrical Impedance Tomography Using Filtered Back-Projection", *Proc. 14th Ann. Int. Conf. IEEE Eng. in Med. Biol. Soc.*, Paris, France, **14** (1), 1691-1692.

BARBER D.C., BROWN B.H., (1985). "Recent Developments in Applied Potential Tomography - APT", *Information Processing in Medical Imaging*, 106-21.

BARBER D.C., BROWN B.H., (1990). "Shape Correction in APT Image Reconstruction", *Proc. of a meeting on Electrical Impedance Tomography, Copenhagen, Denmark*, 44-51.

BARBER D.C., BROWN B.H., HARRIS N., SEAGAR A.D., (1986). "Applied potential tomography: a review of the possible clinical applications of dynamic impedance imaging", *Recent Dev. in Med. and Physiol. Imaging. Suppl to J. Med. Eng. Technology*, Taylor and Francis, London, 8-15.

BERTHIAUME Y., BROADUS V.C., GROPPER M.A., TANITA T., MATHAY M.A., (1988). "Alveolar liquid and protein clearance from normal dog lungs", *J. Appl. Physiol.*, **65** (2), 585-593.

BERTHIAUME Y., MATHAY M.A., (1987). "Beta-Adrenegic Agonists Increase Lung Liquid Clearance in Anesthetized Sheep", *J. Clinical Investigation*, **79**, 335-343.

BOUMAN C., SAUER K., (1993). "A Generalized Gaussian Image Model for Edge-Preserving MAP Estimation", *IEEE Trans. Image Processing*, **2** (3), 296-309.

BREKTON W., (1992). "The Problem of Anisotropy in Electrical Impedance Tomography", *Proc. 14th Ann. Int. Conf. IEEE Eng. in Med. Biol. Soc.*, Paris, France, **14** (1), 1734-1735.

BROWN B.H., BARBER D.C., HARRIS N., SEAGAR A.D., (1986). "Applied potential tomography: a review of the possible clinical applications of dynamic impedance imaging", *Recent Dev. in Med. and Physiol. Imaging. Suppl to J. Med. Eng. Technology*, Taylor and Francis, London, 8-15.

CAIN S.M., (1977). "Oxygen delivery and uptake in dogs during anemic and hypoxic hypoxia", *J. Applied Physiology*, **42** (2), 228-243.

CAMPBELL J.H., HARRIS N.D., BROWN B.H., MORICE A.H., (1994). "Clinical applications of electrical impedance tomography in the monitoring of changes in intrathoracic fluid volumes", *Physiol. Meas.*, **15**, A217-A222.

CARROLL L., (1911). *The Hunting of the Snark: an Agony in Eight Fits*: London, Macmillan & Co.

CHAUVEAU N., RIGAUD B., SHI Y., MORUCCI J.P., (1992). "Digital Demodulation in Electrical Impedance Tomography", *Proc. 14th Ann. Int. Conf. IEEE Eng. in Med. Biol. Soc.*, Paris, France, **14** (1), 1701-1702.

CHEN Z.Q., PAOLONI P.J., (1992). "An integral Equation Approach to Electrical Conductance Tomography", *IEEE Trans. on Med. Imaging*, **11** (4), 570-576.

CHENEY M., ISAACSON D., NEWELL J.C., SIMSKE S., GOBLE J., (1990). "NOSER: An Algorithm for Solving the Inverse Conductivity Problem", *Int. Journal Imaging Syst. and Technol.*, **2**, 66-75.

CHENEY M., ISAACSON D., SOMERSALO E.J., ISAACSON E.L., (1992). "Layer-Stripping Reconstruction Algorithm for Electrical Impedance Tomography", *Proc. 14th Ann. Int. Conf. IEEE Eng. in Med. Biol. Soc.*, Paris, France, **14** (1), 1694-1695.

DALZIEL C.F., (1956). "Effect of electric shock on man", *IRE Trans. Med. Electron.*, **5**, 44-62.

DAWIDS S.G., (1987). "Evaluation of applied potential tomography: a clinician's view", *Clin. Phys. Physiol. Meas.* , **8** (A), 175-180.

DAVEY K.R., CHENG, C.H., EPSTEIN C.M., (1991). "Prediction of Magnetically Induced Electric Fields in Biological Tissue", *IEEE Trans. on Biomed. Eng.*, **38** (5), 418-422.

DEMOMENT G., (1989). "Image Reconstruction and Restoration: Overview of Common Estimation Structures and Problems", *IEEE Trans. on Acoustrics, Speech, Signal Process.*, **37** (2), 2024-2036.

DETROYER A., LORING S.H., (1956). "Respiratory Muscle Action", Chap. 26, Vol. 3, Sect 3, *Handbook of Physiology*, American Physiological Society, Bethesda, MD, USA.

FEIN A., GROSSMAN R.F., JONES G., GOODMAN P.C., MURRAY J.F., (1979). "Evaluation of Transthoracic Electrical Impedance in the Diagnosis of Pulmonary Edema", *Circulation*, **60**, 1156-1160.

FORTIER N., DEMOMENT G., GOUSSARD Y., (1994). "GCV and ML Methods of Determining Parameters in Image Restoration by Regularization: Fast Computation in the Spatial Domain and Experimental Comparison", *J. of Visual Comm. and Image Representation*, **4** (2), 157-170.

EYÜBOGLU B.M., PILKINGTON T.C., (1992). "Anisotropic Skeletal Muscle Conductivity in Electrical Impedance Tomography", *Proc. 14th Ann. Int. Conf. IEEE Eng. in Med. Biol. Soc.*, Paris, France, **14** (1), 1726-1727.

FOSTER K.R., SCHWAN H.P., (1989). "Dielectrical Properties of Tissues and Biological Materials: A Critical Review", CRC Crit. Reviews Biomed. Eng., **17** (1), 25-104.

FUKS L.F., CHENEY M., ISAACSON D., GISSER D., NEWELL J.C., (1991). "Detection and Imaging of Electric Conductivity and Permittivity at Low Frequency", *IEEE Trans. on Biomed. Eng.*, **38** (11), 1106-1110.

GALATSANOS N.P., KATSAGGELOS A.K., (1992). "Methods for Choosing the Regularization Parameter and Estimating the Noise Variance in Image Restoration and Their Relation", *IEEE Trans. on Image Processing.*, **1** (3), 322-336.

GEDDES L.A., BAKER L.E., (1989). *Principles of Applied Biomedical Instrumentation*, 3rd edition, Wiley-Interscience Pubilcation.

GEDDES L.A., BAKER L.E., (1972). "Thoracic impedance changes following waline injection into right and left ventricles", *Journal of Applied Physiology*, **33** (3), 278-281.

GEDDES L.A., BAKER L.E., (1971). "Response to the passage of electric current through the body", *J. Assoc. Adv. Med. Instrum.*, **5**, 13-18.

GENCER N.G., KUZUOGLU M., IDER Y.Z., (1992). "Sensitivity Matrix Analysis of the Back-Projection Algorithm in Electrical Impedance Tomography", *Proc. 14th Ann. Int. Conf. IEEE Eng. in Med. Biol. Soc.*, Paris, France, **14** (1), 1682-1683.

GESELOWITZ D.B., (1971). "An Application of Electrocardiographic Lead Theory to Impedance Plethysmography", *IEEE Trans. on Biomed. Eng*., 38-41.

GLIDEWELL M. E., KWONG T.N., (1994). "The Inclusion of Anatomical Constraints and Anisotropy in Three-Dimensional Electrical Impedance Tomography", *Proc. 16th Ann. Int. Conf. IEEE Eng. in Med. Biol. Soc.*, Baltimore, MD, USA, **16** (1), 540-541.

GLIDEWELL M. E., KWONG T.N., (1993). "Including Anisotropy in Electrical Impedance Tomography using Anatomical Constraints", *Proc. 15th Ann. Int. Conf. IEEE Eng. in Med. Biol. Soc.*, San Diego, CA, USA, **15** (1), 806-807.

GRIFFITHS H., (1987). "The importance of phase measurement in electrical impedance tomography", *Phys. Med. Biol.*, **32** (11), 1435-1444.

GOLUB G.H., HEATH M., WAHBA G., (1979). "Generalized Cross-Validation as a Method for Choosing a Good Ridge Parameter", *Technometrics*, **21** (2), 215-223.

GUARDO R., BOULAY C., BENZARTI F., BERTRAND M., (1990). "Rationale for a Rigid Electrode Frame in Electrical Impedance Tomography", *Proc. 12th Ann. Int. Conf. IEEE Eng. in Med. Biol. Soc.*, Philadelphia, PA, USA, **12** (1), 126-127.

GUARDO R., BOULAY C., BERTRAND M., (1991). "A Neural Network Approach to Image Reconstruction in Electrical Impedance Tomography", *Proc. 13th Ann. Int. Conf. IEEE Eng. in Med. Biol. Soc.*, Orlando, FL, USA, **13** (1), 14-15.

GUARDO R., BOULAY C., MURRAY B., BERTRAND M., (1991). "An experimental Study in Electrical Impedance Tomography using Backprojection Reconstruction", *IEEE Trans. on Biomedical Eng.*, **38**, 617-627.

GUARDO R., BOULAY C., SAVOIE G., ADLER A., (1993). "A Superheterodyne Serial Data Acquisition System for Electrical Impedance Tomography", *Proc. 15th Ann. Int. Conf. IEEE Eng. in Med. Biol. Soc.*, San Diego, CA, USA, **15** (1), 86-87.

HUA P., WEBSTER J.G., THOMPKINS W.J., (1988). "A Regularised Electrical Impedance Tomography Reconstruction Algorithm", *Clin. Phys. Physiol. Meas.*, **9** (A), 137-144.

ISAACSON D., (1986). "Distinguishability of Conductivities by Electric Current Computed Tomography", *IEEE. Trans. on Medical Imaging*, **MI-5** (2), 91-95.

KALLMAN J.S., BERRYMAN J.G., (1992). "Weighted Least-Squares Criteria for Electrical Impedance Tomography", *IEEE. Trans. on Medical Imaging*, **11** (2), 284-292.

KOTRE C.J., (1989). "A sensitivity coefficient method for the reconstruction of electrical impedance tomograms", *Clin. Phys. Physiol. Meas.*, **10**, 275-281.

KUBICEK W.G., KOTTKE F.J., RAMOS M.U., PATTERSON R.P., WITSOE D.A., LABREE J.W., REMOLE W., LAYMAN T.E., SCHOENING H., GARAMELA J.T., (1974). "The Minnesota Impedance Cardiograph - Theory and Applications", *Biomed. Eng.*, 410-416.

LAI-FOOK S.J., WILSON T.A., HYATT R.E., RODARTE J.R., (1976). "Elastic constants of inflated lobes of dog lungs", *J. Applied Physiology*, **40** (4), 508-513,.

LEKSELL L.G., (1991). "Measurement of extravascular lung water - methods and clinical implications", *Acta. Anaesthesiol. Scand.*, **35**, Supplementum 95, 81-86.

MATHAY M.A., BERTHIAUME Y., STAUB N.C., (1985). "Long-term clearance of liquid and protein from the lungs of unanesthetized sheep", *J. Appl. Physiol.*, **59** (3), 928-934.

MCADAMS E.A., JOSSINET J., (1990). "Skin-Electrode Impedance in Impedance Tomography", *Proc. of a meeting on Electrical Impedance Tomography, Copenhagen, Denmark*, 14-19.

MORICE A.H., HARRIS N., CAMPBELL J., ZHANG F., BROWN B., (1993). "EIT in the investigation of chest disease" in HOLDER D. (ed.), *Clinical and physiological applications of electrical impedance tomography*, London: UCL Press.

MURPHY D., ROLFE P., (1988). "Aspects of instrumentation design for electrical impedance tomography", *Clin. Phys. Physiol. Meas.,* **9** (A), 5-14.

NEWELL J.C., EDIC P.M., REN X., LARSON-WISEMAN J.L., DANYLEIKO M.D., (1994). "Assessment of Acute Pulmonary Edema in Dogs by Electrical Impedance Tomography", Submitted to *IEEE Trans. Biomed. Eng*.

NEWELL J.C., ISAACSON D., GISSER D., (1988). "An Electric Current Tomograph", *IEEE Trans. on Biomed. Eng.*, **38** (11), 828-832.

NEWELL J.C., ISAACSON M., CHENEY M., SAULNIER G.J., GISSER D.G., GOBLE J.C., COOK R.D., EDIC P.M., (1992). "Impedance Images of the Chest", *Proc. 14th Ann. Int. Conf. IEEE Eng. in Med. Biol. Soc.*, Paris, France, **14** (1), 1752-1753.

NEWELL J.C., SAULNIER G.J., EDIC P.M., ISAACSON D., CHENEY D.G., GISSER D., COOK R.D., (1993). "Electrical Impedance Imaging", *Bioengineering Science News*, **17** (2), 19-23.

NEWELL J.C., ISAACSON D., SAULNIER G.J., CHENEY M., GISSER D.G., (1993). "Accute Pulmonary Edema Assessed by Electrical Impedance Tomography", *Proc. 15th Ann. Int. Conf. IEEE Eng. in Med. Biol. Soc.*, San Diego, CA, USA, **15** (1), 92-93.

NOPP P., RAPP E., PFÜTZNER H., NAKESCH H., RUHSAM Ch., (1993). "Dielectrical Properties of Lung Tissue as a function of Air Content", *Phys. Med. Biol.*, **38**, 699-716.

OLSON W.H., (1992). "Electrical Safety", in WEBSTER J.G. (ed.) *Medical Instrumentation: Application and Design*, 2nd ed., Houghton Mifflin, Boston, USA.

PAPOULIS A., (1984). *Probability, Random Variables, and Stochastic Processes,* McGraw-Hill, New York.

PARKER K.J., HUAND R.A., MUSULIN R.A., LERNER R.M., (1990). "Tissue Response to Mechanical Vibrations for Sonoelasticity Imaging", *Ultrasound in Med. and Biol.*, **6** (3), 241-246.

POMERANTZ M., DEGLADE F., EISEMAN B., (1970). "Clinical Evaluation of Transthoracic Electrical Impedance as a Guide to Intrathoracic Fluid Volumes", *Annals of Surgery*, 686-694.

PLONSEY R., (1969). *Bioelectric Phenomena*, McGraw-Hill Book Company, New York, USA.

REDDY J.N., (1992). *An Introduction to the Finite Element Method for Engineers*, Adam Hilger, New York, USA.

RIU P., ROSSELL J., PALLÀS-ARENY R., (1992). "In Vivo Static Imaging for the Real and the Reactive Parts in Electrical Impedance Tomography Using Multifrequency Techniques", *Proc. 14th Ann. Int. Conf. IEEE Eng. in Med. Biol. Soc.*, Paris, France, **14** (1), 1706-1707.

ROGERS S., KABRINSKY M., (1991). *An Introduction to Biological and Artificial Neural Networks for Pattern Recognition*, SPIE, Bellingham, WA, USA.

ROSELL J., MURPHY D., PALLAS R., ROLFE P., (1988). "Analysis and assessment of errors in a parallel data acquisition system for electrical impedance tomography", *Clin. Phys. Physiol. Meas.,* **9** (A), 93-99.

SANTOSA F., VOGELIUS M., (1990). "A Backprojection Algorithm for Electrical Impedance Imaging", *SIAM J. Applied Math.,* **50** (1), 216-243.

SAVOIE G., (1994). "Applications de la tomographie d'impédance électrique à l'étude de phénomènes physiologiques", mémoire M.Sc.A., École Polytechnique de Montréal, Canada.

SCHUESSLER T.F., BATES J.H.T., (1995). "A Non-Blurring Regularization Scheme for Electrical Impedance Tomography",*Proc. 17th Ann. Int. Conf. IEEE Eng. Biol. Med. Soc.*, Montreal, Canada, **17** (1), pp. 559-560.

SCHUESSLER T.F., BATES J.H.T., (1994). "Utility of an Esophageal Reference Electrode for Thoracic Electrical Impedance Tomography", *Proc. of. 1994 Conf. Canadian Medical and Biological Eng. Soc.*, Vancouver, Canada, **20**, 10-11.

SEAGAR A.D., BARBER D.C., BROWN B.H., (1987). "Electrical Impedance Imaging", *IEEE Proceedings,* **134** (A) 2, 201-210.

SEAGAR A.D., BARBER D.C., BROWN B.H., (1987)."Theoretical Limits to Sensitivity and Resolution in Impedance Imaging", *Clin. Phys. Physiol. Meas.,* **8** (A), 13-31.

SEAGAR A.D., BROWN B.H., (1987). "Limitations in hardware design in impedance imaging", *Clin. Phys. Physiol. Meas.,* **8** (A), 85-90.

SHARDONOFSKY F.R., SATO J., BATES J.H.T., (1990). "Quasi-Static Pressure-Volume Hysteresis in the Canine Respiratory System in Vivo", *J. Applied Physiology*, **68** (5), 2230-2236.

SHAW G.R., GOUSSARD Y., GUARDO R., (1993). "Linearization of the Forward Problem in Electrical Impedance Tomography", *Proc. 15th Ann. Int. Conf. IEEE Eng. in Med. Biol. Soc.*, San Diego, CA, USA, **15** (1), 82-83.

SHAW G.R., GOUSSARD Y., GUARDO R., (1993). "Regularized Image Reconstruction in Electrical Impedance Tomography", *Proc. of. 1993 Conf. Canadian Medical and Biological Eng. Soc.*, Ottawa, Canada, **19**, 266-267.

SMALLWOOD R.H., NOUR S., MANGNALL Y., SMYTHE A., BROWN B.H., (1992). "Impedance Imaging and Gastric A Motility", *Proc. 14th Ann. Int. Conf. IEEE Eng. in Med. Biol. Soc.*, Paris, France, (1), 1748-1749.

SPINALE F.G., REINES H.D., COOK M.C., CRAWFORD F.A., (1989). "Noninvasive Estimation of Extravascular Lung Water Using Bioimpedance", *J. Surgical Research,* **47**, 535-540.

STAUB N.C., HOGG J.C., (1980). "Conference report of a workshop on the measurement of lung water", *Critical Care Medicine,* **8** (12), 752-759.

STOY R.D., FOSTER K.R., SCHWAN H.P., (1982). "Dielectrical Properties of Mammalian Tissues from 0.1 to 100 Mhz: A Summary of Recent Data", Phys. Med. Biol., **27** (4), 501-513.

SUROWIEC A.J., STUCHLY S.S., KEANEY M., SWARUP A., (1987). "Dielectric Polarization of Animal Lung at Radio Frequencies", *IEEE Trans. Biomedical Eng.*, Vol. **BME-34** (1), 62-67.

TRUDELLE S., ADLER A., GUARDO R., (1995). "Electrical Impedance Tomography: Characterization of In-Vitro Performance", *Proc. 17th Ann. Int. Conf. IEEE Eng. Biol. Med. Soc.*, Montreal, Canada, **17** (1), 563-564.

VAHID-SHAHIDI A., GUARDO R., SAVARD P., (1992). "Effects of Excitation- to Measurement-lead Planes Separation on Conductivity Distributions Computed by Electrical Impedance Tomography", *Proc. 14th Ann. Int. Conf. IEEE Eng. in Med. Biol. Soc.*, Paris, France, **14** (1), 1728-1729.

VAHID-SHAHIDI A., GUARDO R., SAVARD P., KASHANI P., (1993). "Assessment of Electrical Impedance Tomography for Localizing Pulmoary Edema in a Realistic Human Thorax Model", *Proc. of. 1993 Conf. Canadian Medical and Biological Eng. Soc.*, Ottawa, Canada, **20**, 262-263.

VAN DE WATER J.M., MOUNT B.E., BARELA J.R., SCHUSTER R., LEACOCK F.S., (1973). "Monitoring the Chest with Impedance", *Chest*, **64** (5), 597-603.

VAN OOSTEROM A., SMULDERS L.A.W., (1990). "Electrical Impedance Measurements and Lungs Physiology", *Proc. of a meeting on Electrical Impedance Tomography, Copenhagen, Denmark*, 242-248.

WEBB S., (1988). *The Physics of Medical Imaging*, Adam Hilger, Bristol, UK.

WEBSTER J.G., (1992). *Electrical Impedance Tomography*, Adam Hilger, New York, 97-137.

WEST J.B., (1990). *Respiratory physiology - the essentials* (4th ed.), Williams & Wilkins, Baltimore, MD, USA.

WEST J.B., (1990). *Pulmonary pathophysiology - the essentials* (4th ed.), Williams & Wilkins, Baltimore, MD, USA.

WIDROW B., LEHR M.A., (1990). "30 years of adaptive neural networks: perceptron, Madaline, and Backpropagation", *Proc of the IEEE*, **78**, 1415-1442.

WIDROW B., STEARNS S.D., (1985). *Adaptive Signal Processing,* New York, Prentice-Hall.

WOLF P.D., SMITH W.M., PILKINGTON T.C., (1992). "A Method for Determining Surface Electrode Location and Boundary Shape Using Impedance Measurements", *Proc. 14th Ann. Int. Conf. IEEE Eng. in Med. Biol. Soc.*, Paris, France, **14** (1), 1724-1725.

WOO E.J., HUA P., WEBSTER J.G., TOMPKINS W.J. (1993). "A Robust Image Reconstruction Algorithm and Its Implementation in Electrical Impedance Tomography", *IEEE. Trans. on Medical Imaging*, **12** (2), 137-145.

WOO E.J., HUA P., WEBSTER J.G., TOMPKINS W.J., (1992). "Walsh Function Current Patterns and Data Synthesis for Electrical Impedance Tomography", *IEEE. Trans. on Medical Imaging*, **11** (4), 554-559.

WOO E.J., HUA P., WEBSTER J.G., TOMPKINS W.J., "Measuring Lung Resistivity Using Electrical Impedance Tomography", *IEEE Trans. on Biomedical Engineering*, Vol. 39, No. 7, 1992, 756-760.

YORKEY T.J., WEBSTER J.G., TOMPKINS W.J., (1987). "Comparing Reconstruction Algorithms for Electrical Impedance Tomography", *IEEE Trans. on Biomed. Eng.*, **BME-34**, 843-852.